

POLITECNICO DI TORINO

Corso di Laurea Magistrale in Ingegneria Aerospaziale

Tesi di Laurea Magistrale

**Prototype development of an innovative heat
exchanger for an aircraft engine cooling system
made by Additive Manufacturing (SLM).**



Relatore: Prof. Paolo Maggiore

Correlatore: Ing. Matteo Dalla Vedova

Candidato: Davide Perrone

Marzo 2019

Acknowledgments

Dedico la mia Laurea Magistrale in Ingegneria Aerospaziale e questa monografia, prima che a me stesso, a mia Nonna Antonietta, che con un solo sguardo e senza chiedere mai nulla in cambio, mi ha trasmesso costante forza e incitamento ad andare avanti, con tenacia. Rinvigorisce così il suo ricordo nella speranza di averla resa orgogliosa di me.

Allo stesso tempo ringrazio fortemente mio nonno Oronzo, che ha reso la mia vita a Torino dignitosa e tranquilla, offrendo deliberatamente pieno supporto economico, per anni ogni mese.

Un grazie doveroso lo devo alla mia famiglia, in particolare a mia madre, che ha sempre mostrato senso di comprensione e vicinanza umana nei momenti più difficili. Ad Alba, un ringraziamento amorevole, perchè è stata vittima delle mie paranoie logoranti, ma ha tenuto duro e abbiamo condiviso assieme questi mesi impegnativi ma gratificanti.

Altrettanto importanti sono stati Zia Santina, Luca e Monia qui a Torino, con loro mi sono sempre sentito in famiglia e grazie al loro immancabile supporto ho superato qualsiasi problema incontrato nella vita quotidiana.

Un affettuoso pensiero dedico ai compagni di viaggio Leonardo, Nunzio ed Andrea che hanno rappresentato la fuga divertente e il lato goliardico dell'esperienza universitaria.

Abstract

The object of the following dissertation is the construction of a prototype of an innovative heat exchanger (HE) for an aircraft engine cooling system made by Additive Manufacturing (SLM). The new shape design is referred to the internal surface of exchange, the core of the compact HE to enhance the convective heat transfer coefficient and reduce, at the same time, the pressure drop occurred across the ducts of the block. The compact heat exchanger is embedded in the engine, as part of the cooling system of the aircraft built by I.C.P. srl.

In fact this work is the summary of my Master Thesis that I have done in stage with an aircraft's company, the I.C.P. Aviazione srl, located in Castelnuovo Don Bosco (AT). The stage started in September 2018 and ended in February 2019. In addition to this, it is important to consider that the main purpose of the thesis was not only design and analysis of the component of the engine but, eventually, the construction of the heat exchanger too.

Therefore the second phase of the thesis consisted in construction of the heat exchanger by additive manufacturing technique, in particular Selective Laser Melting provided by AIDRO srl, a 3D printing company located in Varese. The collaboration with them started by sharing the Solidworks CAD model of the component built up by me and sent to the factory for the final integration and printing.

I could summarise the main goal of the master thesis as follows. First step preliminary research about the state of the art of the heat exchanger for industrial application and, simultaneously the study of the heat flux physical principles. Then by considering constraints and output performances required by the HE, the design of an innovative and better performing core to supply the leakage exposed by ICP's engineers. The result was a CAD model file containing the assembly of the HE, delivered as ready to AIDRO for the printing process. The last step was a test of the new prototype on the engine, validating in this way the output of the brief CFD simulation by StarCCM+ software.

Contents

Acknowledgments	ii
List of Figures	III
List of Tables	VIII
1 Aircraft's Engine Systems	1
1.1 M09 Engine by I.C.P. srl	1
1.2 Cooling and Lubrification System	7
1.3 Compact heat exchanger	16
1.3.1 Integration in the cooling system	18
1.3.2 Brazing and related issues	20
1.3.3 Specifications of the actual heat exchanger	24
1.3.4 Performance of the engine: temperature and pressure loss . .	28
2 Innovative Heat Transfer Surface Area and recent study to enhance HE performance	34
2.1 Plate heat exchanger structures and geometry	36
2.2 Recent developments and new type plate heat hexchanger	39
2.3 New compound corrugation plates: sinusoidal surface	42
2.4 A brief review of trabecular and lattice struct. for HE design	51
3 Design for AM: value chain to develop an innovative prototype	57
3.1 Novel heat exchanger (HX) core: CAD design	58
3.1.1 Material for AM	63
3.1.2 Single plate design	64
3.1.3 Core layout	66

3.1.4	Weight valuation	68
3.2	Metal Additive manufacturing	72
4	HX performance and simulation by STAR CCM+ software	74
4.1	Heat Transfer Mechanism: conduction and convection	75
4.1.1	Reynolds number for water and oil side	79
4.1.2	Prandtl for water and oil side	83
4.1.3	Nusselt for water and oil side	84
4.2	ε -NTU method	88
4.2.1	LMTD method	92
4.2.2	Ntu and effectiveness method	92
5	CFD analysis for flow through in Heat exchanger	95
5.1	STAR CCM+ Modelling/Simulation	95
5.1.1	Geometry	98
5.1.2	Mesh	100
5.1.3	Mesh Outline	102
5.1.4	Wall y^+	107
5.1.5	Models and conditions	110
5.1.6	Oil side results and validation	114
5.1.7	Water side results and validation	121
6	Conclusions	127
	Bibliography	131

List of Figures

1.1	Savanna™ by I.C.P. srl	2
1.2	M09 engine installed on the aircraft.	3
1.3	M09 engine: detailed view of the propeller.	4
1.4	M09 performance as declared by I.C.P. srl	5
1.5	Performance curve of the M09 Engine.	6
1.6	3D rendering of M09 Engine, courtesy of <i>I.C.P.srl</i>	7
1.7	Cooling system, working fluid water, courtesy of <i>I.C.P.srl</i>	9
1.8	Radiator, courtesy of <i>I.C.P.srl</i>	10
1.9	Lubrication scheme, courtesy of <i>I.C.P.srl</i>	12
1.10	Temperature distribution on the external piston surface.	13
1.11	Inner turbolator, courtesy of <i>I.C.P.srl</i>	16
1.12	Actual heat exchanger, courtesy of <i>I.C.P.srl</i>	17
1.13	Detailed view of the lubrication system, heat exchanger integration.	18
1.14	Aluminum radiator, wavy fins braised, particular-5 finning wavy in sheet of aluminum;-6 flat tubes in aluminum, liquid path for coolant. [2]	19
1.15	Cross flows air-water radiator. [2]	20
1.16	Compact heat exchanger, courtesy of <i>I.C.P.srl</i>	21
1.17	Example of brazed plate heat exchanger	22
1.18	Upper view of the turbolator, courtesy of <i>I.C.P.srl</i>	25
1.19	Side view of the turbolator, courtesy of <i>I.C.P.srl</i>	26
1.20	Top view of separator, courtesy of <i>I.C.P.srl</i>	26
1.21	Top view of interface of separation, courtesy of <i>I.C.P.srl</i>	27
1.22	View of the inner channel of the heat exchanger, courtesy of <i>I.C.P.srl</i>	27

1.23	The heat exchanger is embedded into the carter of the engine, courtesy of <i>I.C.P.srl</i>	29
1.24	Mass flow rate and pressure, water circuit, courtesy of <i>I.C.P.srl</i> . . .	30
1.25	Mass flow rate and pressure, water circuit, plot, courtesy of <i>I.C.P.srl</i>	31
1.26	Mass flow rate pressure and temperature, oil circuit, courtesy of <i>I.C.P.srl</i>	32
2.1	Brief classification of heat exchanger.	35
2.2	Chevron plate shape.	37
2.3	Structure of a typical gasketed plate heat exchanger with chevron plates	37
2.4	Effect of chevron angle on heat transfer coefficient.	39
2.5	Contact points and intersections in PHEs with chevron corrugations.	41
2.6	Configurations of four different primary surfaces with: (a) conventional sinusoidal corrugation, (b) anti-phase secondary corrugation, (c) in-phase secondary corrugation and (d) full-wave rectified trough corrugation.	43
2.7	Equations describing four different primary surfaces.. . . .	43
2.8	Three dimensional configurations of four different unit cells ($P/H = 2.2$; (a) conventional sinusoidal corrugation, (b) anti-phase secondary corrugation, (c) in-phase secondary corrugation and (d) full-wave rectified trough corrugation.	44
2.9	Detailed geometrical data for the four different surfaces.	45
2.10	Variation of the normalized performance metrics as a function of P/H ; (a) Fanning friction factor and (b) Nusselt number. Variation of the normalized goodness factors as a function of P/H ; (a) volume goodness factor and (b) area goodness factor.	46
2.11	Distribution of the Nusselt number on lower corrugation plate; (a) sinusoidal model, (b) HC# 01, (c) HC# 02 and (d) HC# 03.	47
2.12	Distributions of the normal velocity component in the trough of lower plate; (a) sinusoidal model and (b) HC# 01.	48
2.13	Distribution of the local pressure coefficient for the HC# 03 with $P/H = 2.2$ and (b) boundary layer profiles near the bottom wall for the same case.	49

2.14	Local HTC distributions and standard deviations for four different P/H cases.	50
2.15	Unit cell of the different cellular topologies. a) Strut-based cellular structures, b) Skeletal-TPMS based cellular structures and c) sheet-TPMS based cellular structures.	52
2.16	3D printed cellular structured samples with different topologies fabricated using powder bed fusion and made of Maraging steel.	53
2.17	SEM images showing the powder sticking on the printed structure.	53
2.18	Heat sink dimensions at pin base for (a) Pin fin 6061, (b) Rectangle, (c) Rect RND, (d) Ellipse, (e) Lattice and (f) Isometric view of one Lattice cell.	54
2.19	SLM fabricated heat sinks, base dimensions 50 mm x 100 mm, flow in the z direction. (a) Pin fin 6061, (b) Rectangle, (c) Rect RND, (d) Ellipse, (e) Lattice and (f) close up of Lattice.	55
2.20	Pressure drop across heat sinks. SLM heat sink efficiency index.	55
2.21	Heat transfer coefficient based on heat transfer surface area.	56
3.1	value chain approach.	58
3.2	Recall of the performance of an anti-phase sinusoidal corrugated plate.	59
3.3	MATLAB [®] unit cell generation.	60
3.4	Solidworks unit cell.	62
3.5	AlSi10Mg spec. courtesy of ZARE prototipi.	63
3.6	Filling of the inner surface.	64
3.7	Comparison between current and novel surface.	65
3.8	Enlargement factor and compactness factor.	66
3.9	Core layout, inner configuration: blue-water channels; green-oil channels; black-separation surface to prevent contact between fluids.	67
3.10	Complete Core upgrade.	67
3.11	Parts weight evaluation, HX material AlSi10Mg.	69
3.12	Weight evaluation, HX material AlSi10Mg.	69
3.13	Elements of the assembly.	71
3.14	Metal 3D printing process, step by step.	73
3.15	EOS M290 printer.	73

4.1	The graph shows the variation of the conductive heat flux on the plate thickness, at different material's conductivity.	76
4.2	Variation of the thermal resistance on thickness of the plat.	77
4.3	Development of the thermal boundary conditions.	78
4.4	Geometry of the rectangular offset strip plate fins.	80
4.5	Reynolds number and plate diameter.	82
4.6	Moody's diagram.	85
4.7	Pressure drop trend at different velocity of the two fluids.	88
4.8	Calculation results of Manglik-Bergles correlation, [24].	89
4.9	Circuit thermal resistancies analogy for the two sides.	90
4.10	NTU for counter-flow heat exchanhger.	94
5.1	CFD approach for simulation.	96
5.2	Solid part considered in the simulation, periodical repetiotion in x direction.	98
5.3	Computational domain.	99
5.4	Inner turbolator section.	99
5.5	New geometry part.	100
5.6	Properties.	101
5.7	Mesh properties.	101
5.8	Mesh quality: output of the macro runned into StarCCM+.	103
5.9	Bar chart about mesh properties.	104
5.10	Volume mesh properties, macro's output.	105
5.11	Compact volume mash report.	106
5.12	Section plane across domain for more comfortable mesh visualization.	107
5.13	Conformity between prism layer and poly mesh.	107
5.14	$y+\approx 1$	108
5.15	10 layers are improved to capture the viscous sublayer near the wall, chosing a $y+\approx 1$. In the first image $y+$ range is up to 3, instead in the second one, a refinement of the thin layer prism mesh bring to reduce the $y+$ value to 0.05, involving a more accurate solution.	109
5.16	Wall $y+$: range 0-3.	109
5.17	Oil temperature.	114
5.18	Oil Pressure.	115

5.19	Oil velocity.	115
5.20	Wall $y+$ oil side.	116
5.21	Specified Wall $y+$ heat transfer coefficient.	116
5.22	Nusselt number for oil.	117
5.23	Simulation's residuals after simulation.	117
5.24	Pressure monitor: after convergence, pressure drop is steady at 174Pa.	118
5.25	Fanning friction coefficient f vs Reynolds number.	118
5.26	Heat transfer coefficient vs Reynolds number.	119
5.27	Colburn factor vs Reynold number.	119
5.28	Nusselt number vs Reynold number.	120
5.29	Error trend in f and j results.	120
5.30	Water pressure.	121
5.31	Water temperature.	122
5.32	water velocity.	122
5.33	Heat transfer coefficient, water side.	123
5.34	Wall $y+$ water side.	123
5.35	Colburn factor j vs Reynolds Number, water side.	124
5.36	Fanning friction coefficient f vs Reynolds number, water side.	124
5.37	Heat transfer coefficient for water.	125
5.38	Nusselt number vs Reynolds number, water side.	125
5.39	Residuals after simulation, water side.	126
6.1	Water side absolute pressure: $\Delta P=1.03\text{bar}$	129
6.2	New channel layout and simulation.	130

List of Tables

1.1	Corrugation's dimensions. The values in the table refer to the Solidworks CAD model, provided by <i>I.C.P.srl</i>	24
1.2	Separator's specifications. The values in the table refer to the Solidworks CAD model, provided by <i>I.C.P.srl</i> , 1.20	24
1.3	Interface's specifications. The values in the table refer to the Solidworks CAD model, provided by <i>I.C.P.srl</i> , 1.21	25
3.1	Geometry characterization of the wave-surface.	60
3.2	Unit cell Features.	61
3.3	Overall corrugated plate dimensions.	64
3.4	Corrugated plate features: one plate spec.	65
3.5	Weight optimization for the complete HX.	68
4.1	Boundary conditions and setting for conductive heat transfer on a plate.	76
4.2	Geometrical features of the actual HX inner turbolator, measured by Solidworks model.	80
4.3	Dimensionless parameters of the geometry.	81
4.4	Water channel: Reynolds number, water properties at 360K.	81
4.5	10W-50 SE oil channel: Reynolds number at 373K.	82
4.6	Prandtl number of typical substances.	83
4.7	Prandtl number for our application, water at $T = 360\text{K}$, oil at $T = 373\text{K}$	84
4.8	Nusselt number, friction factor for thermally fully developed flow regime.	84

4.9	Results: Colburn factor and Fanning factor f for the two sides, water and oil.	86
4.10	87
4.11	Resume of parameters by empirical correlation for the actual strip-fin heat exchanger.	87
4.12	Resistances of the fluids in the heat exchanger.	91
4.13	input parameters for NTU method.	93
5.1	Fluid domain spec.	99
5.2	Geometrical features of fin.	100
5.3	Water medium, y^+ estimation.	110
5.4	Enabled models for oil side.	110
5.5	Enabled models for solid.	111
5.6	Initial conditions for oil side.	111
5.7	Regions initial conditions setup.	112
5.8	Regions initial conditions setup.	112
5.9	Enabled models for water side.	112
5.10	Regions initial conditions setup.	113
6.1	Water side discrepancy about results, at $Re=6186$	128

Chapter 1

Aircraft's Engine Systems

In the following chapter is presented the engine developed by I.C.P. srl. It is installed on the leading aircraft of the company, Savannah™ (??) and the entire innovative architecture of the new propulsion system is an in-house hardware, which ensures better performances to the aircraft. In these pages the main distinctive characteristics of the engine's subsystems are resumed, and also the component taken into account for this dissertations: the heat exchanger.



1.1 M09 Engine by I.C.P. srl

The master thesis work consists of a partnership between Politecnico di Torino and I.C.P. srl, a middle-size airplanes company located in Piedmont, Castelnuovo don Bosco, Asti, exactly. My stage started in september 2018 and ended in february 2019 and during this period I have got the opportunity to work face-to-face with Icp's Engine Engineer.

I.C.P. srl started the production of airplanes in 1990s, when the company achieved a very high quality standard of production obtaining the ISO 9001 certification in

the aeronautical field. The final products of the company are the highest quality and economically accessible aircraft for all flight enthusiasts.

M09™ Engine (1.1) is the new innovative engine designed by I.C.P. The engine is a 4-stroke V90 twin cylinder engine, front flight, with displacement of 1225 cm^3 . This geometry allows shortening the engine, integrated the oil tank and yielded it more compact giving it a reduction of aerodynamic drag force.



Figure 1.1: Savanna™ by I.C.P. srl

The challenge for the design engineers was to optimize performance while reducing the consumption. M09 is characterized by low emissions and minimal environmental impact. Using fuel mapping with two lambda probes to decrease emissions and to have stoichiometric fuel-air supply. The injection works with continuous self-diagnosis.

The total weight of this engine including all the liquids, exhaust system and ready to go is 82 kg, which offers the best power/weight ratio of any LSA engines on the market. The main innovation is a fuel injection system with double lambda probes, in order to have a stoichiometric mixture air-fuel supply. Unlike other aircraft systems, the M09 has a backup system that is not fuel injected, but carbureted.

The secondary system has its own electronic system, spark plugs, generator and mechanical fuel pump. The backup system will keep the engine running even if it is disconnected from the main battery.

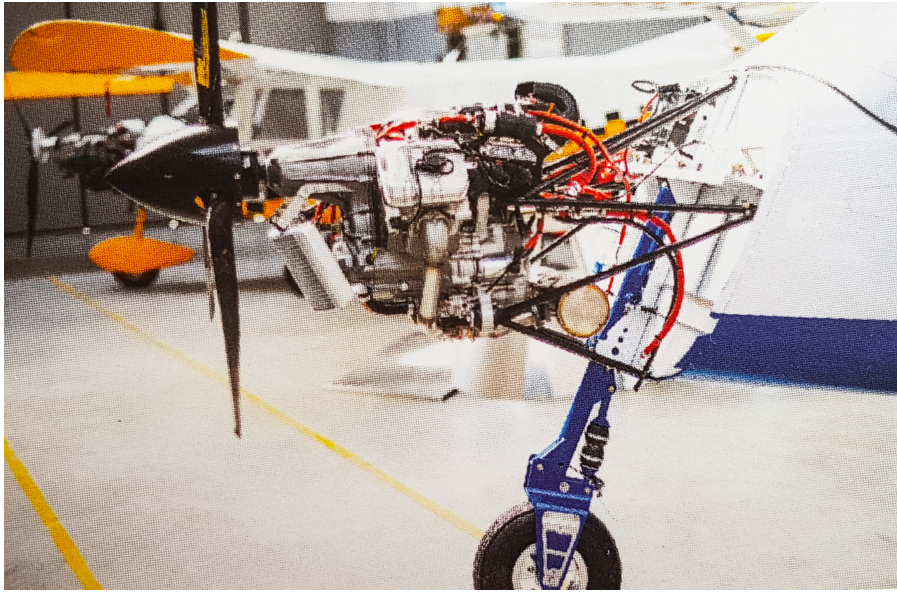


Figure 1.2: M09 engine installed on the aircraft.

The engine is excellent for compactness and bolt-on features and all the accessories are mounted ready to go.

The thrust is produced by the three blades propeller (1.3) mounted in the front side of the aircraft with a gear reduction ratio of 1:2.95. The cockpit includes an high-tech dashboard instrument EMS (5 inch. screen - monitoring Tachometer, T/P oil, Water temperature, battery level, fuel pressure, hourmeter, F.F., F.U., self diagnosis).

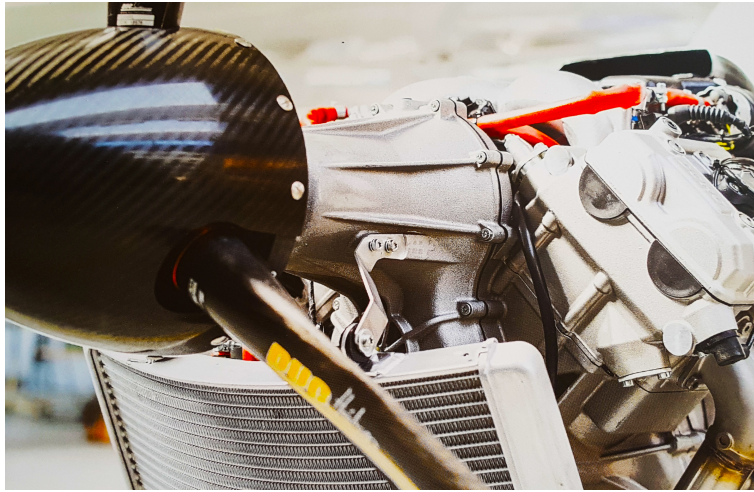


Figure 1.3: M09 engine: detailed view of the propeller.

The M09 engine performances are very interesting compared to the others direct competitors. In order to demonstrate those typical aspects are taken into account and explained several parameters such as:

- 4-stroke engine V90 twin cylinder engine: is a two-cylinder internal combustion engine, where the cylinders are arranged in a V configuration. Although widely associated with motorcycles, V-twin engines are also produced for aeronautical applications and industrial too. Assuming correct counterweighting, a 90 degree V-twin will achieve perfect primary balance; [1]
- 4-valve double overhead camshaft with the automatic decompressor;
- Liquid cooling system where the heat is subtracted by a coolant in contact with the external hotter surface of cylinder and then cooled itself passing throughout an heat exchanger, traditionally called radiator. Moreover structural ducts and passages are cutted across the main block of the engine. Generally, the coolant can be water as well as glycol;
- Dry pump with oil tank and lubrication circuit integrated into the engine;
- Double electronic Magneti Marelli (MM™) ignition;
- Primary fuel system by MM™ with two Lambda probes. This solution is suitable in order to reduce the pollution deriving from the exhaust gases pushed

out after combustion. In particular, thanks to the oxygen sensor a redox takes place, and at the end of the electro-chemical reacting process the output is an electrical signal used as feedback in a closed-loop system which allow to maintain the fuelling of the engine as near as possible to the stoichiometric fuel-air supply. As result it decrease consumption and emissions too; [2]

- Secondary fuel system: mechanical injection carburetor installed into throttle body.

M09 engine performances are listed in the table below [3] :

PERFORMANCE		
Maximum Power (5 min)	128 HP/94.4	7000 RPM
Maximum Power (sustained)	115 HP/84.5824	6600 RPM
Maximum Torque	97.4ft-lb/132.1Nm	6750 RPM
COMBUSTION CHAMBER		
Bore	4.21" / 107 mm	
Stroke	2.68" / 68 mm	
Compressor Ratio	10:01	
Displacement	1225 cm ³ /74.75 cu.in.	

Figure 1.4: M09 performance as declared by I.C.P. srl

This engine belongs to the spark ignition engines family, in which a mixture of air and petrol vapors is ignited by a spark made between the electrodes of a candle, thus achieving a lot of combustion fast (ideally at constant volume). For historical reasons these engines are also called "Otto engines". Considering the ways in which the replacement process takes place of the charge, they can be distinguished four-stroke engines, in which more than half of the work cycle (which lasts four strokes (or times) of the piston, ie two turns of shaft engine) is dedicated to the expulsion of flue gases and to the intake of the fresh charge by the piston, thus accomplishing generally a good exchange of the fluid.

The curves that characterize the behavior of an engine are those that express the driving torque and the actual power depending on the rotation speed. However, it must be kept in mind that the operating conditions can not be defined with a single operating parameter. At a given regime in fact, a motor can develop variable power

acting on the regulation organ. This, changing (Otto engine) the value of the filling coefficient (by a butterfly valve in the suction line), regulates the burnt air-gas mixture mass in each cycle; or (Diesel engine) acting on the injection pump, suitable for power required the mass of fuel injected into an air charge almost unaltered.

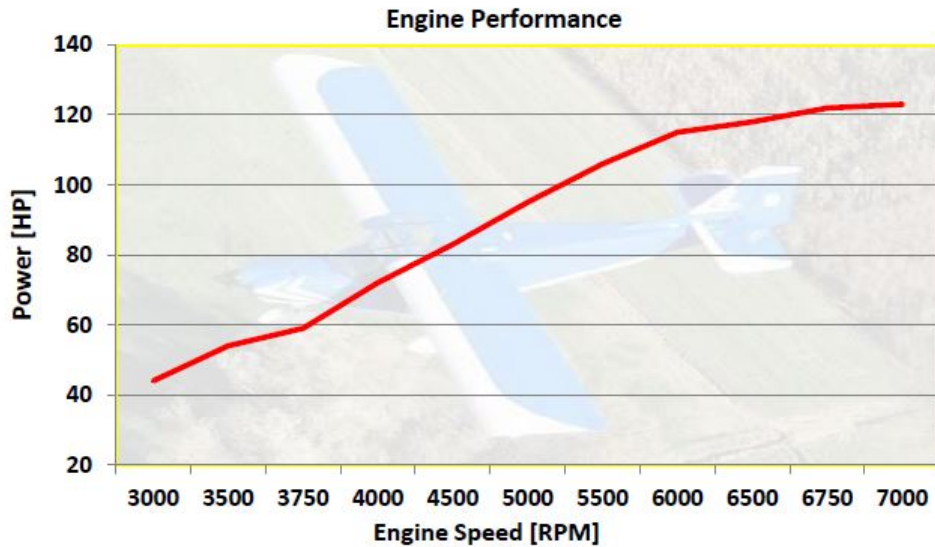


Figure 1.5: Performance curve of the M09 Engine.

Under steady-state operating conditions the parameters they define therefore the way of operating of an engine is necessarily two. Generally we use:

- the rotation speed of the crankshaft;
- the load imposed by the user.

In giving the characteristic curves, therefore, it is also necessary to indicate the load conditions to which they refer. Generally they are referred as maximum load (or full admission), because in this case the curves provide the actual limit performance that the motor can ensure.

1.2 Cooling and Lubrification System

In this section the overview of the lubrication system of the engine is proposed. The figure below shows the overall architecture of the M09, it is a 3D rendering of which this engine want to represent:

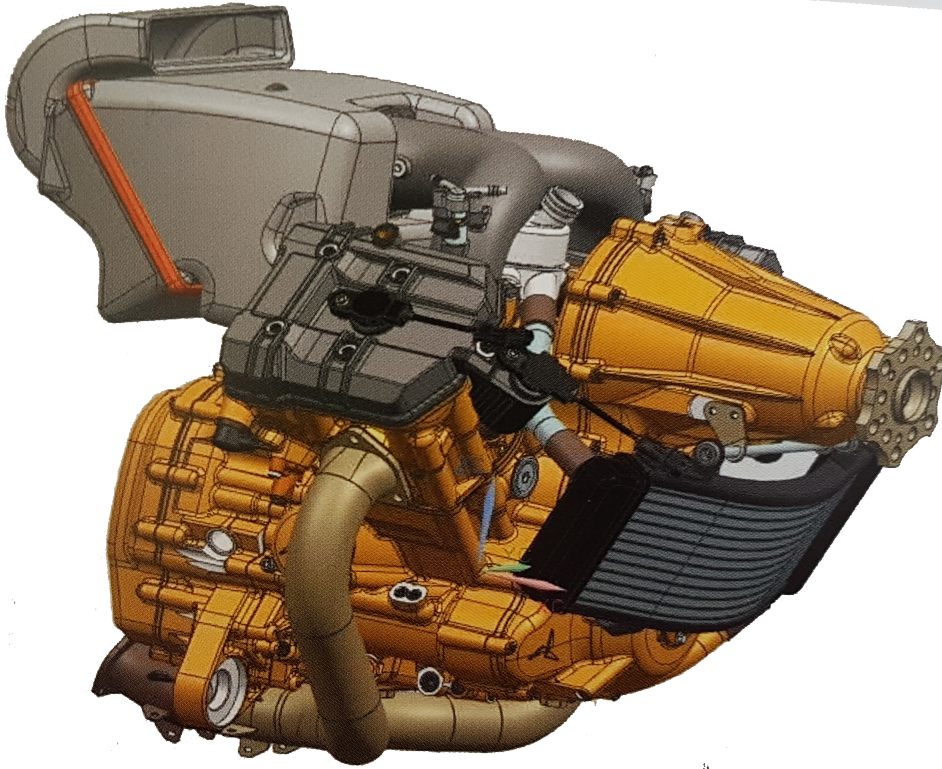


Figure 1.6: 3D rendering of M09 Engine, courtesy of *I.C.P.srl*

The purpose and the philosophy of the project is:

- Making a new aeronautical internal combustion propulsion system;
- High performance in terms of power, aircraft speed, fuel efficiency and reducing consumption;
- Low emission and environmental safety.

The figure shows: integral engine's carter, radiator and the twin-cylinder V90. At this point is necessary to introduce some concept relating to the subsystem that

include the heat exchanger. The system is divided into two linked circuit: the first one is the cooling system which has as working fluid water and the second one better named as lube system dedicated to the cooling of the cylinder absorbing heat directly by cylinders.

With liquid cooling, heat is subtracted from the cylinders wetting the refrigerant fluid immediately in contact with their surface, and releasing the heat through air conditioning and then via ambient air in a suitable heat exchanger, traditionally called radiator. The liquid, so, see only from the car to transport the heat from the small outer surface of the cylinders and the head on the large surface exposed to radiator air.

To cool the engine, cavities are created in its structure and canalizations, through which the achievement is assured of the areas most subject to heat stress by the liquid refrigerant. This generally consists of a mixture of water and ethylene glycol, to which anticorrosive additives and detergents with the aim of lowering the solidification temperature and to ensure a long life to the circuit's organs. Pressurization of the circuit, obtained thanks to the dilation of the liquid during its heating, it allows to reach the refrigerant higher temperatures, avoiding boiling. This fact allows you to reduce heat losses by cooling, without increase the dangers of overheating, and have more temperature jump between the refrigerant and the ambient air, resulting reduction of the radiator exchange surface.

The radiator is the main component of the cooling system, illustrated schematically in fig.(1.8) in one of his typical automotive application. Proper circulation of the liquid, to limit the temperature increase in the crossing of the engine, is assured by a centrifugal pump.

Water has many advantages:

- high specific heat and therefore high capacity thermal;
- low viscosity and therefore a good heat transfer coefficient e low pressure losses;
- constancy over time and with the temperature of its physico-chemical characteristics;
- high latent heat of evaporation, resulting good protection against possible

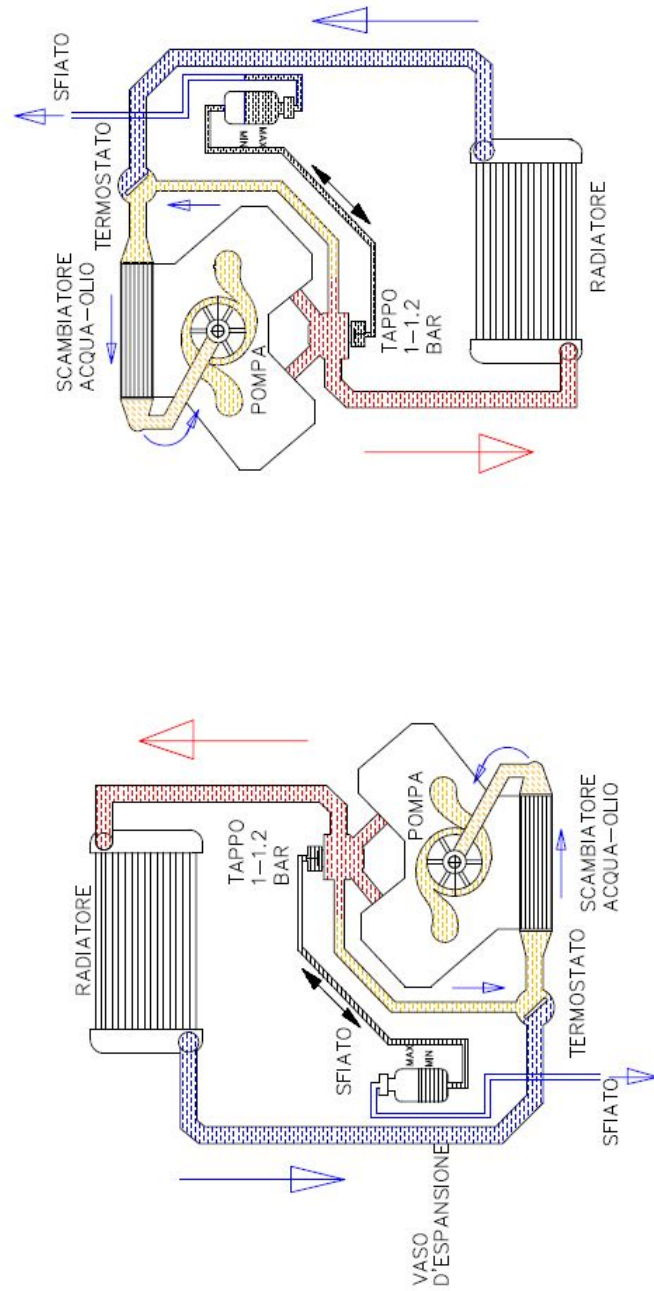


Figure 1.7: Cooling system, working fluid water, courtesy of *I.C.P.srl*

overheating of engine parts.

On the other hand, it has the following drawbacks:

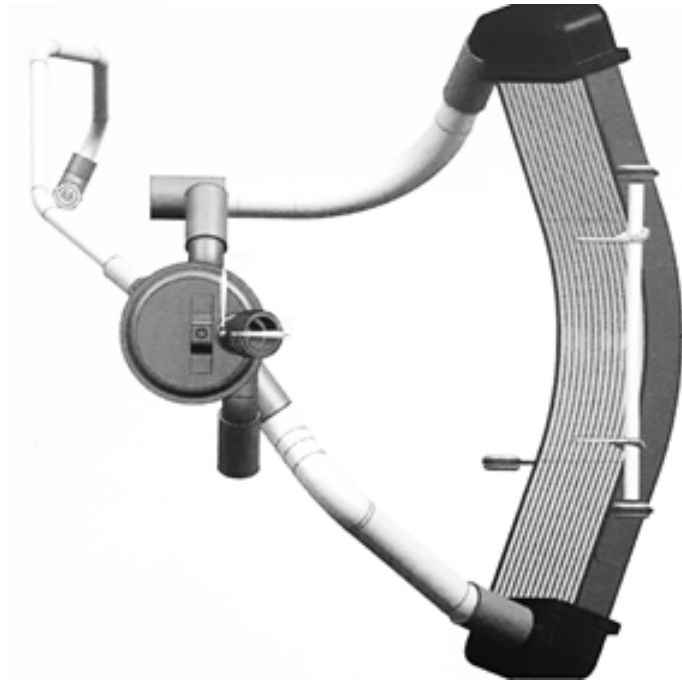


Figure 1.8: Radiator, courtesy of *I.C.P.srl*

- solidifies at a relatively low temperature high;
- has chemical aggressiveness towards some materials.

The cooling system must also guarantee, independently from the operating conditions, the maintenance of the motor at an optimal temperature value, from the point of view: control of harmful exhaust emissions and containment wear and tear of its parts.

Temperature regulation of the coolant is obtained, when it tends to fall too low, preventing with a thermostat that this (although circulating in the engine) steps into the radiator; when he risks getting up too much accentuating the heat exchange in the radiator by means of a fan: Degassing and expansion of the liquid, which increases its volume during heating, takes place in a pressurized and equipped tank of valve cap, often integrated with a radiator pan.

The specific characteristics of the radiators change quickly with the evolution of construction technologies and with the availability of new materials. However, in them one can generally distinguish: the matrix active in the heat exchange, improperly called radiant package (because the heat is transferred to the ambient air

almost exclusively by convection); two collecting trays, placed at the ends of the active block, that have the function to collect and distribute liquid. Among the numerous constructive solutions adopted to realize the matrices of exchange, here we will limit ourselves to remembering the finned tube version and that with wavy fins. The materials used (aluminum, brass, copper, etc.) present always: good thermal conductivity, ease of rolling into reduced thickness (= 0.1 mm), possibility of assembly for brazing, good resistance to corrosion against water.

It should also be borne in mind that it is usually technically found convenient to circulate the two fluids with flows simple crossed (ie with air motion through the radiant package in an orthogonal direction to that of the liquid) or, more rarely, with flows in countercurrent and crossed (ie the liquid travels part of the radiant mass in one direction, reverses the direction of motion and crosses the remaining in the opposite direction).

Now it is illustrated the lubrication system coupled with the first cooling system, as showed in the figure 1.9 below:

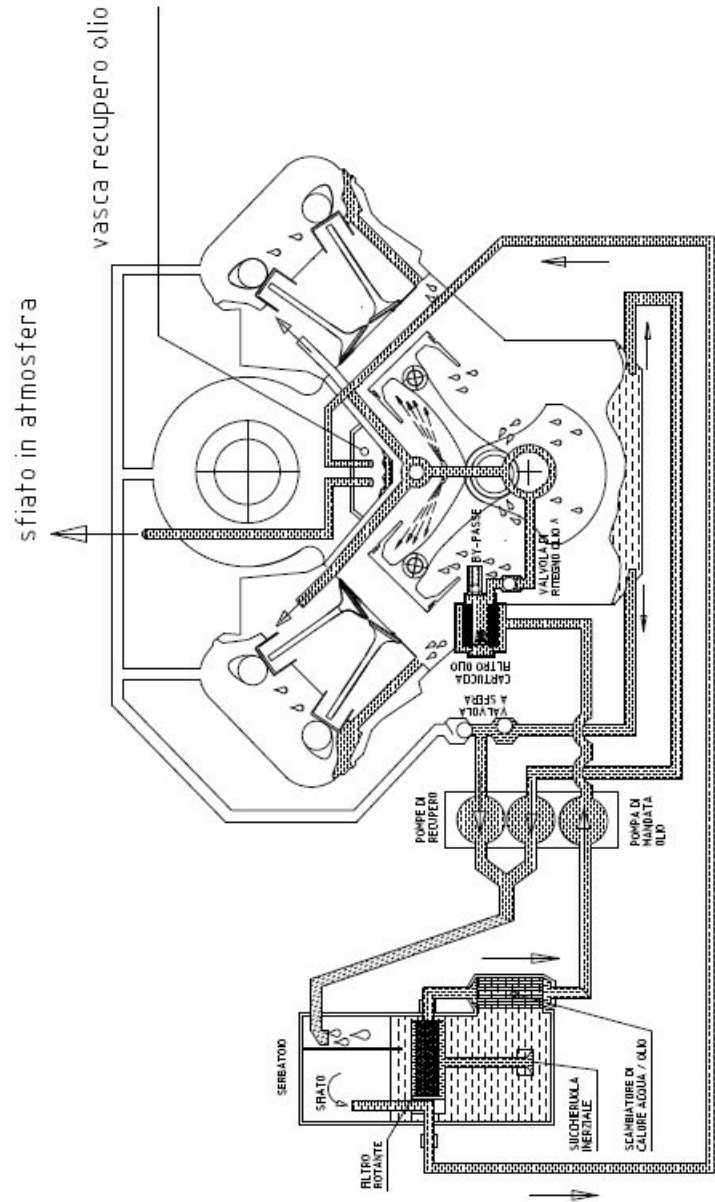


Figure 1.9: Lubrication scheme, courtesy of *I.C.P.srl*

Oil is the working fluid to lube the cylinder. It is an organ subject to an intense flow of heat coming from the gases present in the combustion chamber. About 30-40% of the total heat transmitted to the refrigerant fluid reaches the cylinder barrel through the piston. Absolute values depend mainly on the conditions of operation of the motor and the geometric dimensions of the piece. However, it can be noted that the maximum temperature values are reached in the middle of the head and gradually decrease towards the periphery and the lower part of the mantle. The low values detected in this section denotes an intense transmission of heat (50 + 60%) towards the cylinder walls, in the surface of elastic bands. A good contribution (15 + 20%) to the cooling of the piston it is also given by the jet of oil that is thrown on the inner wall of the head. In the case of pistons with obtained combustion chamber in them, the surface that receives heat is increased. Normally, the maximum temperature values are reached in correspondence of the edges of the cup, as a consequence of the high ratio exposed area to volume.

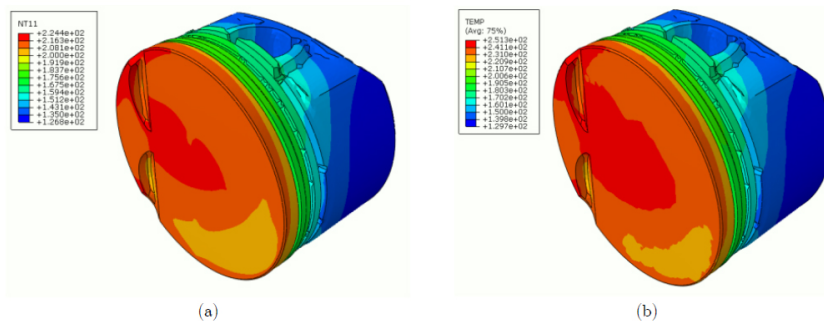


Figure 1.10: Temperature distribution on the external piston surface.

Regarding the indication of critical temperature values, should focus on the following aspects:

- points at higher temperature: limits are imposed by reasons of resistance of materials. Light alloys based on aluminum (with Cu and Si), which have undoubted advantages of: lightness, conductivity thermal and workability, can hardly be used over 350°C , because their mechanical characteristics expire quickly beyond these temperature values;
- elastic band area: to ensure good lubricant behavior and to avoid blockage of

the sealing segments in their quarries, it is necessary to avoid the temperatures in this area are too high. The values seems particularly critical correspondence of the quarry of the first band: with temperature of the order of $200 + 250^{\circ}\text{C}$ the use of oils with effective properties is required anti-sticking, while for higher values there is the danger of blocking of the segment also with oils with a high content of additives;

- bottom of the head: it is necessary to contain the temperatures, for avoid the alteration of the cooling oil and the formation of carbon deposits which accentuate the thermal insulation. For the more thermally stressed and large bore engines, cooling of the piston by pouring oil on the bottom of the head is not more sufficient and it is necessary to provide for a circulation of oil or of water in special ducts made in the head of the piston;
- mantle: performs the function of guiding the piston in the barrel of the cylinder, with respect to which must therefore present content games. Temperature variations (with the operating conditions of the engine) too high can cause excessive expansion and favor the deposit of lacquers and varnishes, facilitating the seizure of this part of the plunger in the cylinder. Typical values are : $80+100^{\circ}\text{C}$ for the lower part of the mantle; $120 + 150^{\circ}\text{C}$ for the upper part.

The maximum and minimum temperature values are reached in conditions of exercise from the inner wall of the cylinder are important from the point of view of lubrication (change of chemical and physical state of oil) and especially of adhesive and corrosive wear.

Intake valves operate at relatively low temperatures (compared to those of discharge), as they are cooled by the charge cool. However, they can reach, near the mushroom, temperatures above $300+400^{\circ}\text{C}$, sufficient to produce one decomposition and oxidation of fuel and lubricant, with formation of deposits. The exhaust valves, then, are subjected at very high temperatures and distributed unevenly, as the possibility of refrigeration is limited. Moreover, there are mechanical stresses due to the impact of the fungus on the seat and control tips on the stem. The valves are therefore subject to: deformations due to unequal thermal expansion; erosions mechanical in nature due to lack of hardness due to flow of gas; chemical corrosions due to the aggressiveness of fluids with which they come in contact

with; breakage for both corrosion and loss of hot resistance. The thermal deformations tend to exalt themselves and erosions, because they increase the escape of gas through the imperfect seals, which heat locally and corrode quickly valve and seat. To make temperature values uniformly distributed and to favor transmission the heat towards the valve stem, valves with cavities are used in the most stressed motors partially filled with metallic sodium or lithium and potassium salts.

The parts at higher temperature and more difficult to cool are also subjected to a more intense heat flow. In positive ignition engines, to ensure a correct execution of the thermodynamic cycle, it is necessary that the temperature of the internal surface of the head remains at below 200+220°C. In this case, it is possible to realize effective heat removal from the valve seats and from the valve candle, avoiding the formation of hot spots that could give rise to anomalous ignition forms.

The limitation of thermal loads serves to prevent them from being reached:

- on the one hand excessive temperature values, which lead to deformations which can affect the correct functioning of the organ (for example: piston seizure in the barrel) and / or an alteration of the lubricating properties of the oil;
- on the other, solicitations of thermal origin, due to deformations and / or at impeded expansion, too high. If, for example, in the area between the two valve seats of a cast iron head is produced (by compression) a plastic deformation, this provokes at the moment of the cold return, of the stresses (of traction) that can exceed the material breaking limit.
- Unlike mechanical stresses, which derive from forces applied to the structure, the stresses of thermal origin are provoked from expansion due to the heating of some parts. These overlap with mechanical stress and represent often the cause of broken parts of a motor subject to high heat flow.

1.3 Compact heat exchanger

Conventional aircraft engines are faced with great challenges in improving the specific fuel consumption (SFC) and reducing the size and weight of the engine core to meet increasingly stringent CO₂ and NO_x emissions regulations. To meet these demands, the aircraft engine industry is investigating advanced engine cycles that use heat exchanger technology for recuperation and/or intercooling. The development of ultra-compact heat exchanger matrices with high heat transfer and low pressure loss is essential for both intercoolers and recuperators. As J.H. Doo, M.Y. Ha and others support [4], cross-corrugated primary surface heat exchangers are proposed for application in compact thermal management systems due to their relatively high volume goodness and thus their potential for light weight designs. Since the cross-corrugated plate heat exchanger has good thermal effectiveness and aerodynamic performance, many researchers have carried out experimental and numerical studies on the aero-thermal performance of various geometrical shapes.

The actual heat exchanger is a compact plates and fins exchanger, where the space between two plates is filled up by a corrugation surface named "turbolator" (1.18).

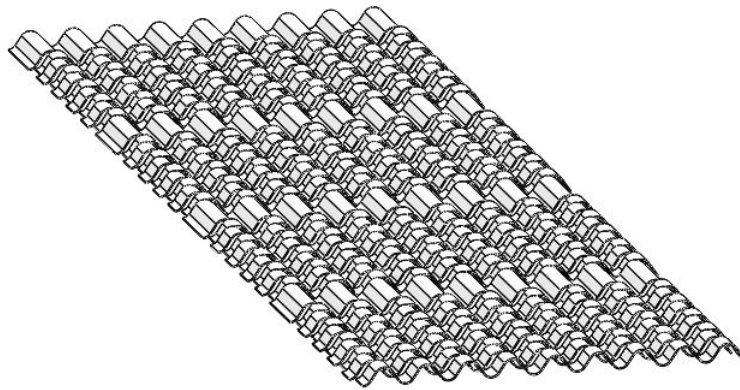


Figure 1.11: Inner turbolator, courtesy of *I.C.P.srl*

The task of this component is double, infact it should :

- Generate turbulence on viscous fluids passing through the passage between two flat plate. As the fluid flow reaches the corrugations, they create swirls and deflection on the fluid path which increase Reynold’s number associated to

the fluid regime and the main result is an augmented heat transfer coefficient realized by the exchange surfaces. (1.12)

- Moreover the solid contact between the corrugation, which could be assumed as fins developed from the surface, generate a conductive heat transfer through the exchanger.

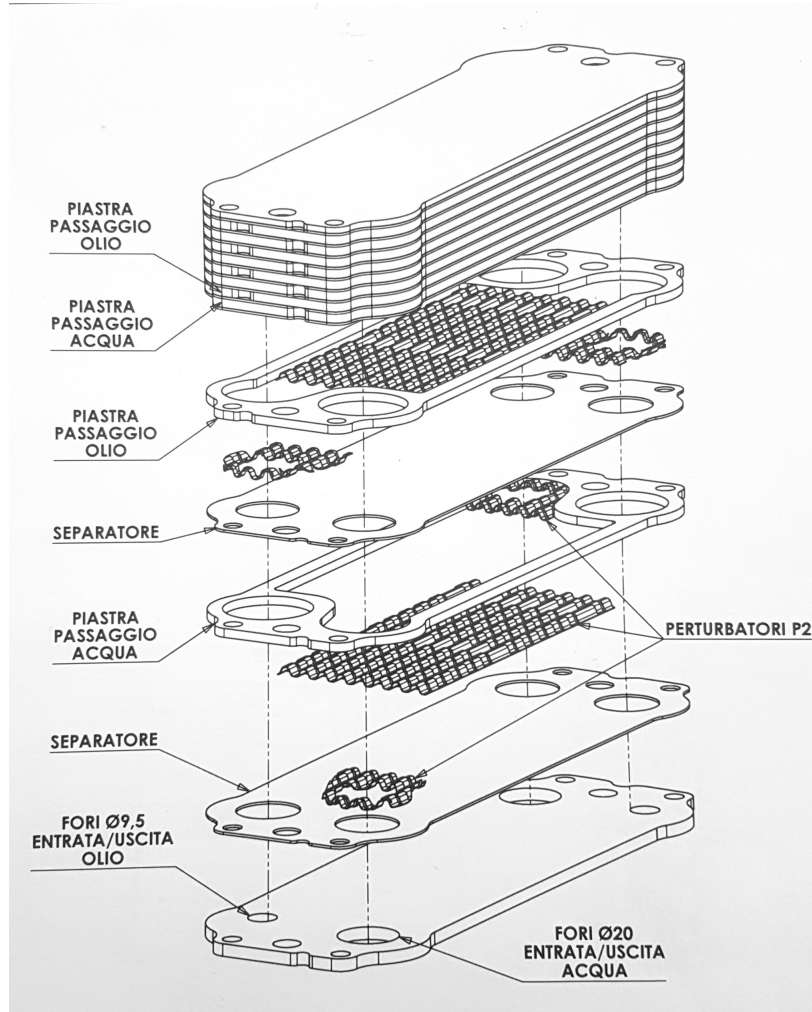


Figure 1.12: Actual heat exchanger, courtesy of *I.C.P.srl*

1.3.1 Integration in the cooling system

However, this solution is not so suitable for the aeronautical application, installed on board the aircraft engine. There are few flaws that can compromise the correct work of the heat exchanger. Before the discussion about problems and leakages, let see where the component is located on the engine and the fabrication process uses. If we now take into account the previous figure about the lubrication system, it is convenient to evaluate the detailed assembly of the system throughout zoom on a particular section (1.13):

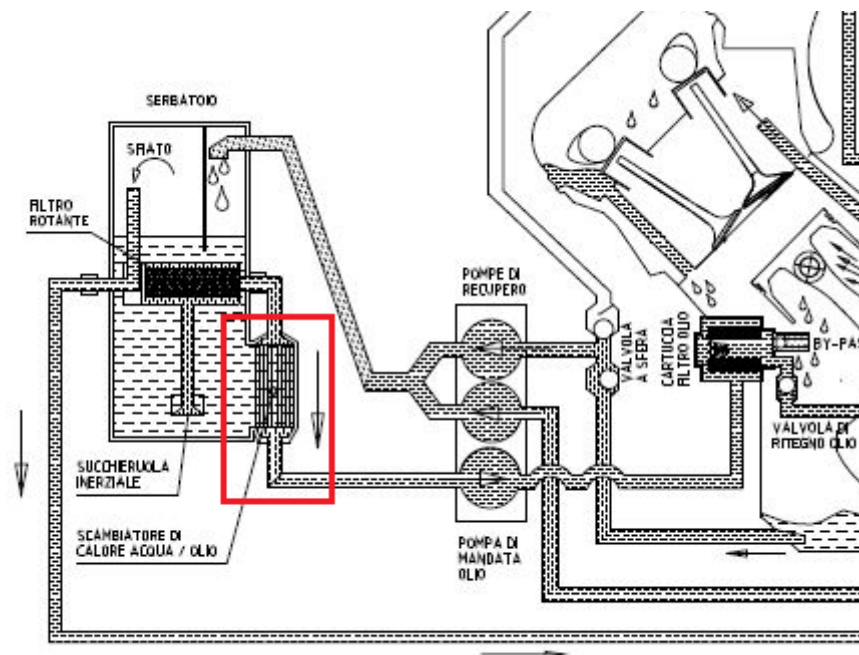


Figure 1.13: Detailed view of the lubrication system, heat exchanger integration.

As shown in the figure above, the heat exchanger is integrated in the lube system and it realizes an heat transfer between oil and water, that we can name working fluid and in particular oil fluid as primary working fluid because of its higher temperature, and then secondary working fluid for water because of its lower temperature. Starting follows the flow as soon as leaves the oil reservoir, it is pushed toward the cylinder by a dedicated pump. Before entering the ducts, the fluid is cleaned up thanks to a filter inserted on line on the pipe. At this point, the coolant is ready

to approach the cylinder, passing through a valve and at this level the process of heat transfer occurred. The external surface of the engine is reached by coolant, that collect heat originated from the hotter zone, inside of it combustion process occurred. The exchange is a convective one, the means is viscous fluid. At the outlet the oil temperature is higher than the inlet, and need to be lowered. An integrated oil tank is placed underside the engine, and here the coolant spills. This is a shelter where oil can return to the reservoir pulled by dedicated recovery pump. The most important element is the heat exchanger because is the node where the oil can be refreshed and recycled in the closed loop cooling process.(1.14):

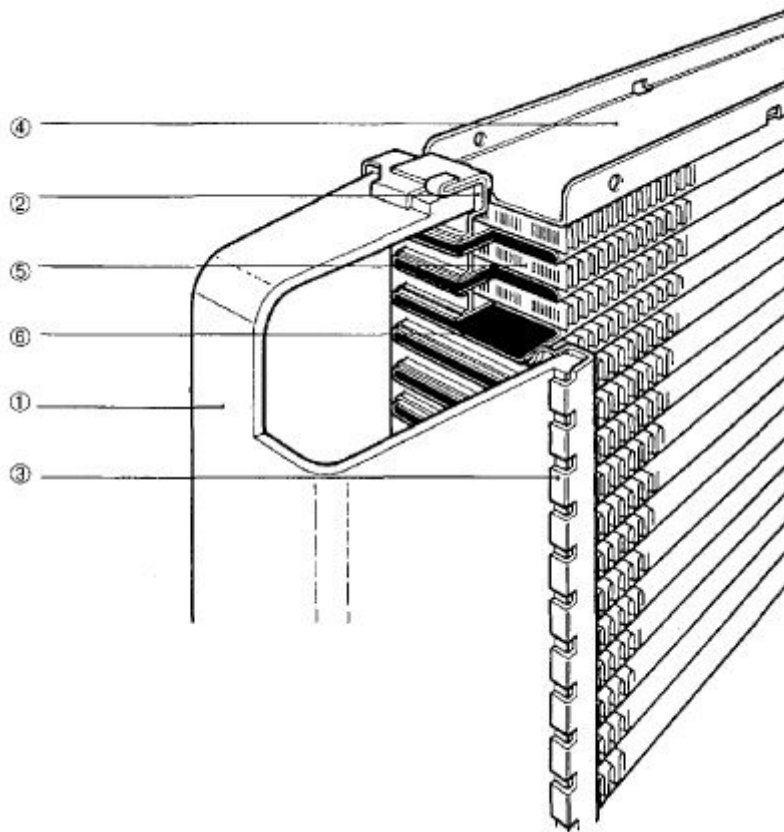


Figure 1.14: Aluminum radiator, wavy fins braised, particular-5 finning wavy in sheet of aluminum;-6 flat tubes in aluminum, liquid path for coolant. [2]

Heat transfer occurs in the heat exchanger is made by two working fluids at different temperature. Water colder than oil and for this reason the heat flux is from oil to water. The water (or glycol solution) is hotter too, but at a certain point in

the scheme, it passes through the radiator, a compact heat exchanger traditionally composed of a series of fins exposed to the incoming air from the relative motion of the airplane, as the air, that strikes on the surface absorbing heat. The result is a water that now can be used to cool the hotter oil. And this is it: the heat leave oil and warms water. Nevertheless the contact between the two working fluids does not take place thanks to the separation wall inside heat hexchanger. This excanger's type is a counterflow heat exchanger, which make better the heat transfer.(1.16) However, this will be discuss in the following paragraph.

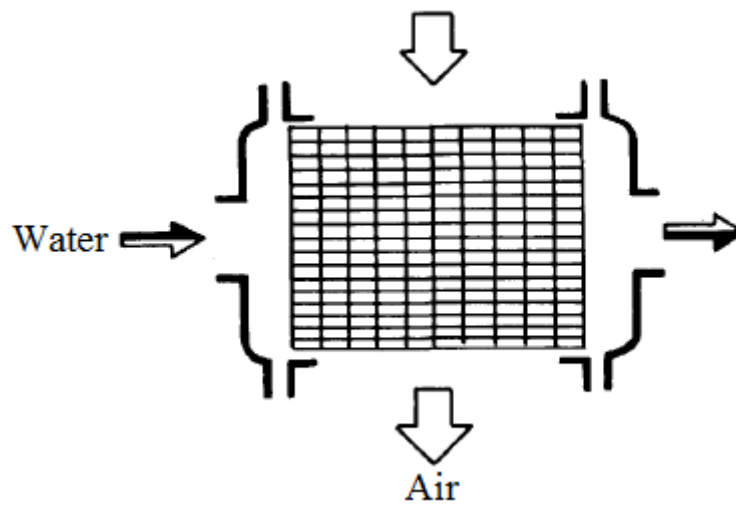


Figure 1.15: Cross flows ait-water radiator. [2]

1.3.2 Brazing and related issues

The actual heat exchanger is aluminium made and the brazing is the fabrication tecnique adopted. Unfortunately, many of the problems face in the engine's heat exchanger are referred to this method. In particular: brazing is a metal-joining process in which two or more metal items are joined together by melting and flowing a filler metal into the joint, the filler metal having a lower melting point than the adjoining metal [5]. However, brazing differs from welding in that it does not involve melting the work pieces and from soldering in using higher temperatures for a similar process, while also requiring much more closely fitted parts than when

soldering.

It is useful consider advantages and disadvantages about brazing, briefly illustrate here:

- Since brazing does not melt the base metal of the joint, it allows much tighter control over tolerances and produces a clean joint without the need for secondary finishing;
- Additionally, dissimilar metals and non-metals (i.e. metalized ceramics) can be brazed;
- Complex and multi-part assemblies can be brazed cost-effectively;
- The brazing can be coated or clad for protective purposes;
- It is easily adapted to mass production and it is easy to automate because the individual process parameters are less sensitive to variation.

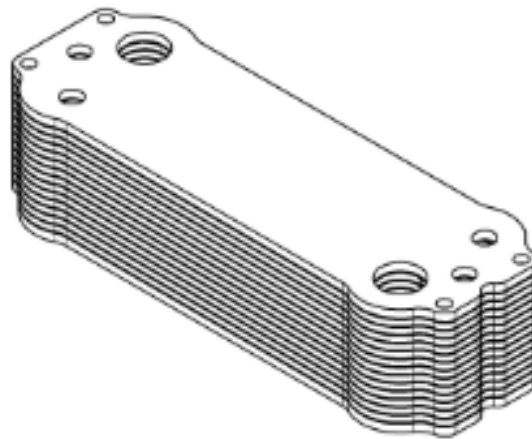


Figure 1.16: Compact heat exchanger, courtesy of *I.C.P.srl*

Inconvenience:

- One of the main disadvantages is the lack of joint strength as compared to a welded joint due to the softer filler metals used;
- brazed joints can be damaged under high service temperatures;

- Brazed joints require a high degree of base-metal cleanliness when done in an industrial setting;
- The joint color is often different from that of the base metal, creating an aesthetic disadvantage.



Figure 1.17: Example of brazed plate heat exchanger

Since brazed plate heat exchangers (1.17) offer a compact and flexible solution designed for ultra-efficient performance for high-pressure or extreme-temperature applications, they are widely adopted in industrial applications. Moreover, as advantage, operational costs are restrained. Nonetheless, high temperature and vibrations, together with a faulty brazing causes many issues in the engine's heat exchanger which require different solutions. The lack of joint strength could interrupt the conductive heat transfer, irreparably. As consequence the performance falls down. The damage of the component is inside the passages, and the inspection not so easy for the maintenance. Therefore a different approach is needed to overcome the problem and make safe and efficient the component. In this case a design for additive manufacturing allows to delete all the contact joints of the sheet, unlike the brazing process. Even if the aluminium alloy used is light, actually the heat

exchanger has a mass of 1500g which is quite remarkable if it is compared to the remaining overall engine's mass. Since additive manufacturing technology adopts aluminium alloy's powder, in particular AlSi10Mg powder with a density of 2.67 g/cm³ can reduce the weight up to one third, unlike the first one.

Another problem referred to the compact heat exchanger actually mounted on the engine is the pressure drop extremely high, because of inner turbolator, especially. The role of the turbolator is clear as explained above, but let consider some specifications and fluid interactions.

1.3.3 Specifications of the actual heat exchanger

The dimensions listed in the table below 1.1 are measured directly on the 3D cad model. The material is Aluminium alloy 1060, having a density of 2700 kg/m^3 (example suitable for the software). The surface area, volume and weight are evaluation only.

The turbolator’s geometry is sinusoidal, and appear as a periodic repetition of a sample wave between zero and maximum width. The first row is moderately out-of-face relative to the following one and the pitch is 7mm. There is a larger corrugation extended for 12.50mm named Primary corrugation and a secondary one, of 4.50mm length. However the surface is entirely covered by the secondary corrugation, and the primary is repeated just four times.

Table 1.1: Corrugation’s dimensions. The values in the table refer to the Solidworks CAD model, provided by *I.C.P.srl*

Spec.	Values [unit]	Primary Corr.	Secondary Corr.
Lenght	140 mm	12.50	4.50
Width	62.37mm		
Height	3.5mm		
Thickness	0.20 mm		
Surface	37160mm^2		
Volume	3580 mm^3		
Weight	9.67 g		

Table 1.2: Separator’s specifications. The values in the table refer to the Solidworks CAD model, provided by *I.C.P.srl*, 1.20

Spec.	Values [unit]
Lenght	141 mm
Width	60.40mm
Height	3mm
Weight	84.13 g

Table 1.3: Interface's specifications. The values in the table refer to the Solidworks CAD model, provided by *I.C.P.srl*, 1.21

Spec.	Values [unit]
Lenght	140 mm
Width	60.40mm
Height	0.60mm
Weight	8.52 g

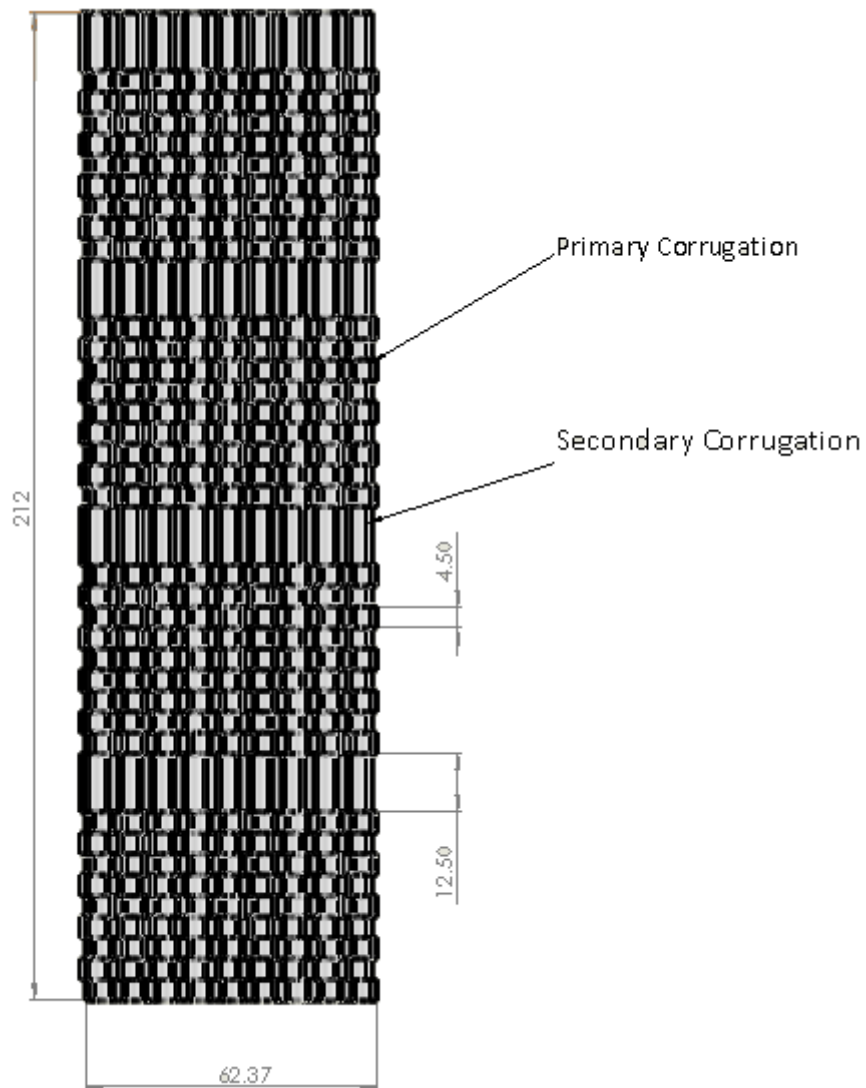


Figure 1.18: Upper view of the turbolator, courtesy of *I.C.P.srl*

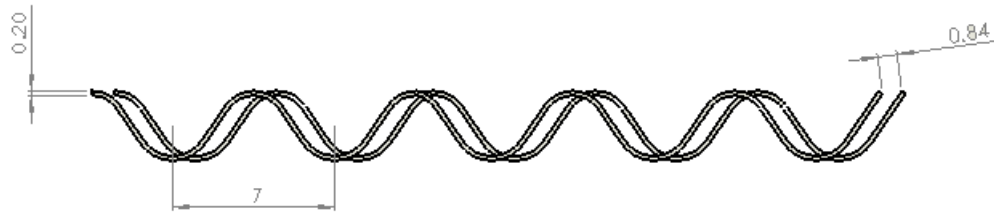


Figure 1.19: Side view of the turbolator, courtesy of *I.C.P.srl*

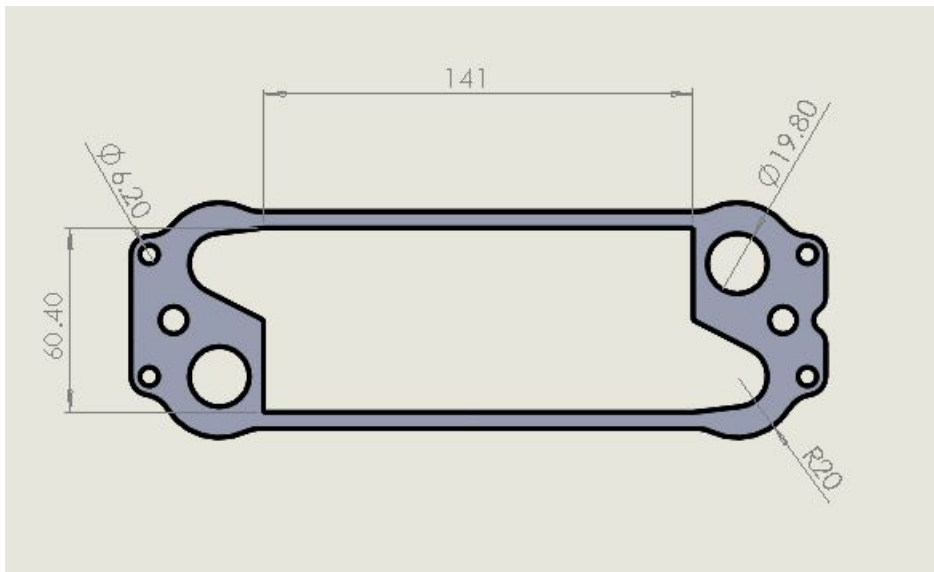


Figure 1.20: Top view of separator, courtesy of *I.C.P.srl*

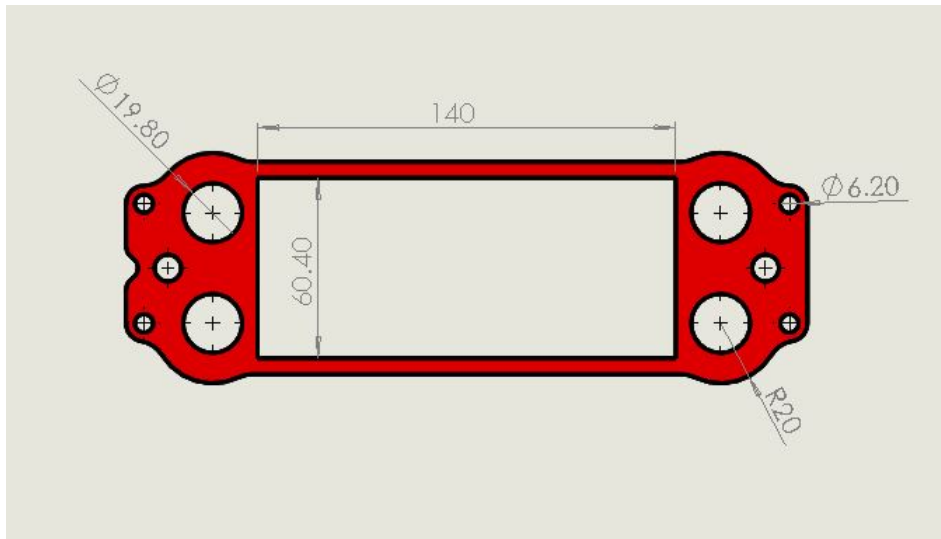


Figure 1.21: Top view of interface of separation, courtesy of *I.C.P.srl*



Figure 1.22: View of the inner channel of the heat exchanger, courtesy of *I.C.P.srl*

1.3.4 Performance of the engine: temperature and pressure loss

The main problem of the current heat exchanger is the high pressure loss in particular in the secondary working fluid: water. Additionally, too much weight: lighter the component better the overall weight of the engine. This last aspect is a goal reachable by additive manufacturing. ICP has conducted several test on the engine and has recorded all the output of the monitoring parameters in tabs, which are presented below.

In order to avoid the possibility of significant increase in pump power (constant), pressure losses must be reduced. The figure below shows the current heat exchanger, which elements are:

- 13 flow channels, 8 water passages for first circuit, 5 oil channels for secondary circuit, respectively;
- Inner turbolator for each passages, as presented above;
- Layer pitch of 3mm constant for every channels;
- Overall height of 54,4mm;
- Material aluminum alloy;
- Overall weight 1500g;
- Working pressure water-oil core 1.5bar.

Since the recess is fixed and the integration is a good solution for the engine's architecture, the heat exchanger will have the same overall dimensions even when the new design will be developed, absolutely 1.23 . In fact, taking into account this geometrical constraint, we will be sure about the perfect matching of the inner flange in front of the engine wall as well as the correct integration of the new component without modifying the engine's block, obviously.

Several test has been conducted to collect the performance of the engine, in different working conditions. When a test compaign begins, there are many and specific parameters that characterize the machine's behaviour. In this situation a choice is necessary, to reduce the parameters and monitoring the most important

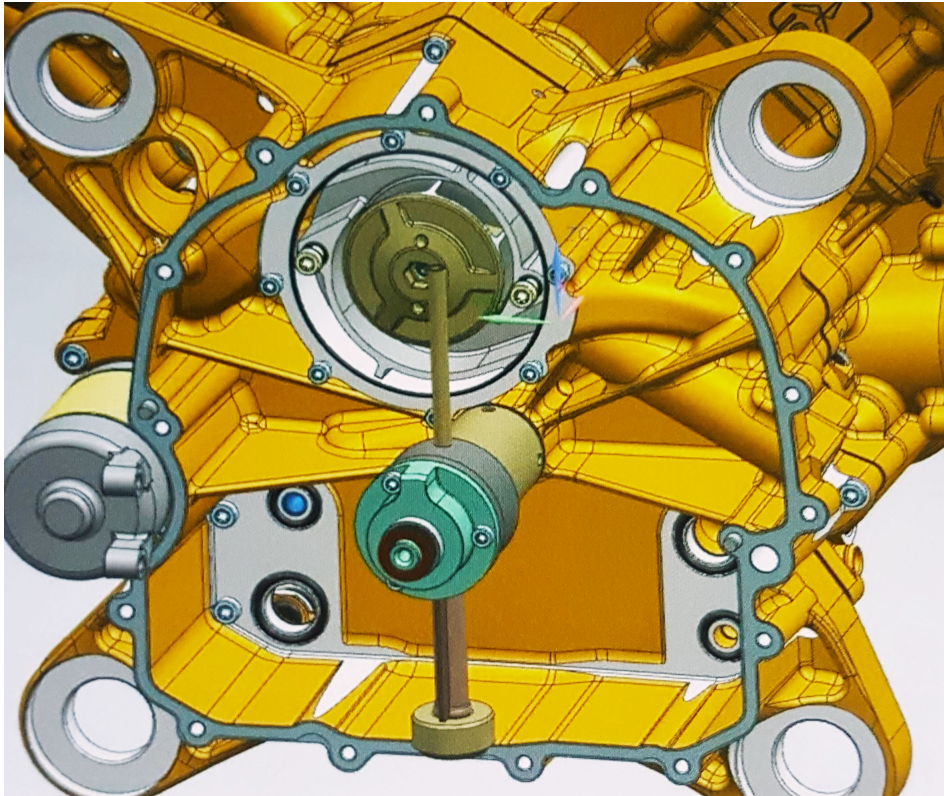


Figure 1.23: The heat exchanger is embedded into the carter of the engine, courtesy of *I.C.P.srl*

effect and performance of the engine in the worst conditions, that are, for example, the maximum power of the engine equal to the strongest working condition. Therefore, in the following tables, 1.24, are collected data refers to the different flight conditions of the airplane, such as engine's rpm, and at the same time, pressure and temperature of the cycle are monitored to extract the performance curve at fixed boundary condition.

Rilievi Portate - Pressioni scambiatore IBS Acqua

RPM	Pressione uscita testa	Portata cilindro 1	Portata cilindro 2	Portata totale	Press.Entrata		Perdita di carico	Temp. Acqua
					girante (bar)	canale Pompa		
2500	0.5	15	16	31	0.31	0.28	0.22	82
3000	0.5	18	20	38	0.24	0.21	0.29	83
3500	0.5	21.5	23.5	45	0.12	0.07	0.43	81
4000	0.5	24.5	25.5	50	-0.05	-0.1	0.60	79
4500	0.5	27.5	28.5	56	-0.17	-0.22	0.72	79
5000	0.6	28	31	59	-0.24	-0.31	0.91	80
5500	0.75	33.5	35	68.5	-0.33	-0.43	1.18	81
6000	0.9	37	36	73	-0.35	-0.4	1.30	82
6500	1.1	38.5	37.5	76	-0.35	-0.36	1.46	84
6650	1.05	38.5	37.5	76	-0.35	-0.36	1.41	83

Figure 1.24: Mass flow rate and pressure, water circuit, courtesy of *I.C.P.srl*

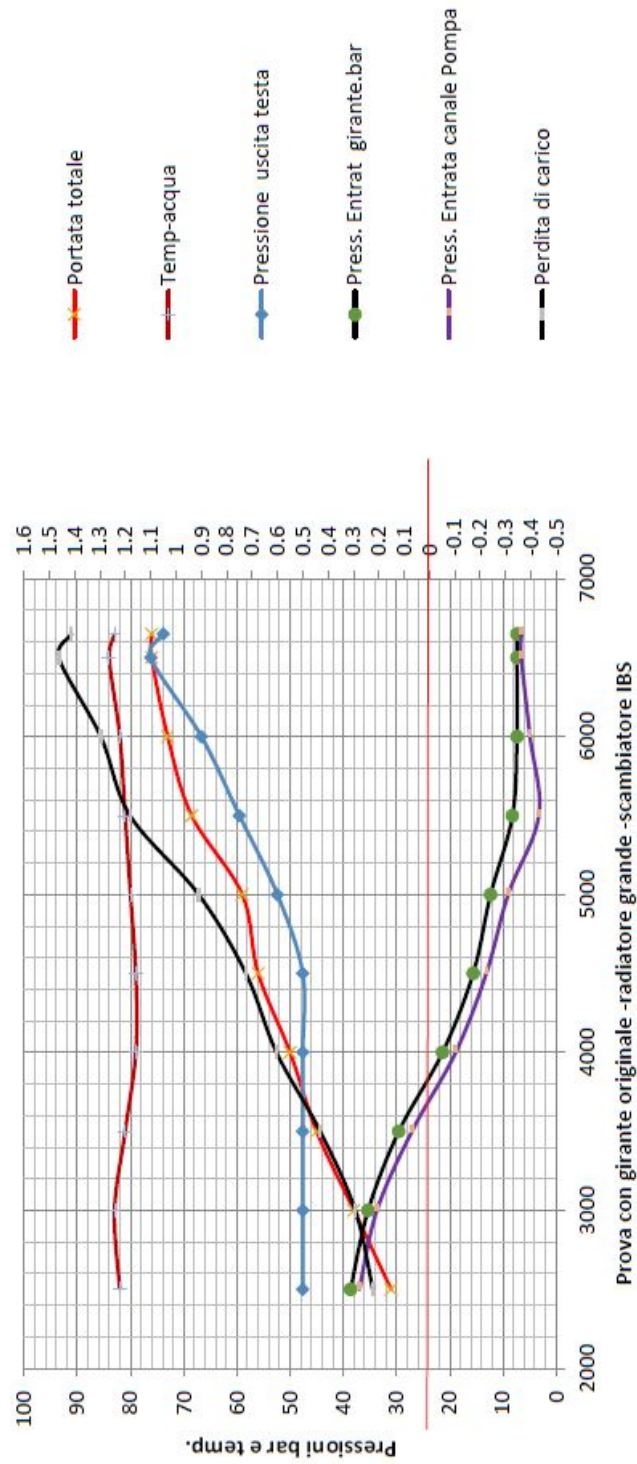


Figure 1.25: Mass flow rate and pressure, water circuit, plot, courtesy of *I.C.P.srl*

RPM	Portata olio(l/min.)	Press. uscita scambiatore(Bar)	Pressione entrata scambiatore(bar)	Temperatura olio
2000	8	-0.1	-0.001	108
2500	10	-0.15	-0.015	108
3000	11.5	-0.2	-0.032	109
3500	13.5	-0.23	-0.03	110
4000	15.8	-0.26	-0.025	111
4500	17.8	-0.3	-0.01	111
5000	19.7	-0.33	-0.01	113
5500	21.7	-0.36	-0.005	113
6000	23.5	-0.38	-0.008	114
6500	25	-0.39	-0.035	115
7000	26	-0.4	-0.02	115

Rilievi Portate - Pressioni scambiatore IBS Olio

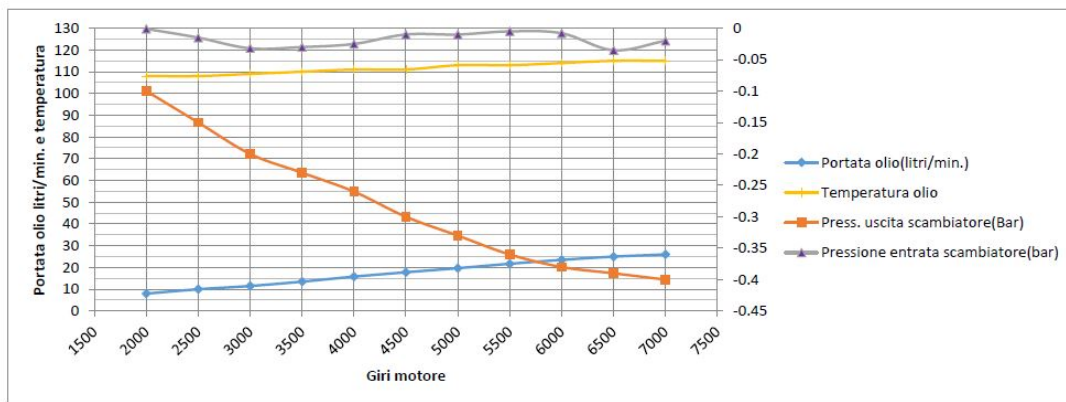


Figure 1.26: Mass flow rate pressure and temperature, oil circuit, courtesy of *I.C.P.srl*

In water circuit is interesting the pressure loss of 1.41, the highest value recorded at 6650rpm and this parameter is too high. Although the power supply by the pump is fixed, reduction of the pressure loss on the heat exchanger is required. This means that a new core geometry can involve better working condition and performance too, so the main task at this point is researching and designing innovative core solution which overcome the represented issue.

Chapter 2

Innovative Heat Transfer Surface Area and recent study to enhance HE performance

Heat exchangers are crucial in thermal science and engineering because of their essential role across the landscape of technology, from geothermal and fossil power generation to refrigeration, desalination, and air conditioning ([7]). In the aviation engineering, they have a fundamental role especially in reducing the temperatures of the fuel and thus increasing the efficiency of the aircraft engines. The literature on aviation heat exchangers is voluminous and continues to be updated today. Two main aspects of this class of flow systems are widely investigated: fluid flow and heat transfer performances, and criteria for evaluating those performances. In addition, the need of a smart and light equipment to be used inside a transport system is ever and ever felt. This requires a particular attention in the selection of components, for example in the engine zone, not only to reduce the weight but also to improve the whole heat transfer efficiency. With this aim, engineers focus their attention on new materials, for example porous materials, that recently have attracted researchers.

Heat exchangers are a fundamental tool in the thermal engineering fields, such as refrigeration, power systems cooling, electronics cooling, and air conditioning. Enhanced heat transfer (EHT) techniques provide:

- Reduction in thermal resistance of a conventional design with or without increase of surface area (as obtained from extended/fin surfaces);
- Passive enhancement, commonly used;
- Active enhancement, direct input of external power;
- Mode of heat transfer and flow regime;
- Single or two phase flow, free or forced convection, laminar, or turbulent flow;
- Type of application (two-fluid HE vs. single fluid HE).

The development of heat exchangers design, reliability and maintainability is always a required matter to enhance the overall systems performance. The heat exchangers have many different types, like; shell and tube (vertical/horizontal), plate heat exchanger (corrugated or flat - gasketed or brazed) and micro heat exchangers.

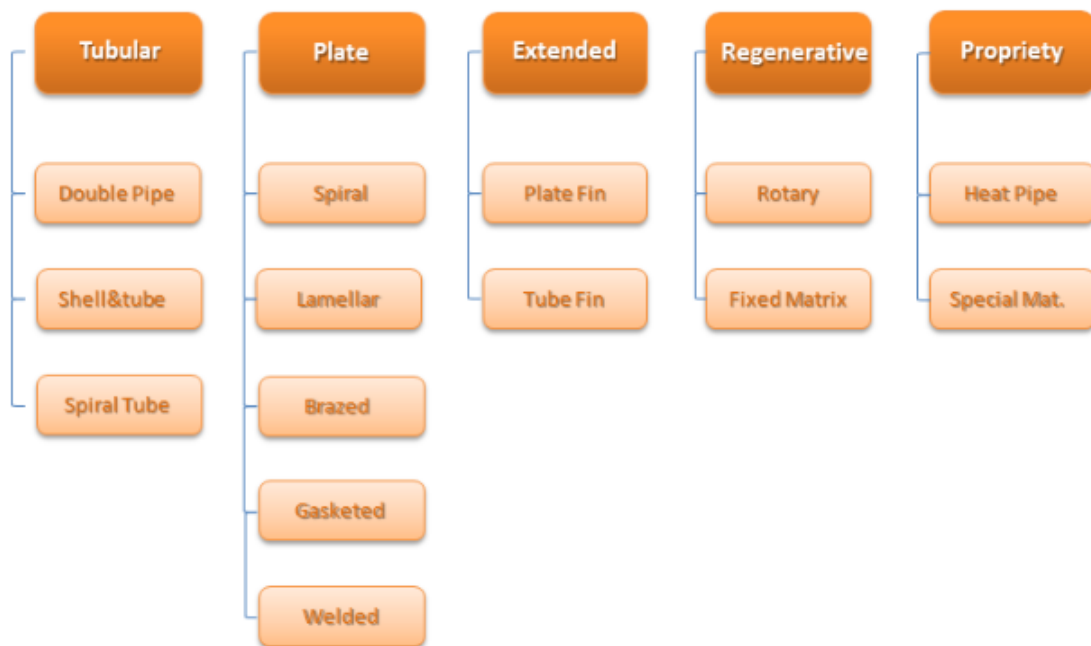


Figure 2.1: Brief classification of heat exchanger.

Two main categories of heat exchangers could be considered, the direct heat exchanger and the indirect heat exchanger. In a direct heat exchanger, the two

mediums between which heat is exchanged are in direct contact, e.g. cooling towers. In an indirect heat exchanger, the two mediums between which heat is exchanged are separated by a wall as in plate heat exchanger. The classical method for the heat exchanger design is known as The LMTD (Log Mean Temperature Difference) and NTU (Number of Transfer Units) method. These methods are based on iterations and prototype assumptions through the design. Due to these reasons, Computational Fluid Dynamics (CFD) techniques are adopted in the design of heat exchangers.

2.1 Plate heat exchanger structures and geometry

Enhancement of heat transfer surfaces has developed over the years, and is the main focus in the heat exchanger industry. Enhanced surfaces yield higher heat transfer coefficient when compared to unenhanced surfaces. A surface can be enhanced by adding extended surfaces (e.g. fins), or employing interrupted surfaces (e.g. corrugations). The plate type heat exchangers are economic and efficient enough to be widely spread in many markets now days. With it's low cost, flexibility, easy maintenance, and high thermal efficiency. The plate proven design is the main parameter for its high efficiency. In addition to the plate efficiency, corrugation patterns that produce turbulent flows, it is not only cause's unmatched efficiency ([8]); it also produces a heat exchanger self-cleaning nature, which in turn reducing the fouling effect [9]. The most common surface pattern used is the chevron design as figure 2.2 shows:

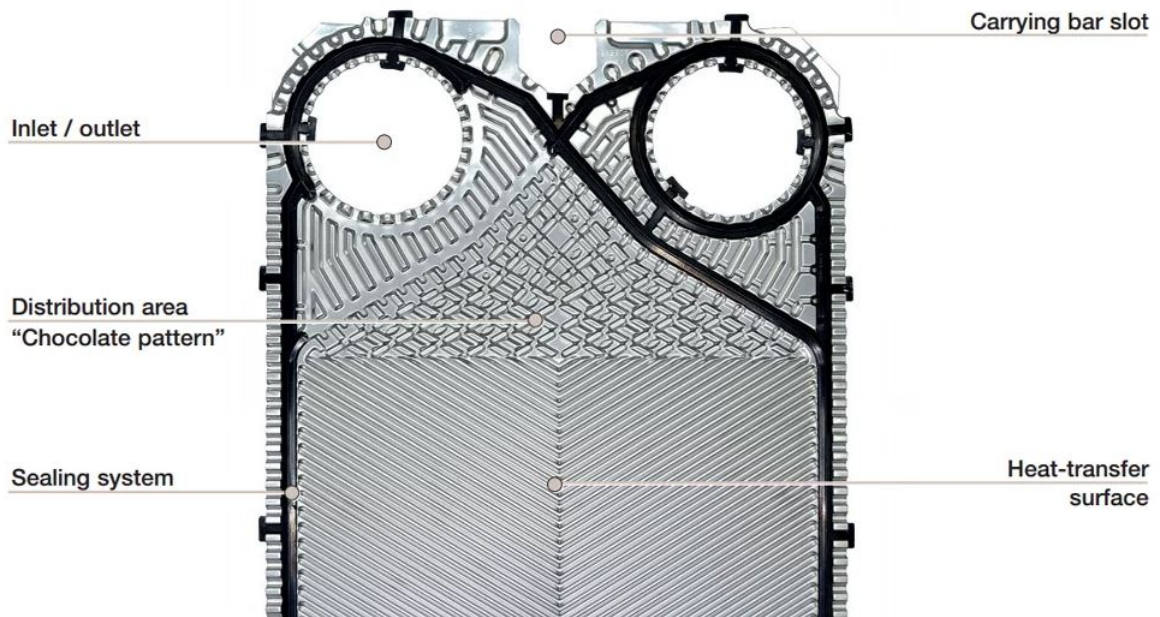


Figure 2.2: Chevron plate shape.

The corrugated plate heat exchanger consists of a number of gasketed plates constrained between an upper carrying bar and a lower guide bar. The plates are compressed between the fixed frame and the movable frame by using many tie bolts. The Structure of a typical gasketed plate heat exchanger with chevron plates is shown 2.3 :

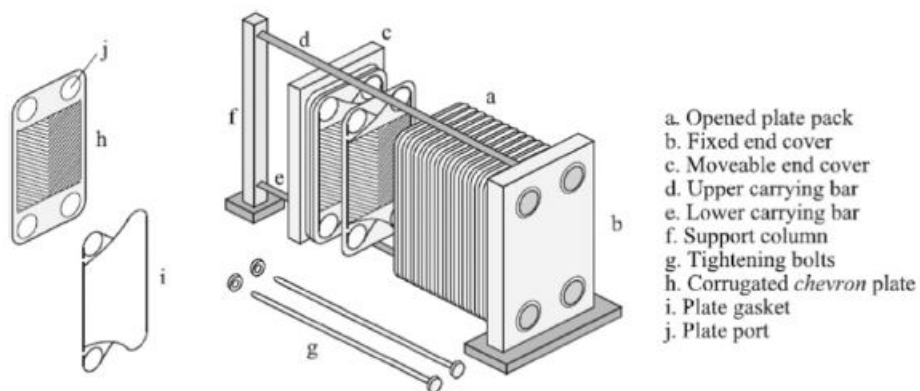


Figure 2.3: Structure of a typical gasketed plate heat exchanger with chevron plates

The important geometrical parameters for a plate heat exchanger are introduced. They are considered essential parameters in plate heat exchanger simulations, the chevron angle ψ , the corrugation depth b and the corrugation pitch p . It has been convenient also to define the parameter *Surfaceenlargementfactor* ϕ . Commercial plates have commonly surface enlargement factor of 1.15-1.25.

Thermal-hydraulic parameters are:

- Reynolds number Re ;
- Nusselt number Nu ;
- Friction factor f ;
- Equivalent diameter D ;

Where the parameter are defined respectively:

$$Re = \frac{\rho u_m D}{\nu} = \frac{GD}{\mu} \quad (2.1)$$

$$Nu = \frac{\alpha D}{\lambda} \quad (2.2)$$

$$f = \frac{\rho \Delta P D}{2L_p G^2} \quad (2.3)$$

Martin (1996) developed his heat transfer correlation by extending the Leveque theory into turbulent regime. Lee et al. (2000) [12] investigated the influence of the plate length to the plate width ratio (Aspect Ratio) on the overall heat transfer and pressure drop:

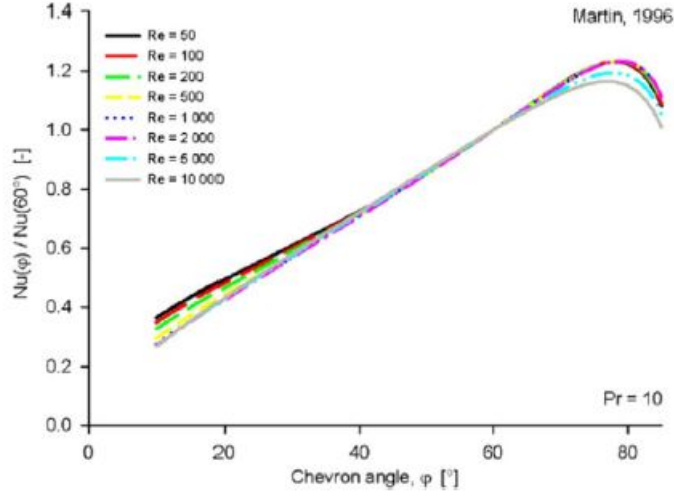


Figure 2.4: Effect of chevron angle on heat transfer coefficient.

Three different plates, with two different lengths and two different widths, were investigated. They found that, the width of the plate is the main parameter affecting the frictional pressure drop performance, since a large part of the heat exchanger is used for distributing the flow across the width of the plate for a wider plate having the same plate length. The ports pressure drop is also important:

$$\Delta P_{manif,ports} = 1.5 \left(\frac{G^2}{2\rho} \right) N \quad (2.4)$$

2.2 Recent developments and new type plate heat exchanger

The developments and the enhancements in all the heat transfer equipments are mainly purposed for energy savings and savings in projects capital investment, through reducing the costs (energy or material). The better heat exchanger is one that transfer's high heat rate at low pumping power with a minimum cost. The spent of money for the research and development in corrugated plate heat exchangers, in last decades, from some companies, offered different and versatile types and models of that heat exchanger.

This type of heat exchangers is widely used for different engineering fields and

applications. Research reactors represent one of the important engineering fields that extensively use corrugated plate heat exchangers due to their simplicity in assembly/disassembly and their easy maintainability. The corrugated plate heat exchanger has a great flexibility than the other types of heat exchangers;

Cross-corrugated primary surface heat exchangers are proposed for such applications due to their relatively high volume goodness and thus the potential for light weight designs. A new-type corrugation Plate Heat Exchanger (PHE) was designed. Results from both numerical simulations and experiments showed that the flow resistance of the working fluid in this new corrugation PHE, compared with the traditional chevron-type one, was decreased by more than 50%, and corresponding heat transfer performance was decreased by about 25% [13]. The flow field of the working fluid in the corrugation PHE was transformed and hence performance difference in both flow resistance and heat transfer was generated. Such a novel plate, consisting of longitudinal and transverse corrugations, can effectively avoid the problem of flow path blockage, which will help to extend the application of PHEs to the situation with unclean working fluids.

Problems related to the chevron-type plate heat exchanger:

- Fouling
- Path blockage
- Energy consumption
- Cleaning
- Large flow resistance

To support the disadvantage of fouling it should be considered the mechanism which make critical this aspect. It is splitted in: particulate fouling, or the accumulation of solid particles suspended in the process stream on the heat transfer surfaces such as dust deposition, particles carried in condenser cooling water, and unburned fuel. Then there is the precipitation fuoling made out by dissolved substances carried in the process stream are precipitated on the heat transfer surfaces. Examples include carbonates, sulfates, and carbonates. All this aspects and more others referred to chemical reaction contribute to increase the pumping power demand and decrease the efficiency of the heat exchanger too, because of an increased

thermal resistance.

The majority of plate corrugations in PHEs are in the form of chevron because of its relatively simple manufacture. Two neighboring plates are stacked and then some network-shaped contact points are formed. These contact points are acting as supporting plates and forming flow channels for working fluid between plates. Frequently those dirty matters will spread in all directions and eventually cause flow path blockage, thus excessive energy consumption will occur. In the chevron PHE, some intersections can be generated when the working fluid is flowing along the corrugation direction in the space formed by two neighboring plates. These intersections 2.3 and contact points are distributed in a cross way, which can on one hand enhance heat transfer through increasing the strength of flow turbulence and on the other hand increase the flow resistance [14] . This is the reason why the chevron type PHE is often assigned an obviously large flow resistance than that of the others.

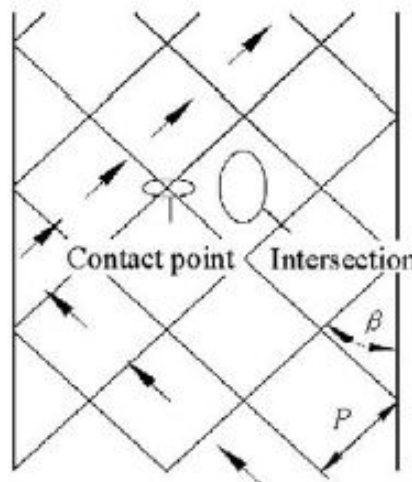


Figure 2.5: Contact points and intersections in PHEs with chevron corrugations.

2.3 New compound corrugation plates: sinusoidal surface

Four different configured surfaces are illustrated in 2.6 . The important modelling results introduced by J.H. Doo et al. (2012) [15], showed that, compared to the conventional sinusoidal model, a pressure drop reduction of approximately 15% was predicted for both the anti-phase and the full wave rectified secondary corrugation models (HC# 01 and HC# 03) with $P/H=2.2$ and θ (intersecting angle) $=90^\circ$, with small changes to the predicted heat transfer capacity. The pressure drop of the in-phase secondary corrugation (HC# 02) was predicted to increase by approximately +38%, and heat transfer capacity was enhanced by approximately +7%.

The detailed geometrical data of these four different cross-corrugated plates are summarized in following fig 2.7.

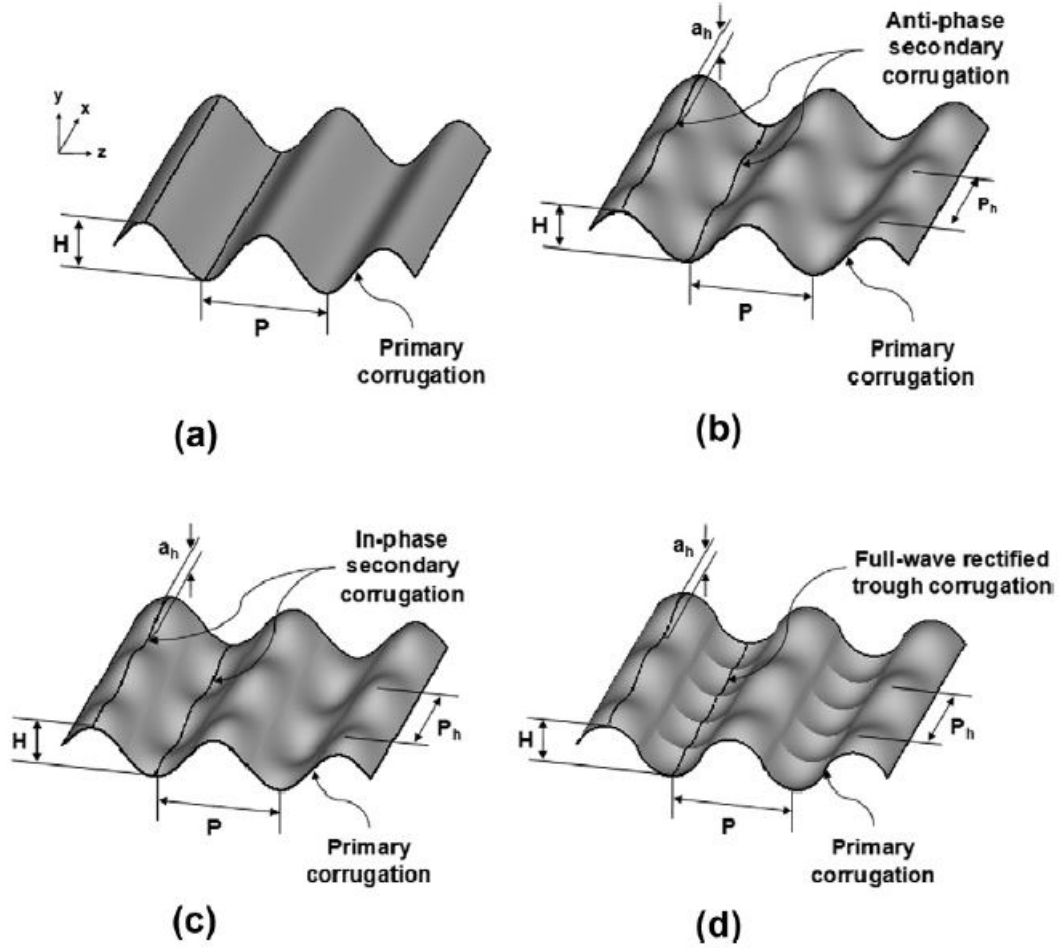


Figure 2.6: Configurations of four different primary surfaces with: (a) conventional sinusoidal corrugation, (b) anti-phase secondary corrugation, (c) in-phase secondary corrugation and (d) full-wave rectified trough corrugation.

Profile	Equation	
Sinusoidal corrugation	$y(x, z) = \frac{H}{2} \sin\left(\frac{2\pi}{P}z\right)$	(1)
Anti-phase secondary corrugation	$y(x, z) = \frac{H}{2} \left[a_h \sin\left(\frac{2\pi(x - \tan(\theta)z)}{P_h}\right) \sin\left(\frac{2\pi z}{P}\right) + (1 - a_h) \sin\left(\frac{2\pi z}{P}\right) \right]$	(2)
In-phase secondary corrugation	$y(x, z) = \frac{H}{2} \left[a_h \sin\left(\frac{2\pi(x - \tan(\theta)z)}{P_h}\right) \sin\left(\frac{2\pi z}{P}\right) + (1 - a_h) \sin\left(\frac{2\pi z}{P}\right) \right], \text{ if } \sin(2\pi z/P) \geq 0$	(3)
Full-wave rectified trough corrugation	$y(x, z) = \frac{H}{2} \left[-a_h \sin\left(\frac{2\pi(x - \tan(\theta)z)}{P_h}\right) \sin\left(\frac{2\pi z}{P}\right) + (1 - a_h) \sin\left(\frac{2\pi z}{P}\right) \right], \text{ if } \sin(2\pi z/P) < 0$	(4)
	$y(x, z) = \frac{H}{2} \left[(1 - a_h) \left(\sin\left(\frac{2\pi z}{P}\right) \right)^{2/3} + a_h \left(\sin\left(\frac{2\pi(x - \tan(\theta)z)}{P_h}\right) \times \left(\sin\left(\frac{2\pi z}{P}\right) \right)^{2/3} \right) \right], \text{ if } \sin(2\pi z/P) \geq 0$	
	$y(x, z) = -\frac{H}{2} \left[(1 - a_h) \left(\left \sin\left(\frac{2\pi z}{P}\right) \right \right)^{2/3} + a_h \left(\left \sin\left(\frac{2\pi(x - \tan(\theta)z)}{P_h}\right) \right \times \left(\left \sin\left(\frac{2\pi z}{P}\right) \right \right)^{2/3} \right) \right], \text{ if } \sin(2\pi z/P) < 0$	

Figure 2.7: Equations describing four different primary surfaces..

Where the denotations of sinusoidal, HC# 01, HC# 02 and HC# 03 represent the sinusoidal corrugation, anti-phase secondary corrugation, in-phase secondary

corrugation and full-wave rectified trough corrugation, respectively.

A CFD simulation is performed to study the effective characteristics of this innovative shape solution, defining a structured hexaedrical mesh in the computational domain. The domain consists of a unit cell beetwen two peaks where the sensitive solution is obtained meshing $064-0.78 \times 10^6$ cells. The first wall normal grid point is at $y^+ \approx 0.8$ and in the stream-wise and lateral directions the grid spacing is $\Delta x \approx 10$ and $\Delta z \approx 10$, respectively. The present unit cell calculation results are validated against existing experimental data in terms of the Fanning friction factor f and Colburn j factor.

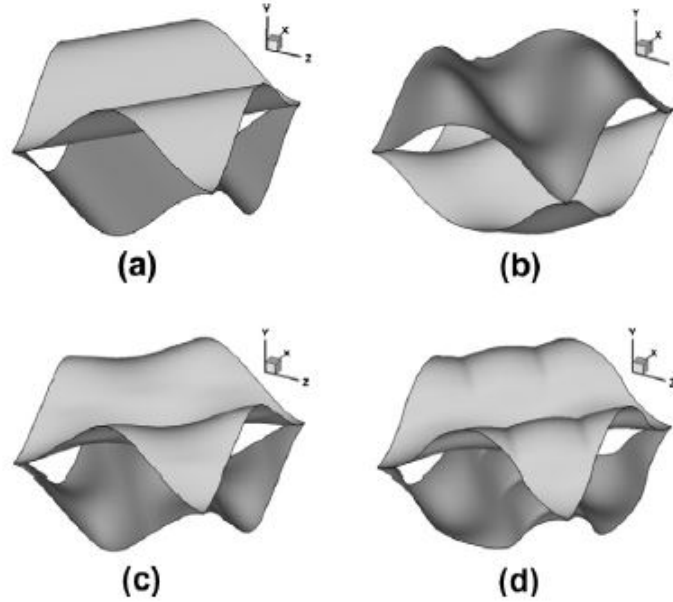


Figure 2.8: Three dimensional configurations of four different unit cells ($P/H = 2.2$; (a) conventional sinusoidal corrugation, (b) anti-phase secondary corrugation, (c) in-phase secondary corrugation and (d) full-wave rectified trough corrugation.

The Fanning friction factor f , Nusselt number Nu , Stanton number St and Colburn j factor are calculated respectively:

$$f = \frac{(\frac{\Delta p}{\Delta x}) D_h}{2\rho U_a^2} \quad (2.5)$$

$$Nu = \frac{h D_h}{k} \quad (2.6)$$

$$St = \frac{Nu}{Re \cdot Pr} \quad (2.7)$$

$$j = St \cdot Pr^{2/3} \quad (2.8)$$

Profile	P/H	θ	a_h	A_{hr}	V	D_h	C	P/H	θ	a_h	A_{hr}	V	D_h	C
Sinusoidal	1.1	90°	0	10.322	2.468	0.957	4.182	2.2	90°	0	27.025	9.873	1.462	2.737
HC#01	1.1	90°	0.2	8.856	2.401	1.084	3.689	2.2	90°	0.2	24.695	9.708	1.572	2.544
HC#02	1.1	90°	0.2	9.000	2.464	1.095	3.653	2.2	90°	0.2	24.874	9.874	1.588	2.519
HC#03	1.1	90°	0.2	9.023	2.473	1.096	3.648	2.2	90°	0.2	26.310	9.860	1.499	2.668

Figure 2.9: Detailed geometrical data for the four different surfaces.

The results show 2.10 the variations of the normalized Fanning friction factor f/f_0 and Nusselt number Nu/Nu_0 as a function of P/H at $\theta = \text{deg } 90$ where the subscript (0) denotes the sinusoidal model. For the cases with P/H=1.1 and $\theta = \text{deg } 90$, the Fanning friction factors of HC# 01 and HC# 03 are within 2.5% of the sinusoidal model and the Nusselt numbers are within 3%. However for the HC#02 case where the primary and secondary corrugations are in phase, the Fanning friction factor increased by +34.3% and the Nusselt number by +17.5%. For the cases with P/H = 2.2 and $\theta = \text{deg } 90$, the Fanning friction factors of HC# 01 and HC# 03 are substantially reduced by -4.7% and -15.2%, respectively. The Nusselt numbers are of almost the same level as for the sinusoidal corrugation with reductions of only -1.01% for HC# 01 and -3.43% for HC# 03. As before HC# 02 shows more marked changes than HC# 01 and HC# 03 with the Fanning friction factor increasing by +37.8% and the Nusselt number increasing by +6.67%. For the anti-phase secondary corrugation of HC# 01 and the full wave rectified secondary corrugation of HC# 03, the increments of the Nusselt number are higher than those of the Fanning friction factor with increasing P/H. In contrast to the in phase secondary corrugation of HC# 02, the increments of the Fanning friction factor are larger than those of the Nusselt number with increasing P/H. Even though the results for further P/Hs of 3.3 and 4.4 for three different secondary corrugation models are not included in the present study, the current results show that HC# 01 and HC# 03 have a potential for reducing the pressure drop penalty for a given heat transfer duty [23].

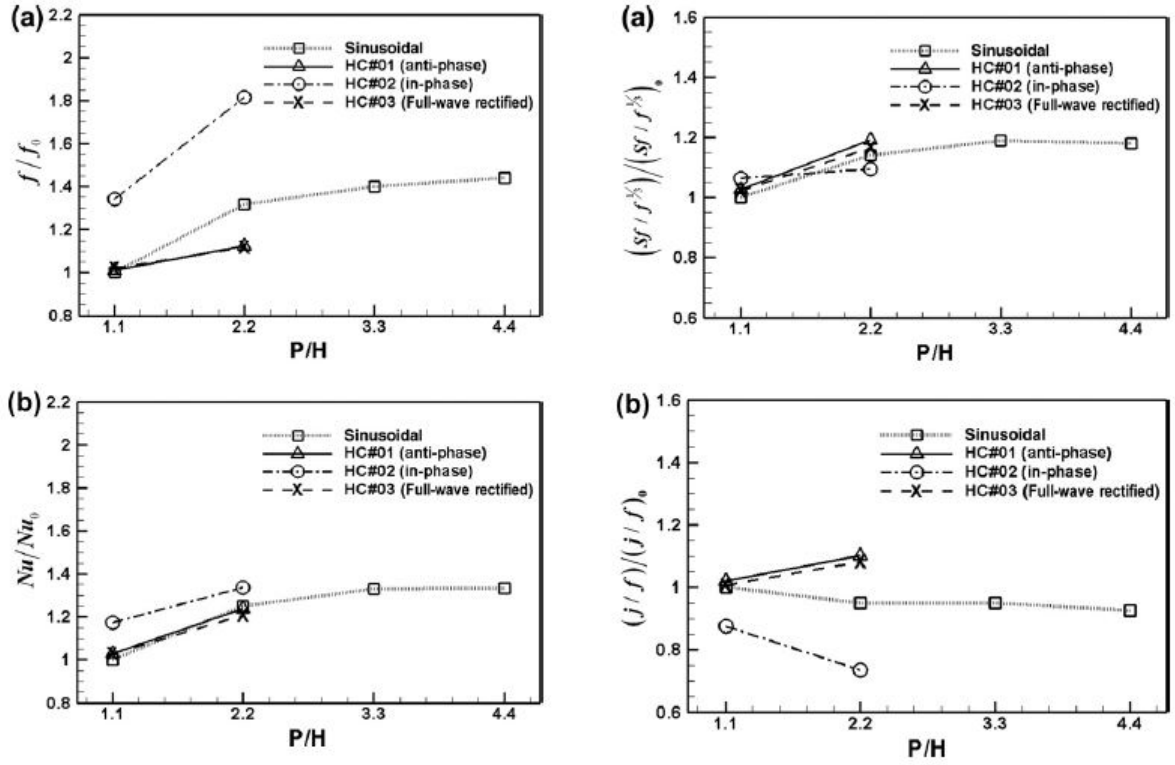


Figure 2.10: Variation of the normalized performance metrics as a function of P/H; (a) Fanning friction factor and (b) Nusselt number. Variation of the normalized goodness factors as a function of P/H; (a) volume goodness factor and (b) area goodness factor.

In Fig. 2.11, high levels of local heat transfer are observed on the upwind side of the primary corrugation followed by low levels of heat transfer on the downstream side. The heat transfer of the three different secondary corrugation models is more uniform than that of the sinusoidal model over the whole corrugation plate. The non-uniform distribution of the Nusselt number on the sinusoidal corrugation results in a non-uniform temperature distribution through the corrugated plate. The more uniform Nusselt number distribution provided by the surfaces with secondary corrugations offers potential to reduce thermal stress and transverse conduction of heat in the corrugated plate.

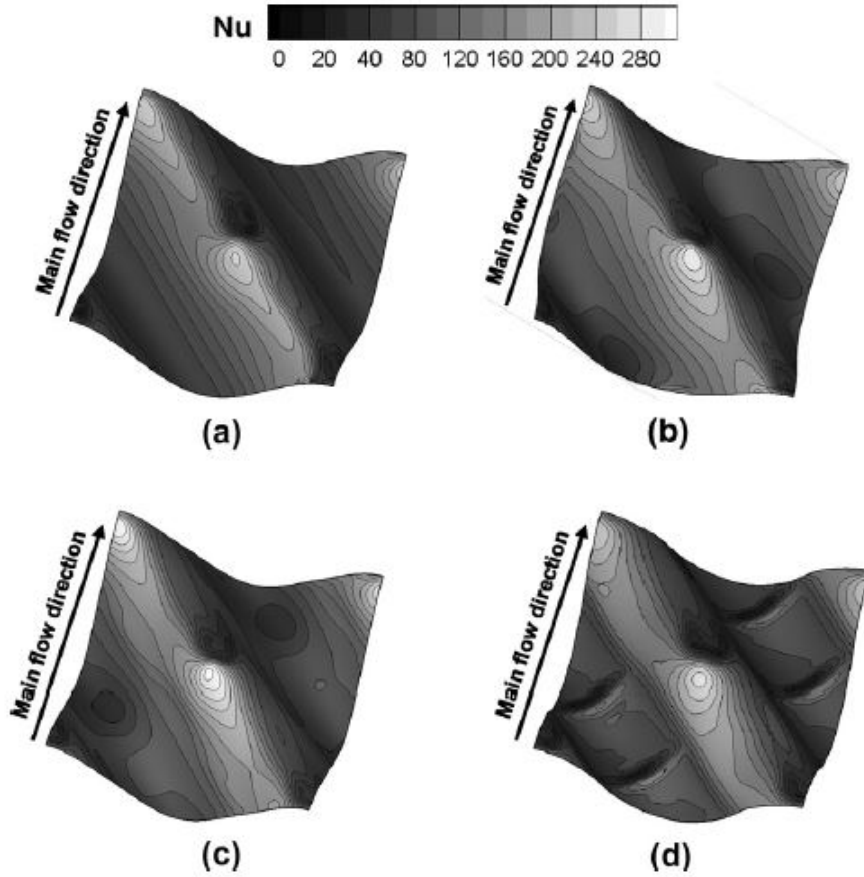


Figure 2.11: Distribution of the Nusselt number on lower corrugation plate; (a) sinusoidal model, (b) HC# 01, (c) HC# 02 and (d) HC# 03.

Fig. 2.12 (a) and (b) show the distributions of the normal velocity component (v) in the trough of the lower plate for the sinusoidal model and anti-phase secondary corrugation model (HC# 01). The normal velocity component plays an important role in the heat transport from the main core flow to the upper and lower surfaces by the large scale fluid motion. In Fig. 2.12(a), the iso-velocity lines are nearly uniformly distributed across the corrugation direction and show only a small variation in the primary corrugation direction. By contrast, the iso-velocity lines in Fig. 2.12 (b) show both positive and negative values and strong gradients indicative of the higher mixing of the flow. This result shows that the activity of the heat transport in the normal direction is strengthened in the trough of the secondary corrugation model, resulting in the enhancement of the large scale flow

mixing.

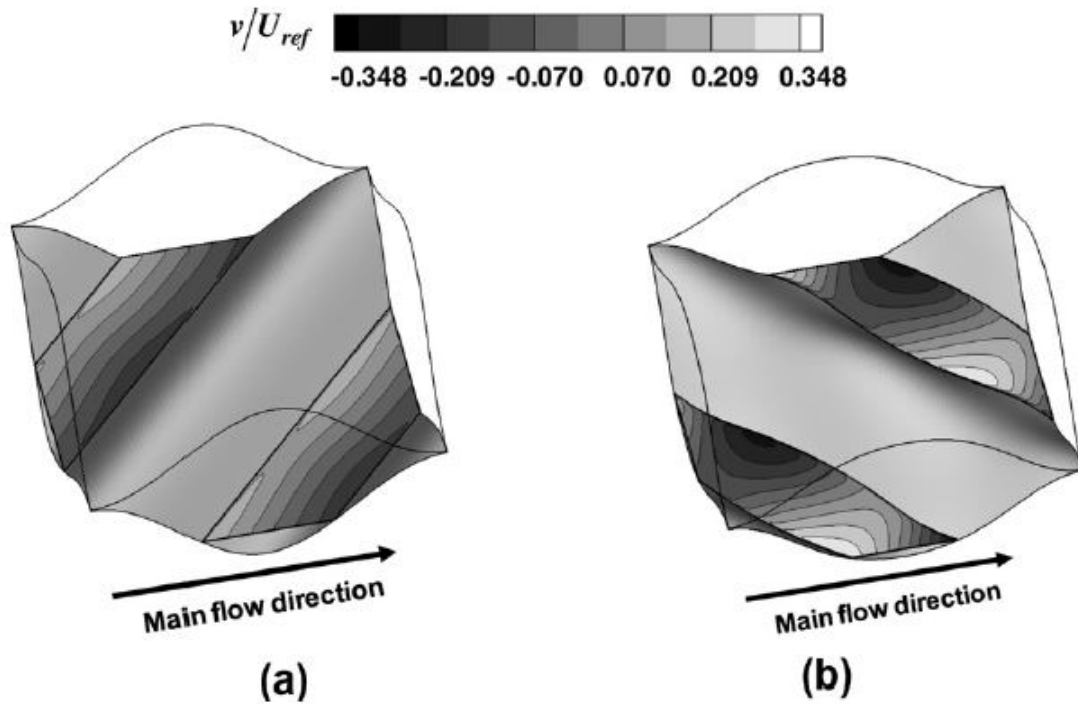


Figure 2.12: Distributions of the normal velocity component in the trough of lower plate; (a) sinusoidal model and (b) HC# 01.

Eventually, Fig. 2.13 (b) shows the schematic of boundary layer profiles around the corrugation peak of the bottom wall for the same case. The upstream flow is accelerated along the concave shape of the corrugation as moving to the corrugation peak. A typical boundary layer profile in the favorable pressure gradient is shown in this region. The flow then gradually loses its momentum due to the adverse pressure gradient located in the downstream of the corrugation peak and as a result separates.

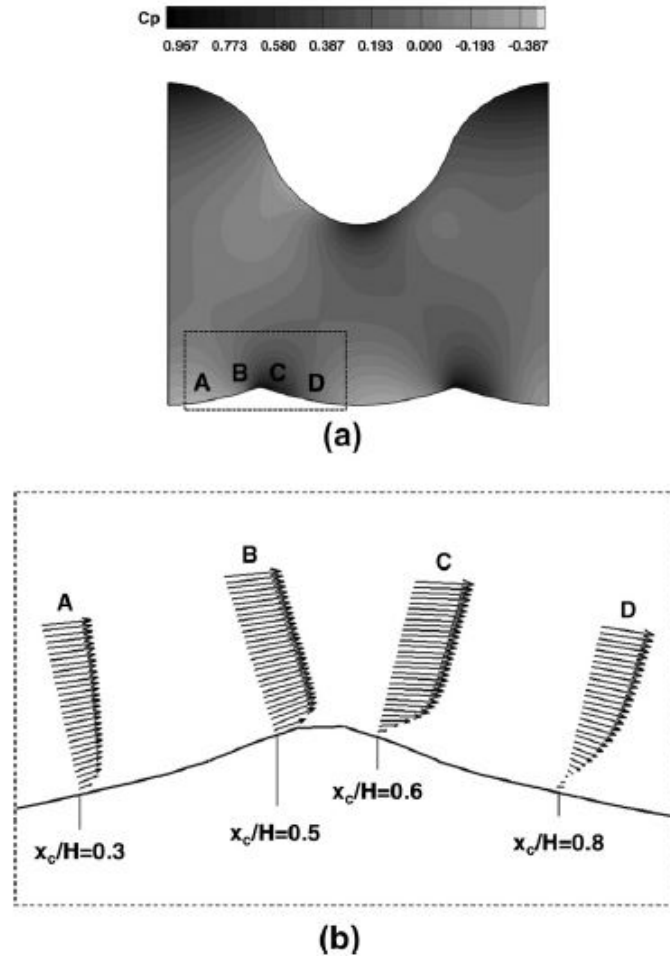


Figure 2.13: Distribution of the local pressure coefficient for the HC# 03 with $P/H = 2.2$ and (b) boundary layer profiles near the bottom wall for the same case.

The conclusion is, when increasing the ratio of pitch of corrugation to the corrugation height, the corrugation becomes flatter. The flatter corrugation results in more uniform local heat transfer coefficient distribution, as shown in Fig. 2.14 .

The PHE thermal performance is deteriorated by the highly nonuniform heat transfer coefficient (HTC) distribution. This deterioration is reflected on a temperature gradient along the plate. Compared to the conventional sinusoidal model, a pressure drop reduction of approximately -15% was predicted for the antiphase and full wave rectified secondary corrugation models (HC# 01 and HC# 03) with $P/H = 2.2$ with small changes to the predicted heat transfer capacity. The pressure drop

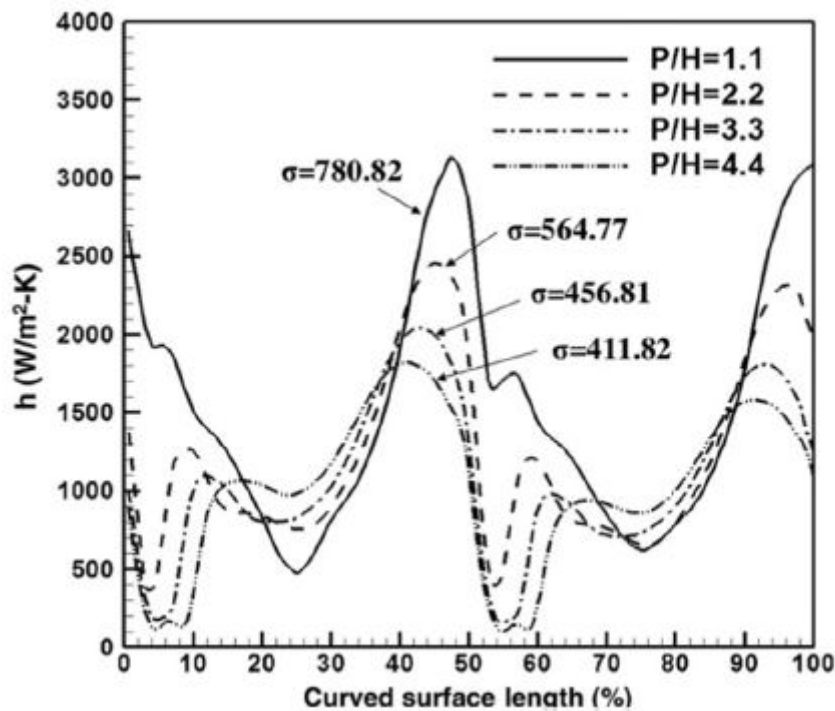


Figure 2.14: Local HTC distributions and standard deviations for four different P/H cases.

of the inphase secondary corrugation (HC# 02) was predicted to increase by approximately +38%, and heat transfer capacity was enhanced by approximately +7%. The volume goodness factor for the anti-phase and full wave rectified secondary corrugations were slightly augmented compared to the sinusoidal corrugation, however, the area goodness factors were substantially augmented with the antiphase and full wave rectified secondary corrugations showing approximately +16% and +14%, respectively. However, both the volume and area goodness factors are reduced for the in-phase secondary corrugation. The variation of the entropy generation along the trough is closely related to the local boundary layer profile. The energy dissipation is largely produced in regions of strong flow acceleration and recirculation. The entropy generation is a good indicator of the local pressure loss mechanism on the various heat transfer surfaces. The anti-phase secondary corrugation (HC# 01) was shown to produced less energy dissipation along the flow, compared to the result of the sinusoidal profile.

2.4 A brief review of trabecular and lattice struct. for HE design

The following section is udeful to discover the new additive manufacturing solutions in heat exchanger's field. In fact several tests have as object the evaluation of innovative core design performance from interesting point of view: heat transfer effect, pressure losses, structural resistance, surface quality.

Starting by a brief presentation about the lattice structures set as fundamental cell for growing up in the volume the structure itself. Recent advances in additive manufacturing facilitated the fabrication of parts with great geometrical complexity and relatively small size, and allowed for the fabrication of topologies that could not have been achieved using traditional fabrication techniques. Let explore the topology-property relationship of several classes of periodic cellular materials; the first class is strut-based structures, while the second and third classes are derived from the mathematically created triply periodic minimal surfaces, namely 2.15 ; the skeletal-TPMS and sheet-TPMS cellular structures. Powder bed fusion technology was employed to fabricate the cellular structures of various relative densities out of Maraging steel [17].

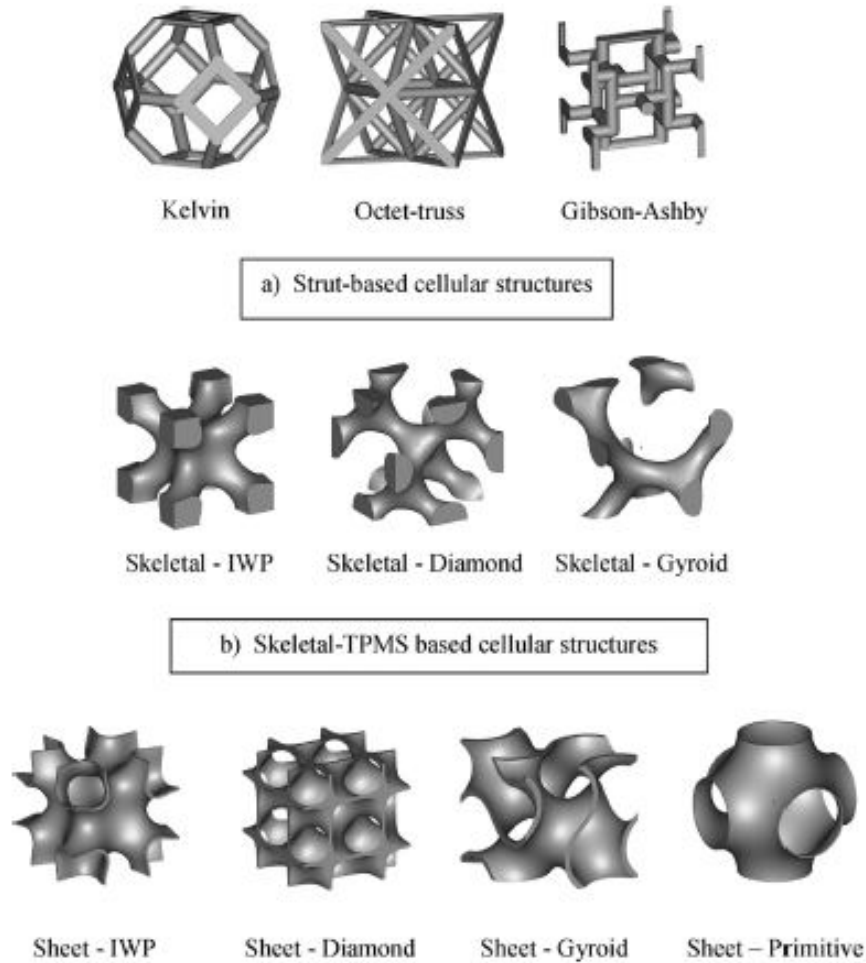


Figure 2.15: Unit cell of the different cellular topologies. a) Strut-based cellular structures, b) Skeletal-TPMS based cellular structures and c) sheet-TPMS based cellular structures.

Cellular metals offer unique functional characteristics including high stiffness to weight ratio, heat dissipation and heat transfer control, and enhanced mechanical energy absorption among others. The mechanical properties of cellular metals are a function of the relative density (defined as the density of the structure relative to the density of the base material), the solid constituent, and the unit cell architecture 2.16.

Relative density plays an important role in determining the cross-flow interactions with trabecular matrix: higher the density, higher will be the blockage effect

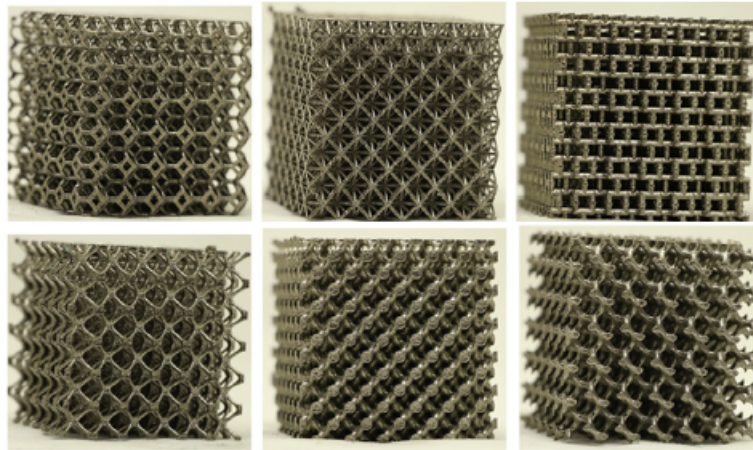


Figure 2.16: 3D printed cellular structured samples with different topologies fabricated using powder bed fusion and made of Maraging steel.

too, due to an augmented wetted area. The most important conclusion is that, while the surface area is fundamental for convection, pressure drop plays a critical and vital role in determining the performance of the HE 2.17 .

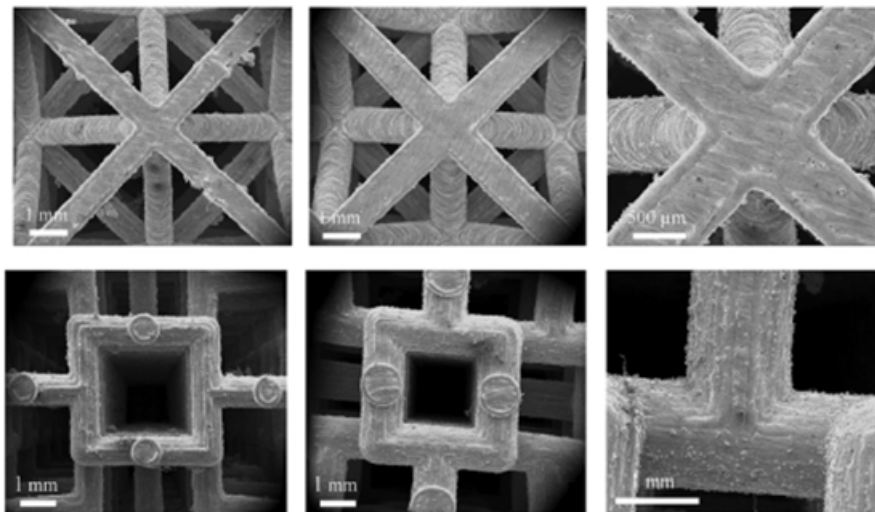


Figure 2.17: SEM images showing the powder sticking on the printed structure.

In the study presented by M. Wong, I. Owena, C.J. Sutcliffe, A. Purithermal, is investigated fluid flow characteristics of five heat sinks that have been fabricated by a rapid manufacturing technique known as Selective Laser Melting. The five heat

sinks consist of two conventional designs, the cylindrical pin and rectangular fin array, for comparison purposes. Although the lattice arrangement made use of the fabrication process, its ability to manufacture heat sinks with high surface area to volume ratios, its performance was limited by the lack of interaction between the cooling air and structure. In terms of both heat transfer performance and pressure drop, the staggered elliptical array, which cannot be manufactured by conventional techniques, outperformed the other heat sinks.

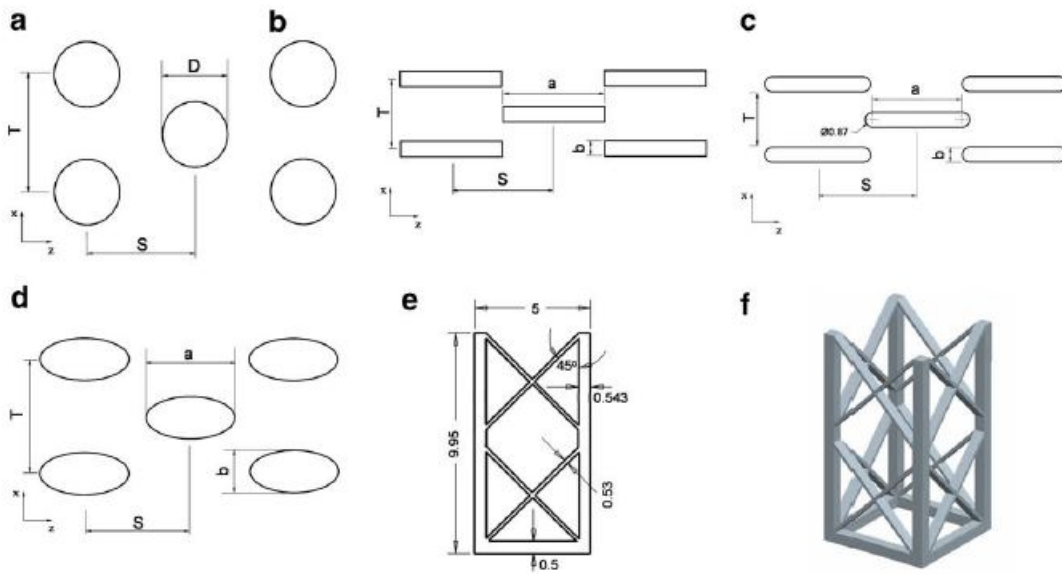


Figure 2.18: Heat sink dimensions at pin base for (a) Pin fin 6061, (b) Rectangle, (c) Rect RND, (d) Ellipse, (e) Lattice and (f) Isometric view of one Lattice cell.

This investigation compares the performance of geometrically dissimilar shapes which makes it difficult to use dimensionless groups to compare the characteristics of the different geometries.

A lattice-structure heat sink demonstrated that increasing the heat transfer surface area alone does not necessarily improve overall heat transfer performance; The air flow through an offset strip array was improved by adding rounded ends to the fins. This was simple to implement using the SLM process but offered a noticeable reduction in pressure loss across the offset strip fins, without incurring a reduction in heat transfer performance. An extension of the offset strip was an array of elliptical fins which offered the highest heat transfer rate per unit pressure drop

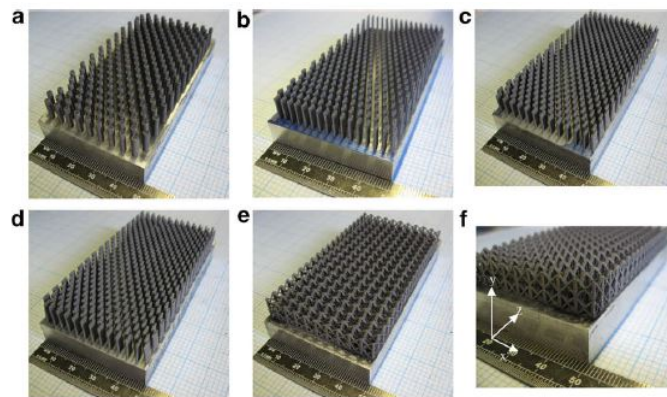


Figure 2.19: SLM fabricated heat sinks, base dimensions 50 mm x 100 mm, flow in the z direction. (a) Pin fin 6061, (b) Rectangle, (c) Rect RND, (d) Ellipse, (e) Lattice and (f) close up of Lattice.

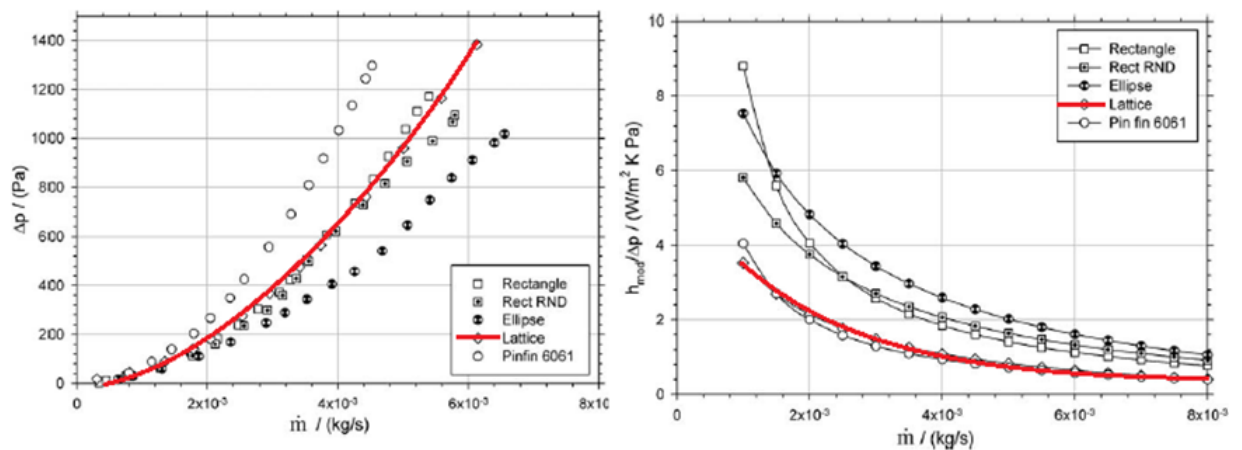


Figure 2.20: Pressure drop across heat sinks. SLM heat sink efficiency index.

compared to the other extended surfaces tested. Both Pin fin 6061 and Lattice perform poorly compared with the other extended surfaces, but for different reasons. Whereas the fin arrangement is capable of reasonable heat transfer, it also suffers from large pressure losses; the lattice has poor heat transfer performance but offers little resistance to the the air flow.

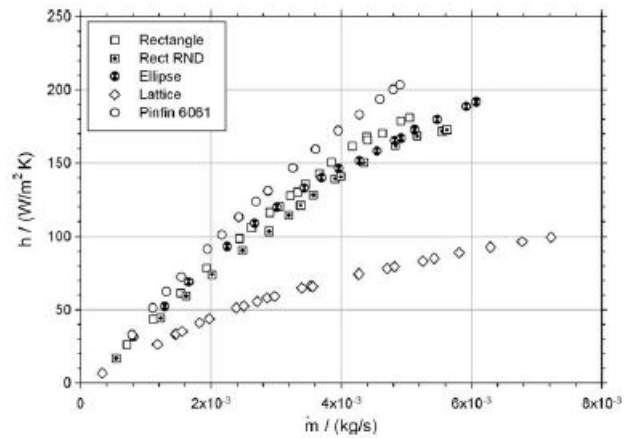


Figure 2.21: Heat transfer coefficient based on heat transfer surface area.

For the circular cross section pin array, the array orientation with respect to the mean flow direction has a small but possibly significant effect on both heat transfer and pressure loss. The channel with drop-shaped pin fins has better heat transfer behaviours than that with circular ones in the tested Reynolds range.

Chapter 3

Design for AM: value chain to develop an innovative prototype

In this chapter is resented the innovative shape of the inner core surface of the heat exchanger. By taking into account all the statements from the chapter 2 about new shape design and pin fins evaluations, it is proposed the total design and performance forecast in comparison with the current heat exchanger. Firstly, a brief but useful examination of the heat transfer mechanism is proposed, then the CAD model by Solidworks is showed. In the following pages, analytical subject's approach is followed to produce a robust and reliable model.

Value chain (5.1) is a developing method that brings to design and optimize a new proptotype, and in this case, a new heat exchanger core. The approach as a value chain [20] is needed to satisfy all the aspects of design process, like sizing, performance and building up. We can resume this method as the following flow chart suggests:

The new approach is useful to deliver:

- Maximum performance
- Minimum volume and weight
- Minimum costs
- Quality assurance

In heat exchanger development, the application consists of:

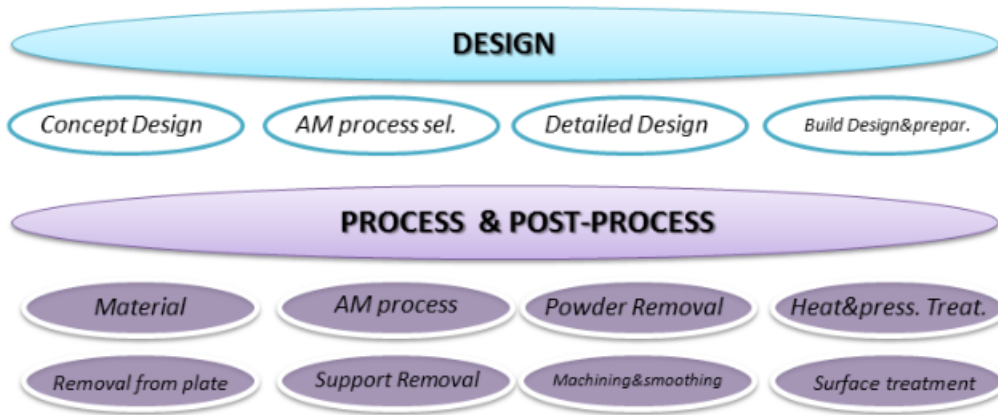


Figure 3.1: value chain approach.

- Heat Exchanger 1D sizing and performance prediction by LMTD, NTU methods;
- Heat transfer surface selection or a multi-criteria optimization;
- Correlations with test achieved.

3.1 Novel heat exchanger (HX) core: CAD design

To make sure that an effective performance enhancement will be realized, it is necessary to overcome the traditional and conventional design about heat exchanger with all the issues linked to manufacturing process and pressure drops. As the chapter 2 describes, the main aim of the thesis is to bring a novel surface which allows to enhance heat transfer coefficient, in particular convective one, but also to reduce pressure jumps strongly. It is clear that an unconventional material produces a considerable reduction of weight of the component and this is absolutely the goal of the new design: weight reduction of about 50% respect to the actual 1500g. Therefore the choice is to reshape all the inner plate as exchange surface based on considerations about new surface shapes proposed by researches earlier exposed [15]. Unlike traditional manufacturing, the complexity and the closed inner

cavities, require additive manufacturing (AM) that tears down the limit of current traditional manufacturing. So it is proposed a design for manufacturing, starting by CAD model. CAD design can be expressed as the ability to make complex shapes and sizes that were difficult to make using conventional manufacturing techniques. AM seems straightforward if a right design process is followed.

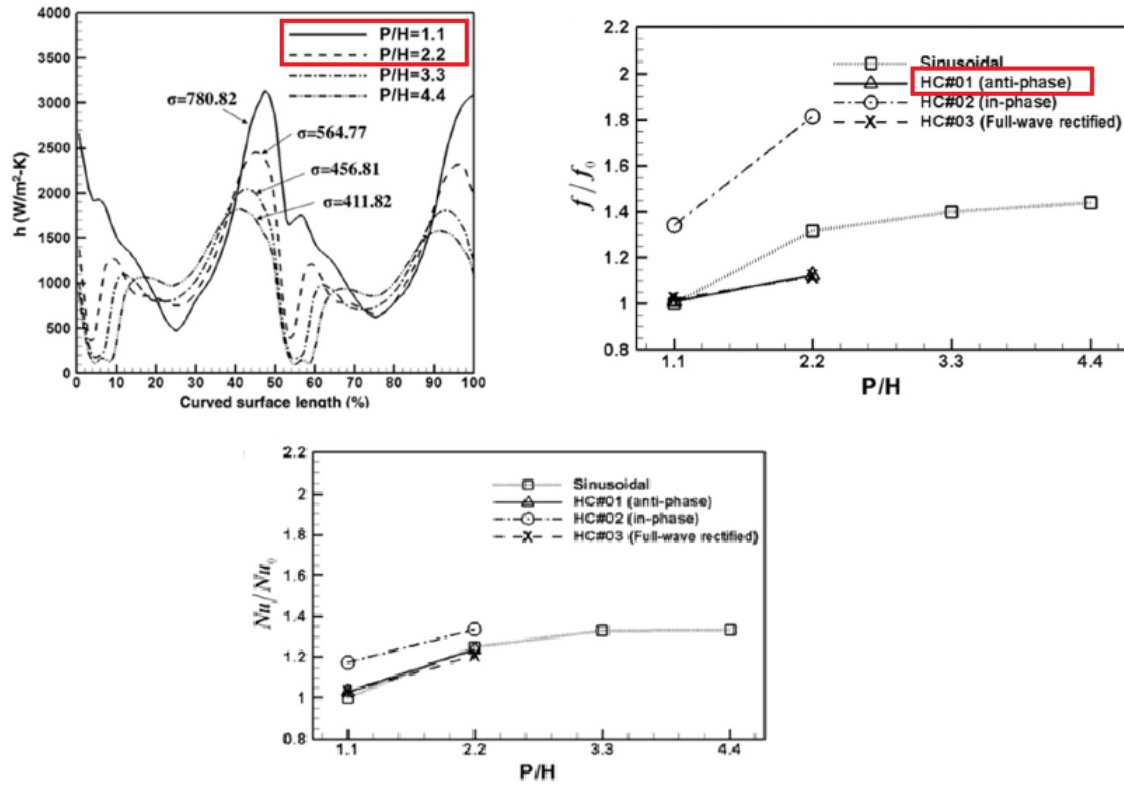


Figure 3.2: Recall of the performance of an anti-phase sinusoidal corrugated plate.

For instance, an antiphase secondary corrugation is selected to enhance heat transfer coefficients. This surface is characterized by a sinusoidal geometry along x axis but also sinusoidal shape along y axis too. However, these are anti-phase wave which means that for maximum point correspond the absolute minimum one in the opposite direction.

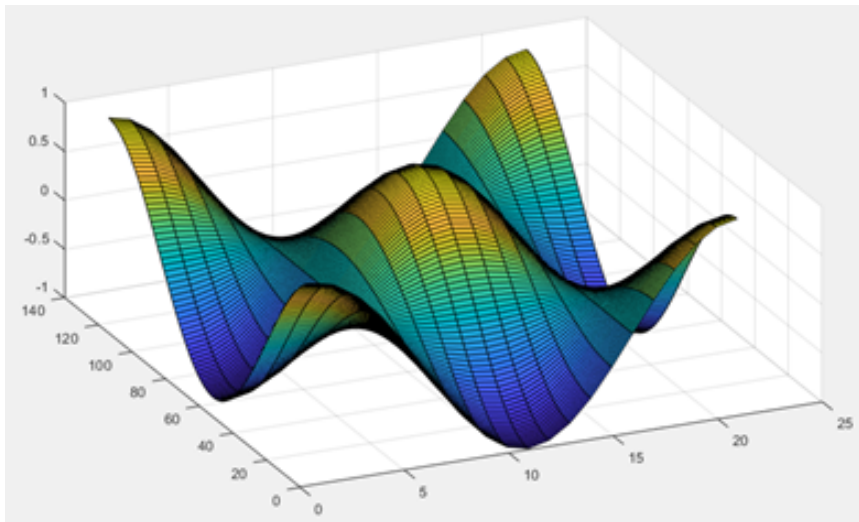
There are two parameters refer to surface configuration, they are:

It is clear that a P/H of 2.2 is recommended to increase htc. Unfortunately, it is not so practicable by building up process. It is necessary to avoid topological problems to choose a flatter plate where the pitch to height ratio of the wave

Table 3.1: Geometry characterization of the wave-surface.

Parameter	Symbol	Values
Pitch	P	6mm
Height	H	2mm
P/H	-	3

surface in slightly higher. Analytical representation of the surface is generated by MATLAB[®]script before cad design. The unit cell showed below in the fundamental block that morph the inner plate's core 3.3 .

Figure 3.3: MATLAB[®]unit cell generation.

The next step is to design unit cell into cad environment as Solidworks to model the 3D shape. This is showed in the following figure 3.4 .

Specification of the unit cell:

Table 3.2: Unit cell Features.

Property	Values
Mass	0.05g
Surface Top Area	44.22mm ²
Volume	19.29mm ³
Thickness	0.4mm

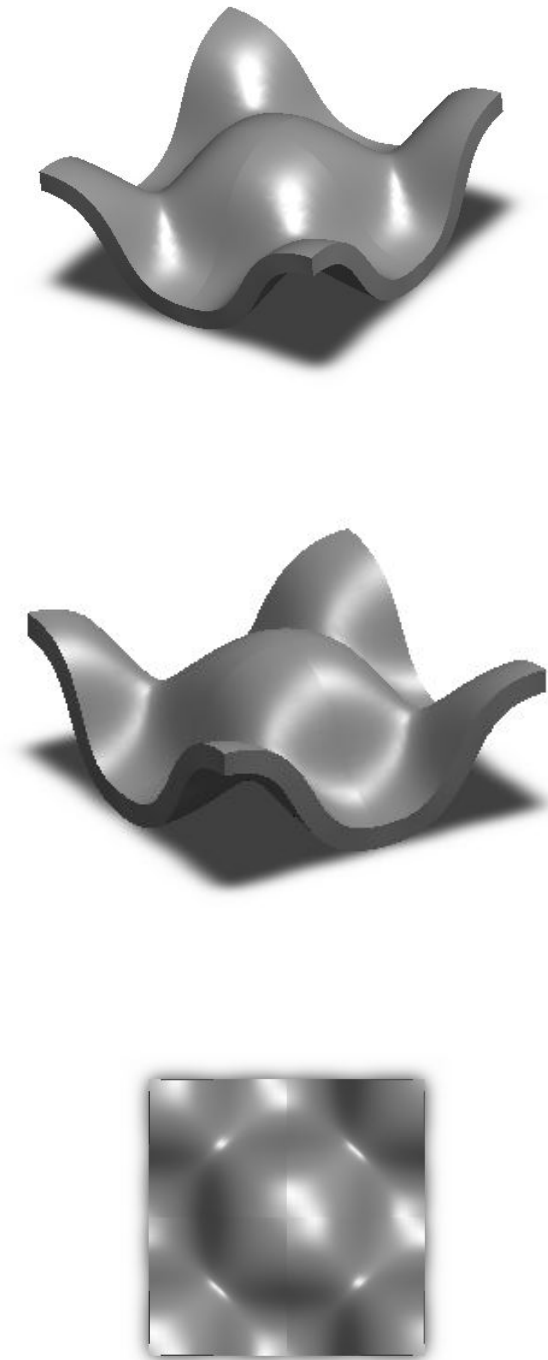


Figure 3.4: Solidworks unit cell.

3.1.1 Material for AM

AlSi10Mg is a typical casting alloy with good casting properties and is typically used for cast parts with thin walls and complex geometry. It offers good strength, hardness and dynamic properties and is therefore also used for parts subject to high loads [3]. Parts in Aluminium AlSi10Mg are ideal for applications which require a combination of good thermal properties and low weight. They can be machined, spark-eroded, welded, micro shot-peened, polished and coated if required. Conventionally cast components in this type of aluminium alloy are often heat treated to improve the mechanical properties. In order to make a truthful evaluation of the component features, it is necessary to create a new material in Solidworks tool named AlSi10Mg, to which are referred all the material property like the following ones:

Technical Data	Test Method		
Typical achievable part accuracy	-----	± 100 µm	
Smallest wall thickness [1]	-----	approx. 0.3 – 0.4 mm	
Surface roughness, as built, cleaned	-----	Ra 6 - 10 µm, Rz 30 - 40 µm	
Surface roughness, after micro shot-peening	-----	Ra 7 - 10 µm, Rz 50 - 60 µm	
Mechanical properties of parts	Test Method	As Built	Heat Treated [5]
Tensile strength [2] in horizontal direction (XY)	ISO 6892-1:2009(B) Annex D	460 ± 20 MPa 66.7 ± 2.9 ksi	345 ± 10 MPa 50.0 ± 1.5 ksi
Tensile strength [2] in vertical direction (Z)	ISO 6892-1:2009(B) Annex D	460 ± 20 MPa 66.7 ± 2.9 ksi	350 ± 10 MPa 50.8 ± 1.5 ksi
Yield strength (Rp 0.2 %) [2] in horizontal direction (XY)	ISO 6892-1:2009(B) Annex D	270 ± 10 MPa 39.2 ± 1.5 ksi	230 ± 15 MPa 33.4 ± 2.2 ksi
Yield strength (Rp 0.2 %) [2] in vertical direction (Z)	ISO 6892-1:2009(B) Annex D	240 ± 10 MPa 34.8 ± 1.5 ksi	230 ± 15 MPa 33.4 ± 2.2 ksi
Modulus of elasticity in horizontal direction (XY)	-----	75 ± 10 GPa 10.9 ± 0.7 Msi	70 ± 10 GPa 10.2 ± 0.7 Msi
Modulus of elasticity in vertical direction (Z)	-----	70 ± 10 GPa 10.2 ± 0.7 Msi	60 ± 10 GPa 8.7 ± 0.7 Msi
Elongation at break [2] in horizontal direction (XY)	ISO 6892-1:2009(B) Annex D	(9 ± 2) %	12 ± 2 %
Elongation at break [2] in vertical direction (Z)	ISO 6892-1:2009(B) Annex D	(6 ± 2) %	11 ± 2 %
Hardness [3]	DIN EN ISO 6506-1	approx. 119 ± 5 HBW	-----
Fatigue strength [4] in vertical direction (Z)	-----	approx. 97 ± 7 MPa approx. 14.1 ± 1.0 ksi	-----
Thermal properties of parts	Test Method	As Built	Heat Treated [5]
Thermal conductivity at 20 °C in horizontal direction (XY)	-----	approx. 103 ± 5 W/m °C	approx. 173 ± 10 W/m °C
Thermal conductivity at 20 °C in vertical direction (Z)	-----	approx. 119 ± 5 W/m °C	approx. 173 ± 10 W/m °C
Specific heat capacity in horizontal direction (XY)	-----	approx. 920 ± 50 J/kg °C	approx. 890 ± 50 J/kg °C
Specific heat capacity in vertical direction (Z)	-----	approx. 910 ± 50 J/kg °C	approx. 890 ± 50 J/kg °C

Figure 3.5: AlSi10Mg spec. courtesy of ZARE prototipi.

3.1.2 Single plate design

After the design of the unit cell, the repetition along two axis of the inner plate is made. This step produce the filling of the internal heat exchange surface, at fixed dimensions of the inner hole. In particular, boundary's cell row is quite complex to join up. in fact a good quality cad model needs to have loft surfaces at the boundary by creating geometric continuity of the plate.

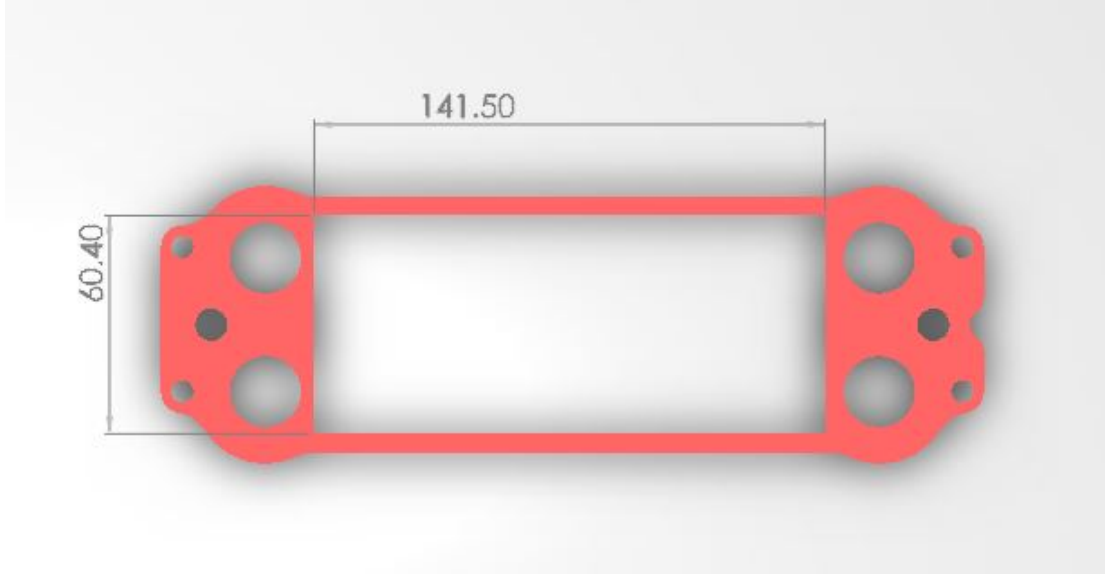


Figure 3.6: Filling of the inner surface.

$$N_{uc,x} = \frac{L_x}{P_{uc}} = \frac{141.50}{6} = 23.6 \quad (3.1)$$

$$N_{uc,y} = \frac{L_y}{P_{uc}} = \frac{60.40}{6} = 10.06 \quad (3.2)$$

Table 3.3: Overall corrugated plate dimensions.

N_x	N_y	Round off N_x	Round off N_y	Total cells
23.6	10.06	23	10	230

Table 3.4: Corrugated plate features: one plate spec.

Prop.	Values
Surf. Area	10170.6mm ²
Mass	11.5g
Volume	44.36mm ³
Thickness	0.4mm

Comparing the new design configuration to the current plate surface, provides an augmented wetted area use to the heat exchange. In terms of Enlargment Factor, it is of about 1.8 larger then a flat plate 3.7 .

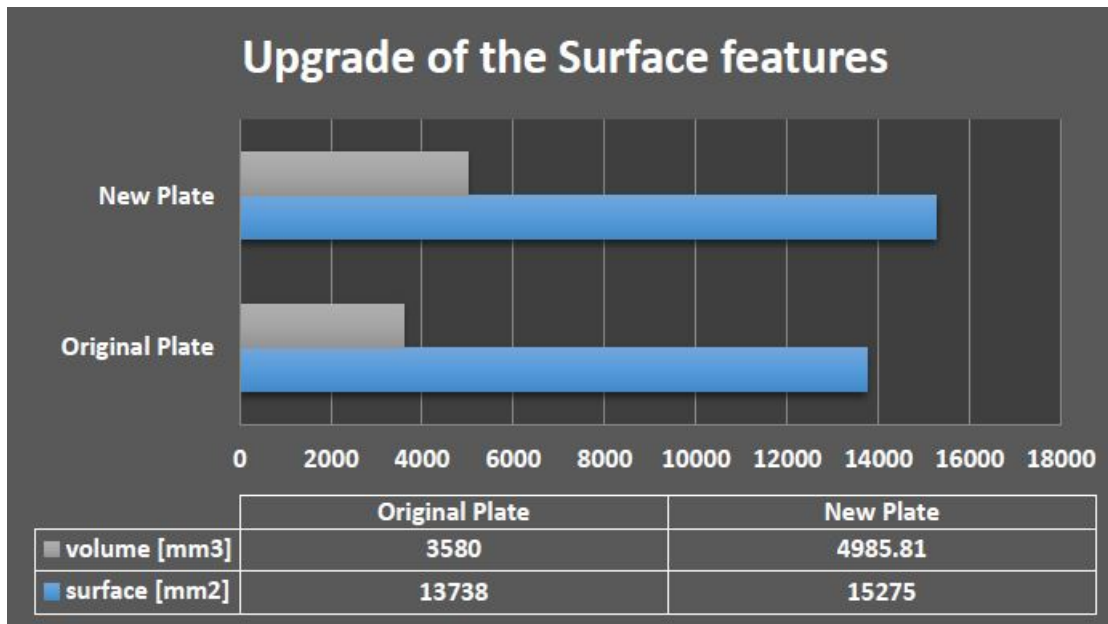


Figure 3.7: Comparison between current and novel surface.

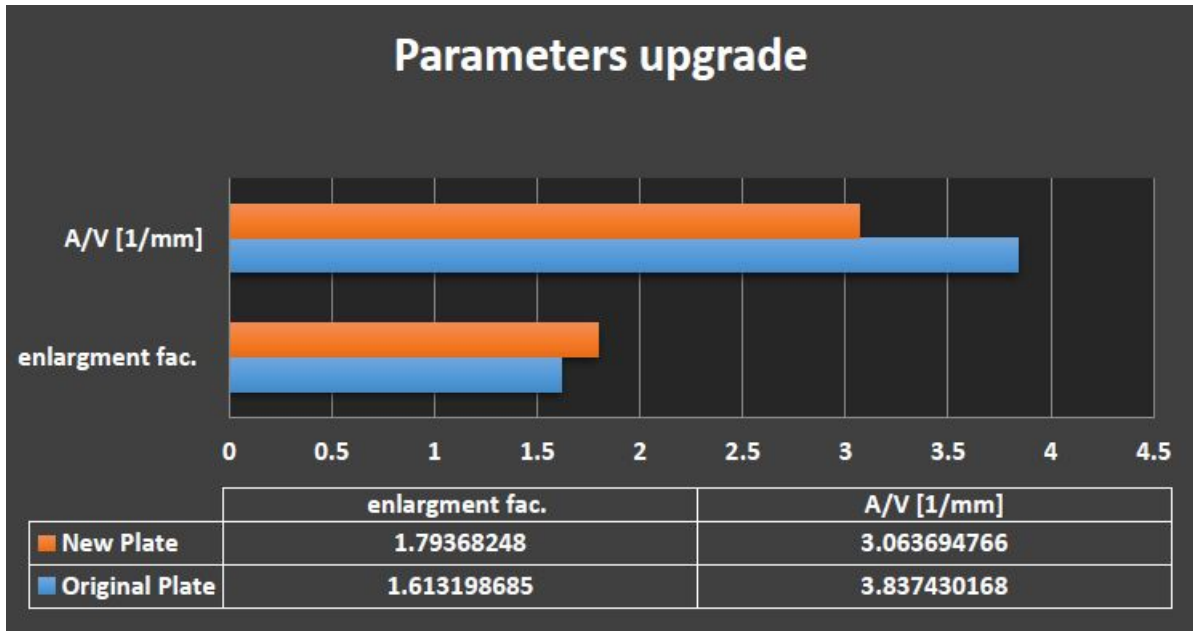


Figure 3.8: Enlargment factor and compactness factor.

3.1.3 Core layout

The layout of the core is different respect to the current one, infact it has been opted for a configuration with 6 water channels against the 8 originally, and 5 channels for the oil circuit. In order to reduce the overall weight of the exchanger, the thickness of the plate is fixed at 0.5mm and the separation spacement or pitch is of 4mm water-water and 3mm for oil-oil. Moreover, this configuration make quite smaller the pressure drop of the water circuit, beacuse of the distanse of the ducts rises.

In the figure above 3.9, can be observed the presence of two grey elements at the top and bottom of core. These are two flanges. The heat exchanger is located in a box embedded in the engine and there is the interface between flage and carter which can be think as a manifold. The inner flange presented four holes, each couple different from the other one, which act as inlet and outlet for water and oil, respectively. Four o’ring are inserted to ensure the perfect seal in the manifolds. Additionally, mechanic loads as vibration and thermal stress make thickness of the falnge larger than other parts. For this reason, the inner flange can not become lighter.

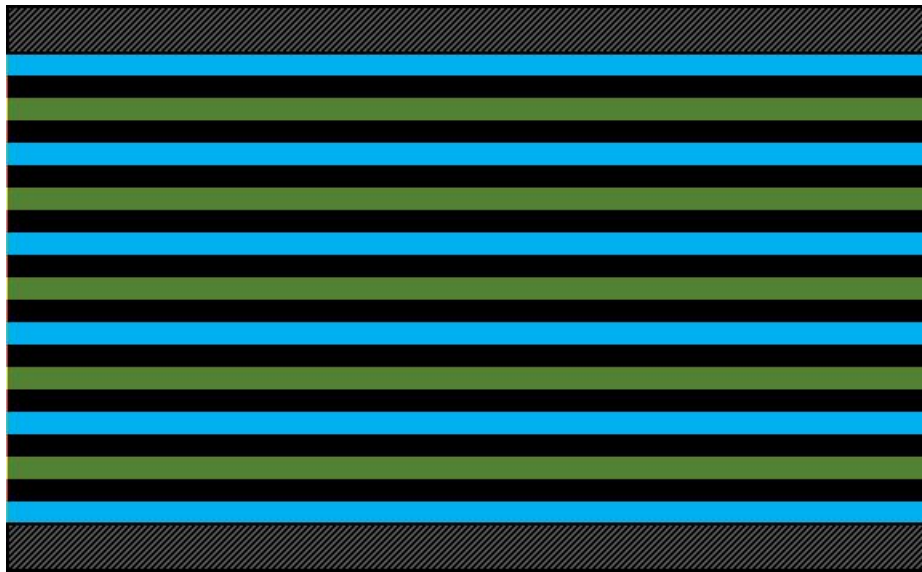


Figure 3.9: Core layout, inner configuration: blue-water channels; green-oil channels; black-separation surface to prevent contact between fluids.

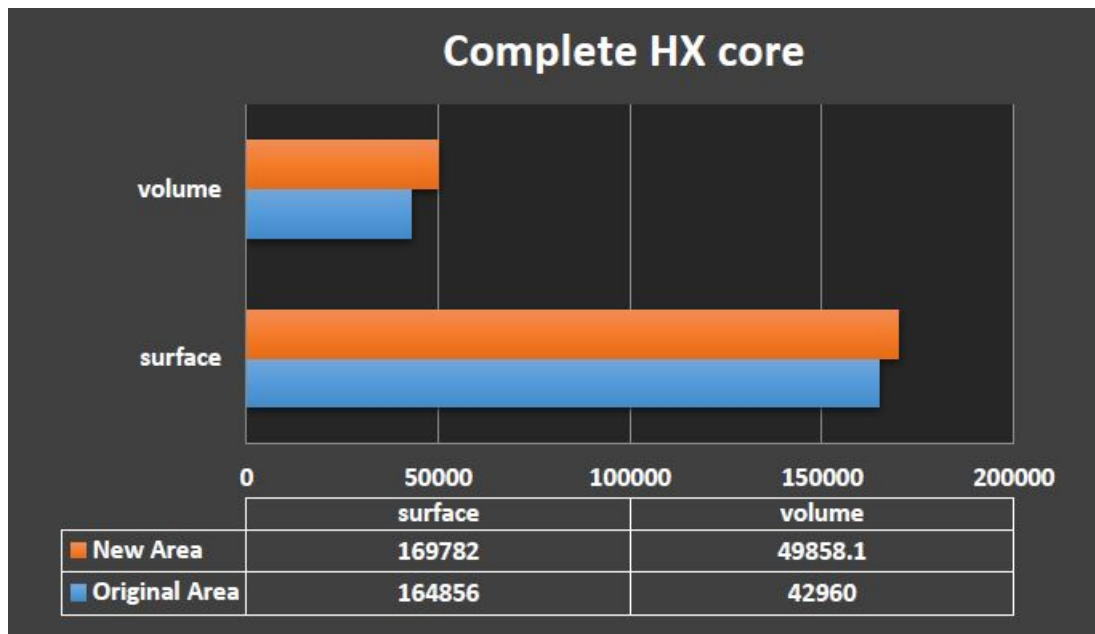


Figure 3.10: Complete Core upgrade.

3.1.4 Weight valuation

In order to further reduce the overall weight of the HX, reshaping of all the parts of the HX assembly is required. First of all, a brief recall of the single part that create the CAD assembly:

- Two flanges, top and bottom to cover che HX core;
- Separation plate where corrugated new designed surfacem is placed;
- Glasket channel’s separator, with two different spacing like above described;

In the following pages is presented a comparison between the original parts and the new ones with the weight evaluation made by Solidworks. AlSi10Mg material is assigned 3.11 .

Table 3.5: Weight optimization for the complete HX.

File	W_i [g]	W_f [g]	ΔW [g]	% W	Number
Outer flange	83.07	74.19	8.88	10.68	1
Inner flange	157.92	113.4	44.52	28.19	1
Separator	22.95	5.93	17.02	74.16	10
Pass. 4mm	43.01	36.36	6.65	15.46	6
Pass. 3mm	43.01	27.27	15.74	36.59	5
Corr. Surface	13.34				10
Pillars	39.49	31.36	8.13	20.58	

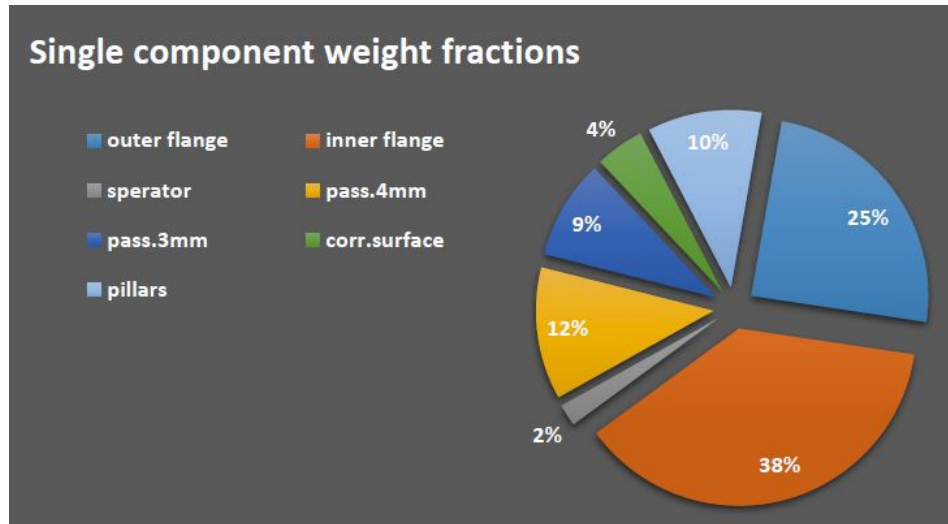


Figure 3.11: Parts weight evaluation, HX material AlSi10Mg.

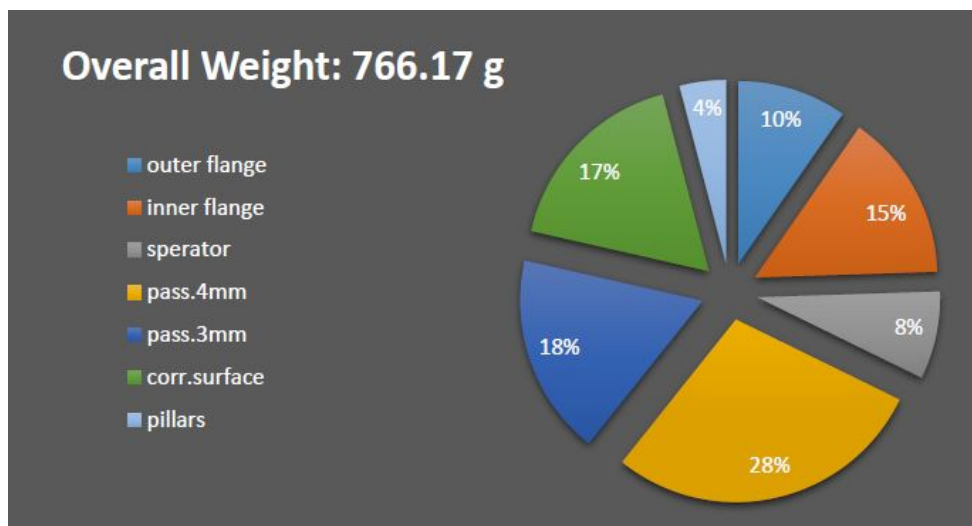
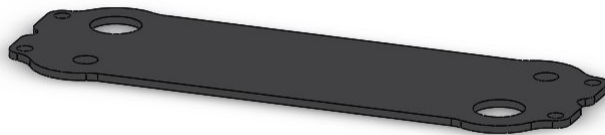
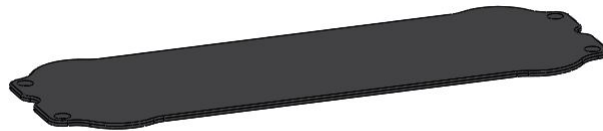


Figure 3.12: Weight evaluation, HX material AlSi10Mg.



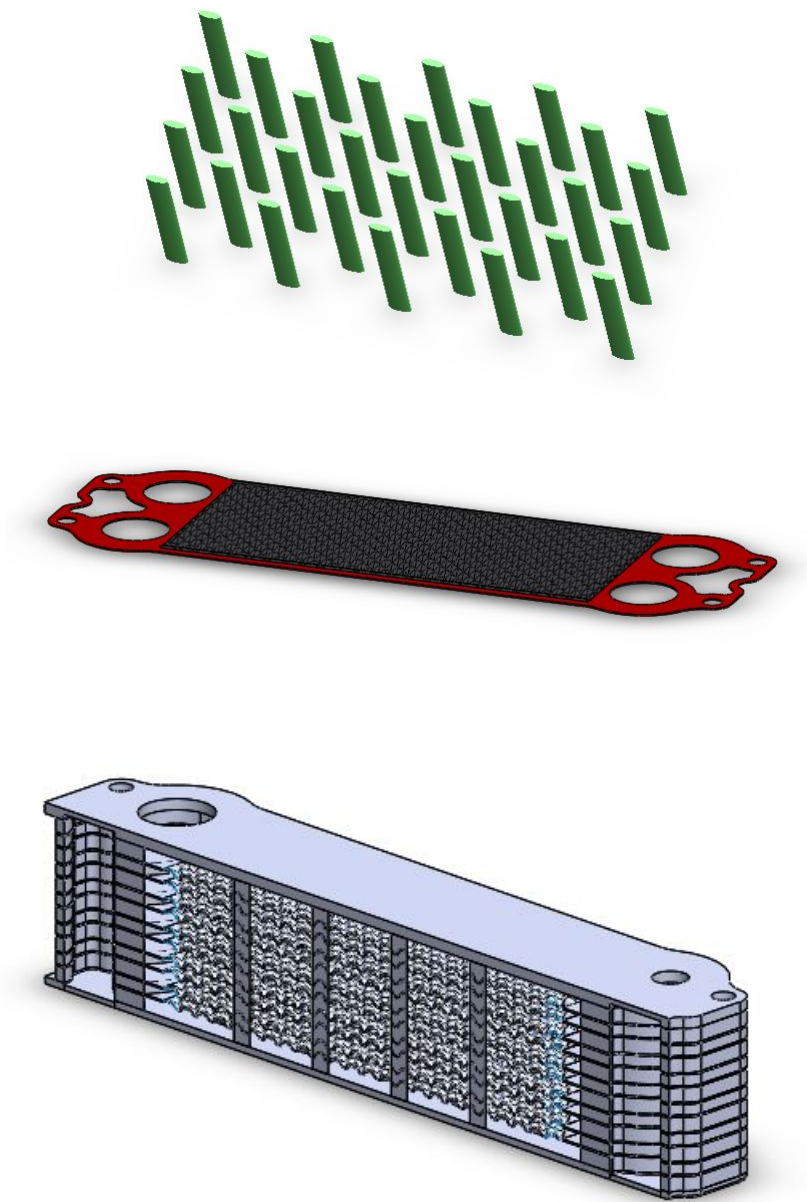


Figure 3.13: Elements of the assembly.

3.2 Metal Additive manufacturing

In order to obtain consistent weight reduction and realize complex shape in easy way, additive manufacturing is selected as suitable process to produce a monolithic element like heat exchanger is. In particular reduction in weight is well matched thanks to AlSi10Mg material powder. If we give an overview to the Metal manufacturing process, we can say that it is made of several linked steps which bring to an optimal object ready to work.

- Part Design: it is convenient to think additive. Part integration will be simpler if in design step some issues are already overcome.
- Software Build Setup: integration is performed by dedicated software. The most famous in the industrial enclosure are EOS RP Tools, EOSTATE, EOSPRINT, Materialise Magics RP.
- Physical Setup: selecting the material in particular AlSi10Mg required for high temperature application and aerospace one.
- Printing: the job is ready to be played.

The next phase is under the name "Quality Assurance" and it is articulated in four steps after printing ended.

- Build Removal: once printing finished, the plate is full of powder but the element printed lies in.
- Part Separation: part is separated from the fusion bed
- Machining: removal of all the supports
- Surface Finishing: roughness of the surface is leveled by machining the surface

Then heat treatment started.

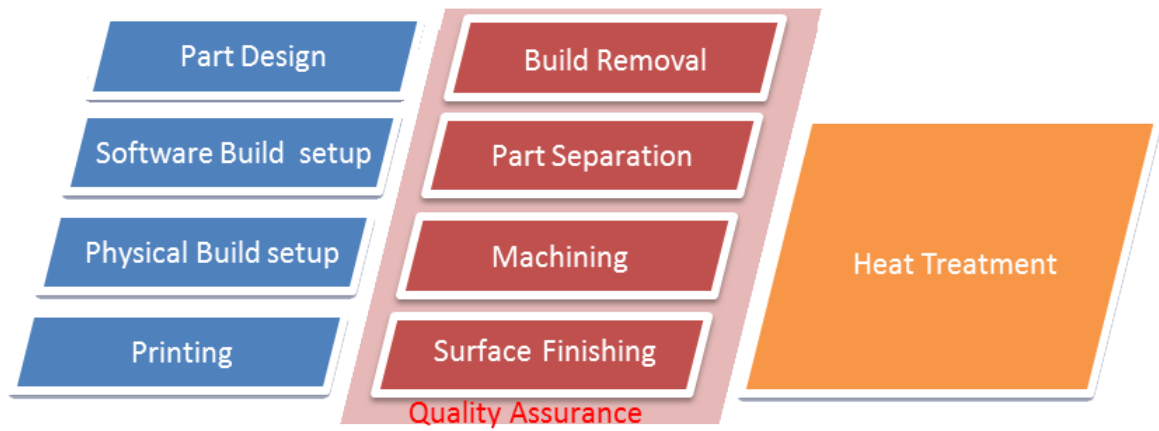


Figure 3.14: Metal 3D printing process, step by step.



Figure 3.15: EOS M290 printer.

Chapter 4

HX performance and simulation by STAR CCM+ software

This section is concerned with the characterization of conduction heat transfer and forced convection within ducts, which is a mode that pervades a wide range of systems and devices. Conduction requires the presence of an intervening medium. In the most cases the evaluation of the power exchanged throughout medium in steady conditions, is interesting to be investigated. Many can be studied by thermal resistances network approach like electrical circuits, and the main aim is to input temperatures and output power. In the following pages will be taken into account all the mechanism that occurred in the heat transfer. Heat conduction across plane walls or solid medium, convection in the inner channels, forced convection more exactly and overall heat transfer coefficient finally.

Simulations performed by STAR CCM+ cfd software are included, to validate the performance of the current heat exchanger in terms of pressure drop firstly, then the novel architecture of the core is evaluated by pressure drop and heat transfer coefficient.

4.1 Heat Transfer Mechanism: conduction and convection

The basic equation for the analysis of heat conduction is Fourier's law, which is based on experimental observations and is:

$$q_n'' = -\lambda_n \frac{\partial T}{\partial n} \quad (4.1)$$

- q_n'' in (W/m²) is the heat transfer rate in the n direction per unit area normal to the heat flow's direction;
- λ_n (W/m · K) is the thermal conductivity in the direction n;
- $\frac{\partial T}{\partial n}$ (K/m) is the temperature gradient in the direction n.

The thermal conductivity is a thermophysical property of the material, which is, in general, a function of both temperature and location; that is, $\lambda = f(T, n)$. For isotropic materials, λ is the same in all directions.

Consider a plane wall of thickness L made of material with a thermal conductivity k. The temperatures at the two faces of the wall are fixed at T_{s1} and T_{s2} with $T_{s1} > T_{s2}$. For steady conditions with no internal heat generation and constant thermal conductivity, the appropriate form of the general heat conduction equation, is:

$$q = \frac{\lambda A (T_{s1} - T_{s2})}{L} \quad (4.2)$$

An example of application of Fourier's law is the conductive heat exchange in a flat surface at fixed boundary conditions. In fact in this case, this example is suitable for our purpose. Consider a plate of thickness 3mm and length 140mm which is like the separation surface in the current compact heat exchanger. As a certain temperature is assigned to the top surface and a different one at the bottom, a temperature gradient occurs and a conductive heat diffusion starts across the medium as Fourier's law describes. Therefore, material plays important role to make final temperature's value.

The previous equation, where λ and A are presumed constant, suggests that in a way that is analogous to Ohm's law governing electrical current flow through

Table 4.1: Boundary conditions and setting for conductive heat transfer on a plate.

Surface	Lenght [unit]	Thickness.	λ [W/mK]	T_{top} [$^{\circ}C$]	T_{bot} [$^{\circ}C$]
Plate	140mm	3mm	290	90	110

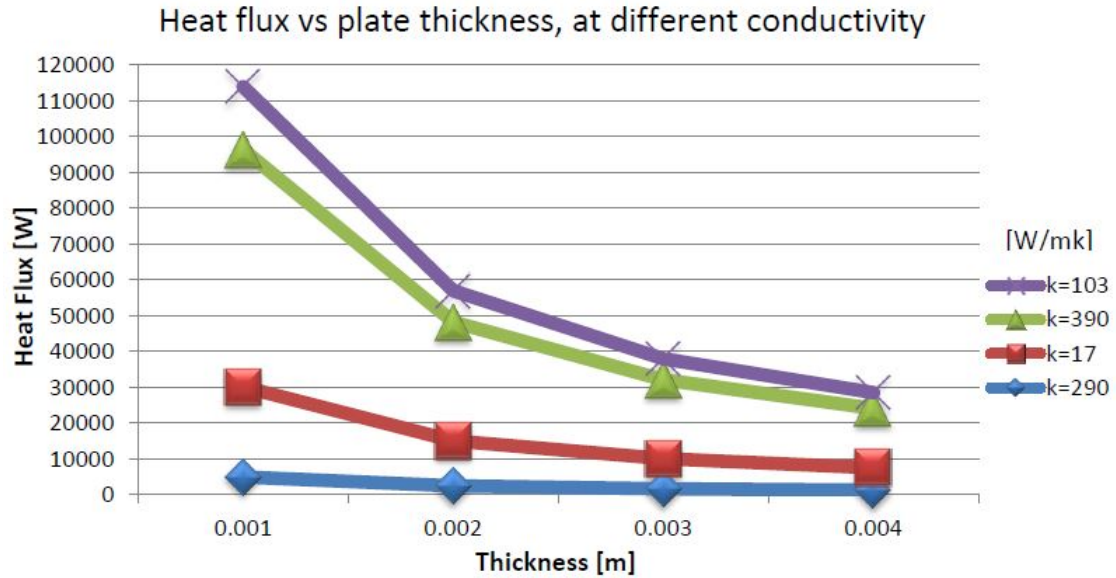


Figure 4.1: The graph shows the variation of the conductive heat flux on the plate thickness, at different material's conductivity.

a resistance, it is possible to define a conduction thermal resistance as:

$$R = \frac{T_1 - T_2}{q} = \frac{L}{\lambda A} [K/W] \quad (4.3)$$

As the graph 4.2 shows, the thermal resistance of a certain material increases as the the thickness of the plate increase too but on the other hand smaller resistance means higher heat flux through that solid medium. In fig. 4.1 is showed an increasing of the heat flux as the thickness tends to zero. Therefore we can assert that if the wall thickness is near to zero, the thermal resistance does not influence the heat transfer in conductive way.

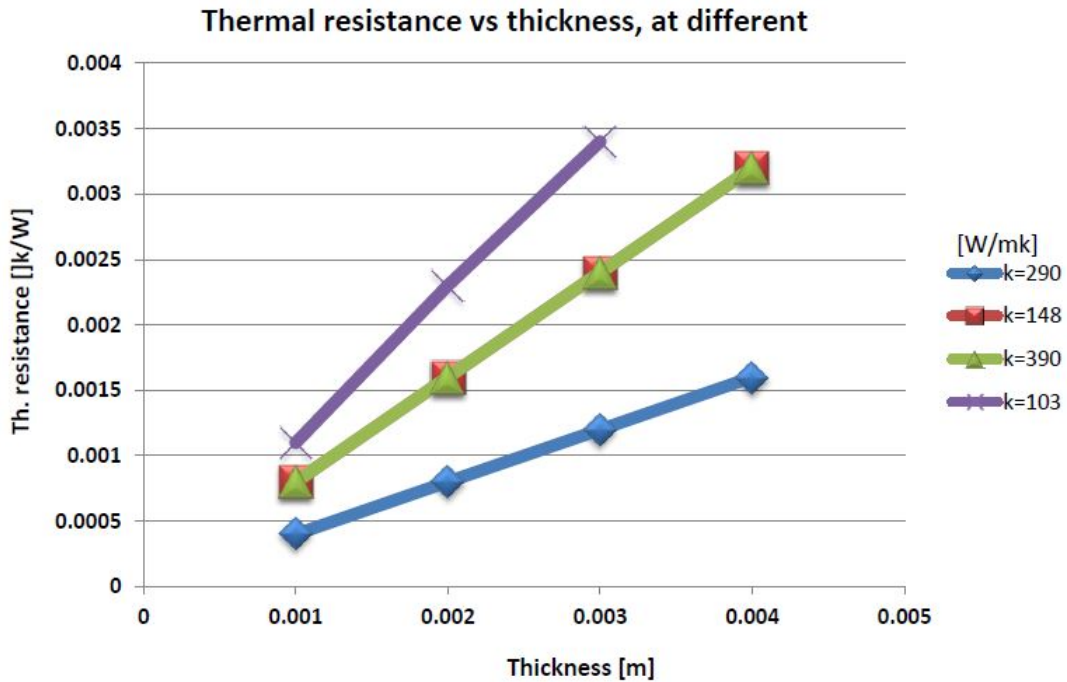


Figure 4.2: Variation of the thermal resistance on thickness of the plat.

Even if the theory of fluids is well developed, analytical solutions are calculated for simpler cases only, such as laminar flow through channel, fully developed. Then for others more complex cases it is necessary to refer to correlation and experimental solutions. The thermal flux can be laminar or turbulent, depending of the fluid. Generally, at low velocity the flow is laminar, instead at high speed it is turbulent. Most fluids are turbulent as their viscosity increases. Consider a circular cross section duct, Reynolds number is defined as:

$$Re = \frac{\rho w D}{\mu} = \frac{w D}{\nu} \quad (4.4)$$

where:

- w is the mean speed of the flow;
- D is the duct's diameter;
- μ is the dynamic viscosity [kg/m];

- ν is the cinematic viscosity [m^2/s], defined as $\nu = \mu / \rho$;

Generally, for flows in non-circular channels is preferred the use of the equivalent diameter or hydraulic diameter, calculated as the ratio between Area of the channle and perimeter, as follow:

$$D_{eq} = \frac{4A_c}{p} \quad (4.5)$$

In circular duct it is exactly the real diameter of the channel. The previous definition of Reynolds number is not quite exact because of many factors that influence the flow behaviour are not considered. Some of these are surface roughness, vibrations of the channels, unsteady motion in the duct. General, for most basical application the variation of Re defines:

- $Re < 2300$ laminar;
- $Re > 10000$ completely turbulent;
- $2300 < Re < 10000$ transition from laminar to turbulent;

However in the design approach is common to consider turbulent flow with $Re > 4000$: this is more conservative for calculation [21].

The region beyond the entrance region in which the velocity profile is fully developed and remains unchanged is called the hydrodynamically fully developed region. The velocity profile in the fully developed region is parabolic in laminar flow and somewhat flatter in turbulent flow due to eddy motion in radial direction 4.4 .

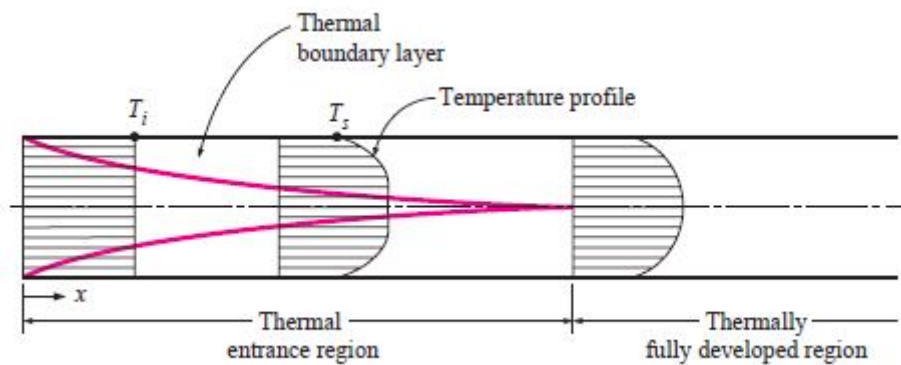


Figure 4.3: Development of the thermal boundary conditions.

Convective thermal transport from a surface to a fluid in motion can be related to the heat transfer coefficient h , the surface-to-fluid temperature difference, and the wetted surface area S in the form:

$$q = hS(T_s - T_f)[W] \quad (4.6)$$

For a particular geometry and flow regime, h may be found from available empirical correlations and/or theoretical relations. Use of eq. below makes it possible to define the convective thermal resistance as:

$$R_{cv} = \frac{1}{hS} \quad (4.7)$$

Common dimensionless quantities that are used in the correlation of heat transfer data are the Nusselt number Nu , which relates the convective heat transfer coefficient to the conduction in the fluid:

$$Nu = \frac{h}{\lambda/L} = \frac{hL}{\lambda} \quad (4.8)$$

The Prandtl number Pr , which is a fluid property parameter:

$$Pr = \frac{c_p \mu}{\lambda} = \frac{\nu}{\alpha} \quad (4.9)$$

where:

- h : convective heat transfer coefficient, $[W/m^2K]$
- L : main geometrical length of the plate;
- c_p : specific heat at pressure constant, $[kJ/kg K]$
- α : thermal diffusivity, $[m^2/s]$

4.1.1 Reynolds number for water and oil side

Initially, consider the actual heat exchanger's turbulator. In many compact HX the inner turbulator can be considered as an offset strip fin whose geometrical features are described in tab5.3 , below:

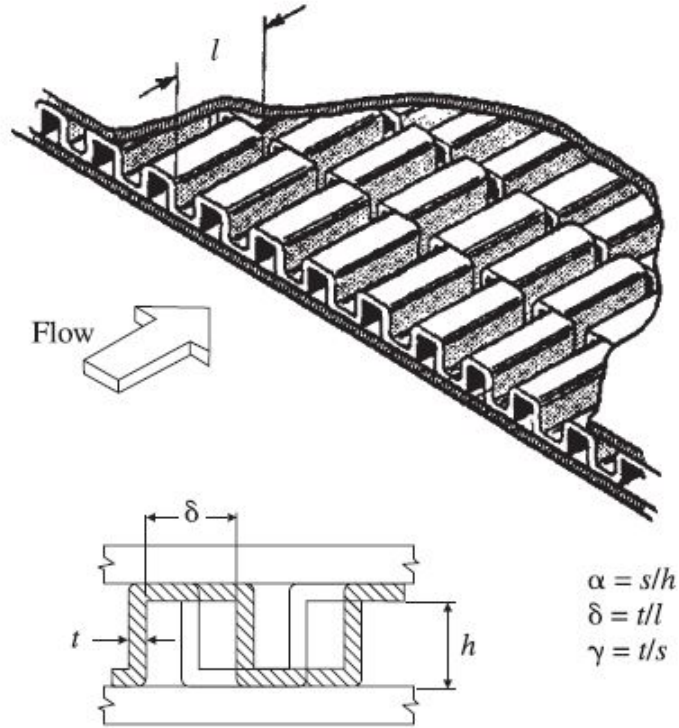


Figure 4.4: Geometry of the rectangular offset strip plate fins.

Table 4.2: Geometrical features of the actual HX inner turbolator, measured by Solidworks model.

t[mm]	l[mm]	h[mm]	s[mm]
0.20	4.5	2.8	3.1

By introducing dimensionless geometrical parameters is convenient to overcome the geometry. In this circumstance α , δ , γ are calculated and then the hydraulic diameter:

Hydraulic diameter is:

$$D_h = \frac{4A}{P} = \frac{4shl}{(2(sl + hl + th) + ts)} = 0.0024m \quad (4.10)$$

Reynolds number is calculated starting by the mass flow rate for the water channel, then for oil's one.

Table 4.3: Dimensionless parameters of the geometry.

α	δ	γ
1.1071	0.0444	0.0645

Table 4.4: Water channel: Reynolds number, water properties at 360K.

ρ [kg/m ³]	μ [kg/ms]	d [m]	A[m ²]	w_m [m/s]	\dot{m} [kg/s]
958	$0.320 \cdot 10^{-3}$	0.0024	$9.8 \cdot 10^{-6}$	0.8791	0.1515

$$Re_w = \frac{\rho w_m D_h}{\mu} = 6238 \quad (4.11)$$

Table 4.5: 10W-50 SE oil channel: Reynolds number at 373K.

ρ [kg/m ³]	μ [kg/m]	d [m]	A[m ²]	w_m [m/s]	\dot{m} [kg/s]
840	$17.1 \cdot 10^{-3}$	0.0024	$9.8 \cdot 10^{-6}$	0.2817	0.0719

$$Re_{oil} = \frac{\rho w_m D_h}{\mu} = 66 \quad (4.12)$$

For the two circuits, Re is lower than 2300 and the inner flow regime is laminar.

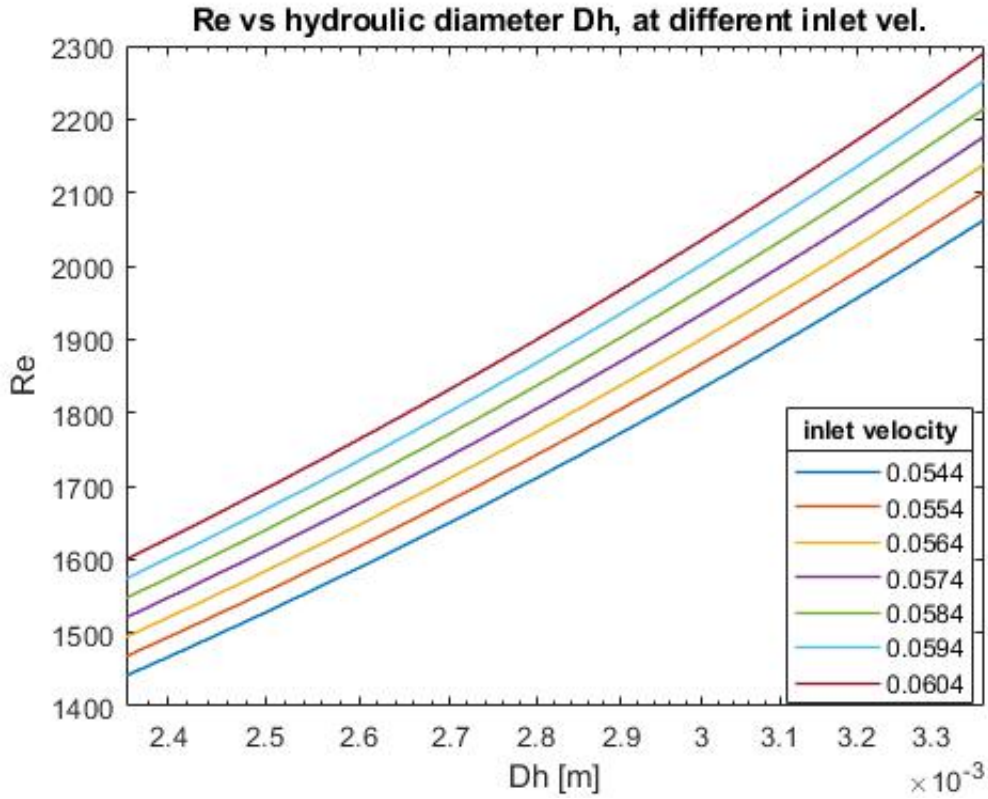


Figure 4.5: Reynolds number and plate diameter.

The figure 4.6 shows that Re increases if the inlet velocity of the flows augments. In particular this means that a more energetic fluid as an accelerated one, is better for Re which represents the ratio between inertia and viscous force. High Reynolds number means that the flow is more turbulent and the viscosity of fluid does not affect the motion of the fluid too. At the opposite side, keeping constant the velocity inlet, it is clear that to have higher Re we have to augment the hydraulic diameter which means an increase of the mass flow rate section.

4.1.2 Prandtl for water and oil side

The Prandtl number is related to the thickness of the thermal boundary layer. When the fluid flows on a heated plate, then the particles in direct contact to the surface reach the same temperature of the wall, keeping thermal equilibrium. Energy (heat is a form of energy) towards the upper layers will be exchanged as momentum and temperature tends to the temperature of the fluid as equal as far from plate. In this case this represent a boundary layer development in thermal way and the dimensionless parameter utilized is the Prandtl number Pr.

By definition, it is:

$$Pr = \frac{\text{momentum diffusivity}}{\text{heat diffusivity}} = \frac{\nu}{\alpha} = \frac{\mu c_p}{\lambda} \quad (4.13)$$

In table some of typical Pr for fluids at $T = 60^\circ C$ are listed:

Table 4.6: Prandtl number of typical substances.

Fluid	Pr
Water	3.79
Lube Oil	1050
Freon-12	3.5
Glycol	51
Alcol	10.6

For our purpose, the Pr is calculated set:

- WATER Pr=1.987;
- OIL Pr=276;

Table 4.7: Prandtl number for our application, water at $T = 360\text{K}$, oil at $T = 373\text{K}$.

Fluid	$\nu [m^2/s]$	$\alpha [m^2/s]$	$\mu [kg/ms]$	$c_p [J/kgC]$	$\lambda [W/mC]$
Water	$0.33 \cdot 10^{-6}$	$1.66 \cdot 10^{-7}$	$0.320 \cdot 10^{-3}$	4204	0.674
Oil	$20.3 \cdot 10^{-6}$	$7.38 \cdot 10^{-8}$	$17.1 \cdot 10^{-3}$	2219	0.137

4.1.3 Nusselt for water and oil side

There are several empirical relationship for calculating the convective heat transfer coefficient, between the surface and the thermally fully developed flow. The relationship for calculating Nu and Fanning friction factor for a non circular duct are showed in the following table. Nusselt number represent the ratio between the heat transfer by convection respect to heat transfer by conduction, and in this case is adjusted for a rectangular section, corrected by a shape factor linked to the dimension of the two sides a and b.

Table 4.8: Nusselt number, friction factor for thermally fully developed flow regime.

a/b	Nu $q_{spf} = cost$	f
1	3.61	56.92/Re
2	4.12	62.20/Re
3	4.79	68.36/Re
4	5.33	72.92/Re
6	6.05	78.80/Re
8	6.49	82.32/Re
∞	8.24	96.00/Re

The Fanning friction factor is a factor that can be read by the Moody’s diagram, and its values depend by the surface roughness (Nikuradse regression):

For more detailed analysis, we have to take into account geometrical factors, by introducing more parameters too. Then, The heat transfer and flow friction characteristics of the plate fin heat exchanger are the analysis of heat transfer factor j and friction factor f .

$$j = St \cdot Pr^{2/3} = \frac{Nu}{Re \cdot Pr^{1/3}} \quad (4.14)$$

where j is the heat transfer factor or Colburn factor, St is the Stanton number;

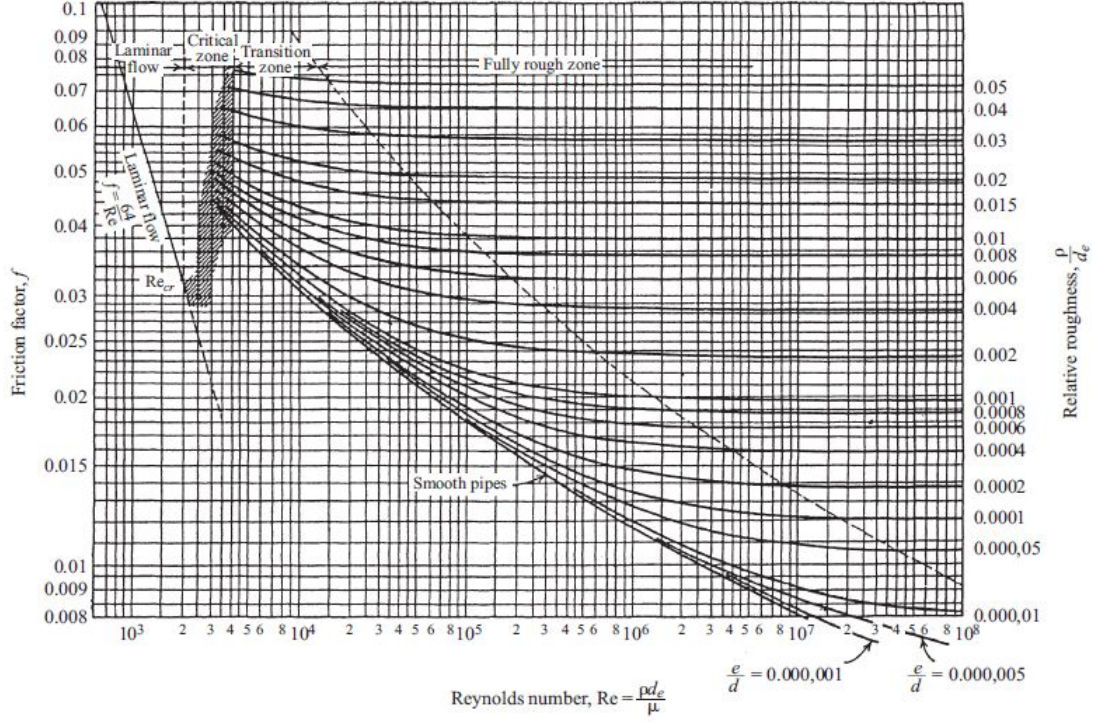


Figure 4.6: Moody's diagram.

Based on the experimental data for 18 different rectangular offset-strip-fin cores listed in Kays and London (1984) the following power law correlations for the Fanning friction factor f and Colburn factor j have been proposed (Manglik and Bergles, 1995) [22]:

$$f_h = 9.6243 Re_h^{-0.7422} \cdot \alpha^{-0.1856} \cdot \delta^{0.3053} \cdot \gamma^{-0.2659} \cdot (1 + 7.669 \cdot 10^{-8} Re_h^{4.429} \cdot \alpha^{0.920} \cdot \delta^{3.767} \cdot \gamma^{0.236})^{0.1} \quad (4.15)$$

$$j_h = 0.6522 Re_h^{-0.5403} \cdot \alpha^{-0.1541} \cdot \delta^{0.1499} \cdot \gamma^{-0.0678} \cdot (1 + 5.269 \cdot 10^{-5} Re_h^{1.340} \cdot \alpha^{0.504} \cdot \delta^{0.456} \cdot \gamma^{-1.055})^{0.1} \quad (4.16)$$

The Nusselt is defined as:

$$Nu = \frac{hD_h}{\lambda} \quad (4.17)$$

where D_h is hydraulic diameter, [m]. Combining equation 4.14 and 4.17, the

convective heat transfer coefficient is presented:

$$h = \frac{j\lambda Re}{D_h} \cdot Pr^{1/3} \quad (4.18)$$

By introducing the ratio between frontal area A_s and cross section of the smallest passage A_c , j expression become:

$$j = \frac{T_{out} - T_{in}}{\Delta \bar{T}} Pr^{2/3} \frac{A_c}{A_s} \quad (4.19)$$

the value of D_h is just calculated in previous section, and it is 0.002849m, and where:

$$\Delta \bar{T} = \frac{\Delta T_{max} - \Delta T_{min}}{\ln\left(\frac{\Delta T_{max}}{\Delta T_{min}}\right)} \quad (4.20)$$

which is $T_w - T_{out}$ during heating and $T_{out} - T_w$ during cooling, [K]; T_w is the wall temperature, [K];

Combing the hydraulic diameter D_h (Eq. (8)) and the mean temperature difference, the heat transfer factor j is expressed in Eq. :

$$j = \frac{D_h}{Pr^{2/3}} \ln\left(\frac{T_w - T_{in}}{T_w - T_{out}}\right) \quad (4.21)$$

Neglecting the fluid loss of inlet and outlet, the friction factor f can be obtained by:

$$f = \frac{\Delta P D_h}{2\rho u^2 L} \quad (4.22)$$

Table 4.9: Results: Colburn factor and Fanning factor f for the two sides, water and oil.

channel	Re_h	α	γ	δ	f	j
Water	6238	1.1071	0.0645	0.0444	0.0464	0.0087
OIL	66	1.1071	0.0645	0.0444	0.9675	0.050719

Once obtained the two main factor j and h , the others results are rapidly derived.

Table 4.10: .

Fluid	j	λ	Re	D_h	Pr
Water	0.0087	0.681	6238	0.0024	1.987
OIL	0.050719	0.137	66	0.0024	276

$$h_{water} = \frac{j\lambda Re}{D_h} \cdot Pr^{1/3} = 5189W/m^2K \quad (4.23)$$

$$h_{oil} = \frac{j\lambda Re}{D_h} \cdot Pr^{1/3} = 1637.77W/m^2K \quad (4.24)$$

Based on the above relations, the heat transfer and flow friction characteristics of fins can be calculated from the fluid properties, channel shape, the parameters of inlet and outlet.

Resume of the results of this section, about Nu , Re , Pr , j , f , h for water and oil side.

Table 4.11: Resume of parameters by empirical correlation for the actual strip-fin heat exchanger.

Side	Re	Nu	Pr	j	f	h	St	$\Delta P/\Delta x$
Water	6238	21.71	1.81	0.0104	0.0464	5489	0.070	9580
OIL	66	24	174.6	0.0507	0.9675	1637.77	0.0016	14187

In order to explain the value of the fluidinamic parameters, it is necessary to recall some definition of the dimensionless number listes above. In particural the fanning friction coefficient f can be arranged in a way that shows the poessure drop:

$$f = \frac{\frac{\Delta P}{\Delta x} D_h}{2\rho u^2} \quad (4.25)$$

where $\Delta P/\Delta x$ and h represent the mean pressure gradient in the main flow direction and the convective heat transfer coefficient, repsectively.

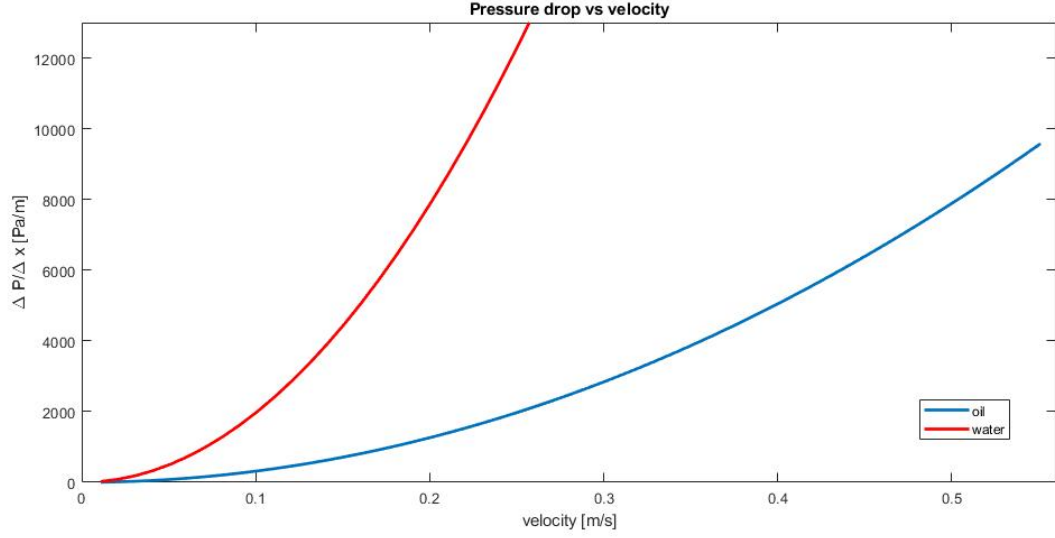


Figure 4.7: Pressure drop trend at different velocity of the two fluids.

From the formulas utilized, is defined the volume goodness factor, in terms of Stanton number, and the area goodness factor in terms of Colburn factor and Fanning factor:

- Volume goodness factor = $\frac{St}{f^{1/3}}$
- Area goodness factor = $\frac{j}{f}$

4.2 ε -NTU method

The overall geometry and the exchanger surface geometry are just specified and are used to calculate the free flow area and the heat transfer area of each side. The convective heat transfer coefficients must be scaled based on a temperature effectiveness of the heat transfer surface. The temperature effectiveness and the fin effectiveness is calculated using following equations (Incropera and DeWitt, 2002). Note, equations need to be evaluated for each side of the heat exchanger.

$$\eta_o = 1 - \frac{A_f}{A_f + A_{pr}}(1 - \eta_f) \quad (4.26)$$

where:

- η_o is the overall temperature effectiveness of the heat transfer surface;
- η_f is the fin efficiency;
- A_f is the fin surface area for the strip fin heat exchanger, [m²];
- A_{pr} is the primary surface area, [m²];

Fin Effectiveness of Thin Sheet Fins is defined as follow, and set at 0.87 for $T^*=0.92$, (4.8):

$$\eta_f = \frac{\tanh\left(\sqrt{\frac{HP}{\lambda A_c}} H\right)}{\sqrt{\frac{HP}{\lambda A_c}} H} \quad (4.27)$$

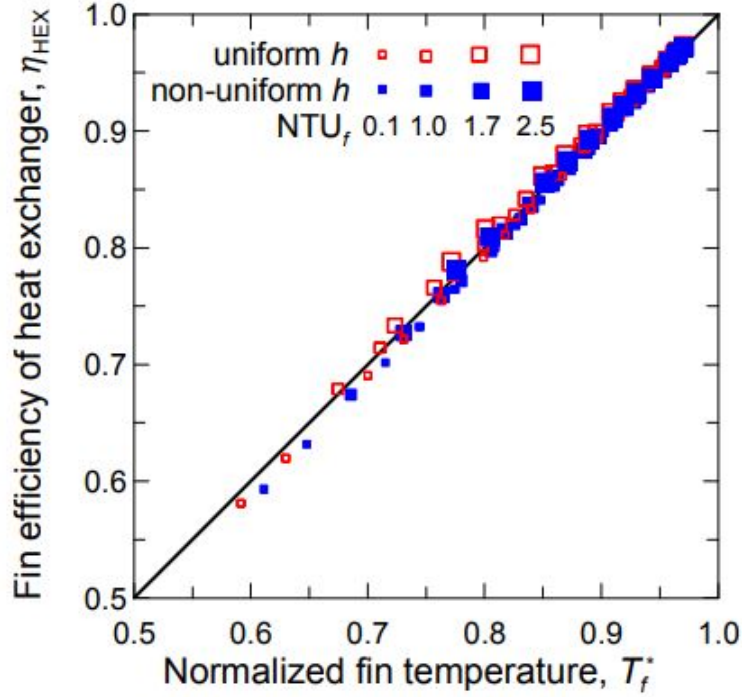


Figure 4.8: Calculation results of Manglik-Bergles correlation, [24].

Using circuit analogy for thermal resistances, is possible to evaluate the thermal conductivities which are the inverse of the resistances 4.9 , and in this way evaluation of the hot side and cold side is done, so an appropriate substitution of the convective heat transfer coefficient is useful for next calculation.

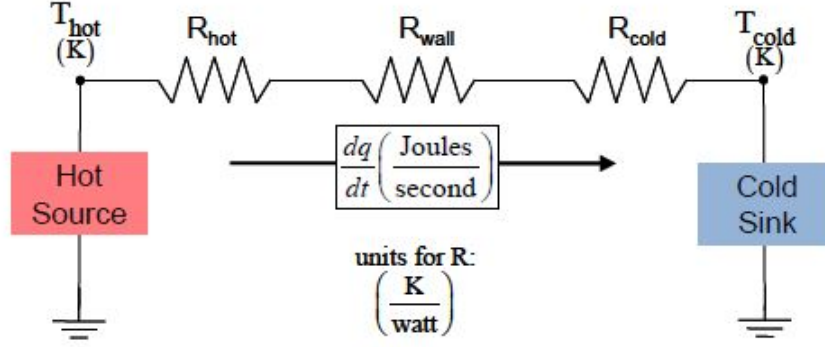


Figure 4.9: Circuit thermal resistancies analogy for the two sides.

$$R_{wall} = \frac{a}{A_{tr}/2\lambda} \quad (4.28)$$

It is negligible because of the thickness of the plate which not affect thermal resistance.

$$R_{hot} = \frac{1}{\eta_0 h_h A_h} \text{ for oil side} \quad (4.29)$$

$$R_{cold} = \frac{1}{\eta_0 h_c A_c} \text{ for water side} \quad (4.30)$$

It is object of interest for the analysis, the inverse of the combined resistance, which represent the overall thermal conductance, defined as:

$$\frac{1}{U_h A_h} = \frac{1}{U_c A_c} = R_{tot} = R_{wall} + R_{hot} + R_{cold} \quad (4.31)$$

Where:

- U is the overall heat transfer coefficient, [$\frac{W}{m^2K}$];
- hot is referred to oil side, instead cold is referred to water one.

Where $R_{fouling}$ is the the resistance caused by fouling. Finally, the overall heat transfer coefficient for unit area is:

$$U = 604.2W/m^2K \quad (4.32)$$

Table 4.12: Resistances of the fluids in the heat exchanger.

Side	h_{side}	$A_{side} [m^2]$	η_o	R_{side}	$R_{fouling}$
hot	1637	3.978e-4	0.87	0.00111	1.75e-4
cold	5489	3.978e-4	0.87	1.92e-4	1.75e-4
wall		0.084		0.0345	

The thermal verification calculation is performed on an already existing exchanger of which they are notes:

- total heat exchange area;
- mass flow rates;
- temperatures of entry of the two fluids.

In this case the goal is to determine the power thermal exchanged and the outlet temperatures of the two fluids. The heat calculation of the exchangers normally takes place using the equations of mass and energy balance which are normally obtained by considering heat exchangers as open systems when fully operational, globally adiabatic. Applying mass balance and fluid energy equations the following formulas are obtained:

$$W_t = G_h(h_{h,in} - h_{h,out}) = G_h c_{ph}(T_{h,in} - T_{h,out}) \quad (4.33)$$

$$W_t = G_c(h_{c,out} - h_{c,in}) = G_c c_{pc}(T_{c,out} - T_{c,in}) \quad (4.34)$$

where the thermal flow rate $C [W/K]$ is introduced:

$$C_h = G_h c_{ph} \quad (4.35)$$

$$C_c = G_c c_{pc} \quad (4.36)$$

The two equations become, respectively:

$$W_t = C_h(T_{h,in} - T_{h,out}) \quad (4.37)$$

$$W_t = C_c(T_{c,out} - T_{c,in}) \quad (4.38)$$

To these two energy balance equations, an exchange thermal equation can be associated. It is important to note that having only three independent equations available (energy balance for the two fluids and the heat exchange equation), can be maximized three unknown variables of the exchanger between: the four temperatures, the two flow rates, the power exchanged and the exchange surface.

4.2.1 LMTD method

In this case the thermal power exchanged between the two fluids is linked to the difference of temperature between the hot fluid and the cold fluid:

$$W_t = UA(T_{hot} - T_{cold}) = UA\Delta T_{ml} \quad (4.39)$$

However, since ΔT varies with the position inside the heat exchanger it is necessary to use a suitably mediated temperature difference. For a counter-flow heat exchanger, the LMTD is calculated as:

$$\Delta T_{ml} = \frac{\Delta T_1 - \Delta T_2}{\ln\left(\frac{\Delta T_1}{\Delta T_2}\right)} \quad (4.40)$$

where:

$$\Delta T_1 = T_{h,in} - T_{c,out} \quad (4.41)$$

$$\Delta T_2 = T_{h,out} - T_{c,in} \quad (4.42)$$

In our application, LMTD is 62°C.

4.2.2 Ntu and effectiveness method

To obtain an expression of the heat exchange equation that does not include any outlet temperature is defined as the efficiency of an exchanger, ϵ , the relationship between thermal power actually exchanged in the exchanger and the maximum heat output exchangeable.

$$\epsilon = \frac{W_t}{W_{t,max}} \quad (4.43)$$

The maximum exchangeable heat output is that which can be realized in an exchanger in which the fluid with a lower thermal capacity undergoes the maximum

possible temperature difference without violating the second principle of thermodynamics, and this occurs when it comes out of the exchanger at a temperature equal to that of the second fluid inlet. In other words:

$$W_{t,max} = C_{min}(T_{h,in} - T_{c,in}) \quad (4.44)$$

This power could be obtained with a counter-flow heat exchanger with an infinite exchange surface;

Table 4.13: input parameters for NTU method.

$T_{h,in}$	$T_{c,in}$	G_c	c_{pc}	G_h	c_{ph}	W_t	$W_{t,max}$	C_{min}	C
115	90	0.1583	4210	0.0719	2307	1657	4143	165.75	0.24

$$\epsilon = \frac{W_t}{W_{t,max}} = 40\% \quad (4.45)$$

Note the thermal efficiency is simple to read the value of NTU in the graphic below:

$$NTU = \frac{UA}{C_{min}} = 0.540 \quad (4.46)$$

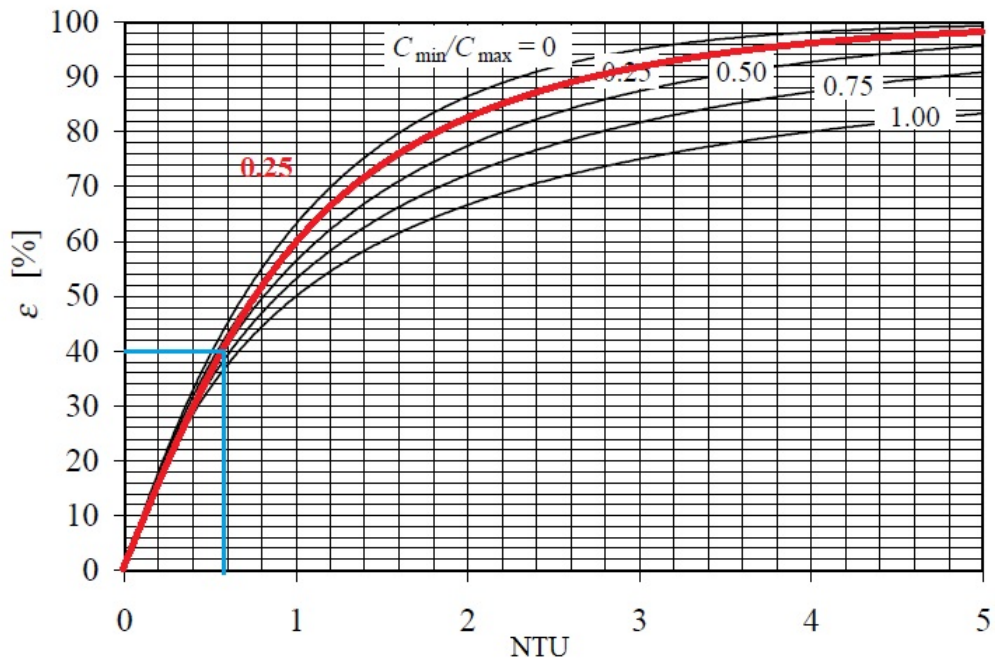


Figure 4.10: NTU for counter-flow heat exchanger.

Efficiency increases rapidly for NTU about 1.5, rather slowly for great values. For a given NTU and C the greater efficiency is that relative to a counter-flow exchanger followed closely by a cross-flow heat exchanger. The efficiency is independent of the C capacity ratio for NTU values less than 0.3.

Chapter 5

CFD analysis for flow through in Heat exchanger

This chapter summarizes a methodology of simulating pressure drop and heat transfer coefficient considering simple passage without inner turbulator firstly, then within turbulator. The validation method starts with simulated flow through turbulator section, representative of the periodic developing of the geometry in the HX. STAR CCM+ software is utilized to perform simulation, and the results are compared to test data provided by ICP for the engine. It is important to consider same specific parameters which involves in heat exchanger's performance: Fanning factor related to pressure loss and Colburn factor that consider heat transfer quality.

There are a lot of different correlations proposed for evaluation of j and f , all referred to different operating conditions. In particular it is useful to remember Manglik & Bergles Correlation [25] and ALEX equations for offset strip fins exchanger. Reynolds number is the main term which differs in the dissertation. Eventually, comparison of the CFD results and test data is proposed.

5.1 STAR CCM+ Modelling/Simulation

As mentioned in the previous chapter, the heat transfer and flow friction characteristics of fins can be calculated from the fluid properties, channel shape, the

parameters of inlet and outlet. The ALEX correlation is in $300 \leq Re \leq 7500$:

$$\ln j = -2.64136 \cdot 10^{-2}(\ln Re)^3 + 0.555843(\ln Re)^2 - 4.09241(\ln Re) + 6.21681 \quad (5.1)$$

where Re is calculated considering the hydraulic diameter of the turbulator's fin.

$$\ln f = 0.132856(\ln Re)^2 - 2.28042(\ln Re) + 6.79634 \quad (5.2)$$

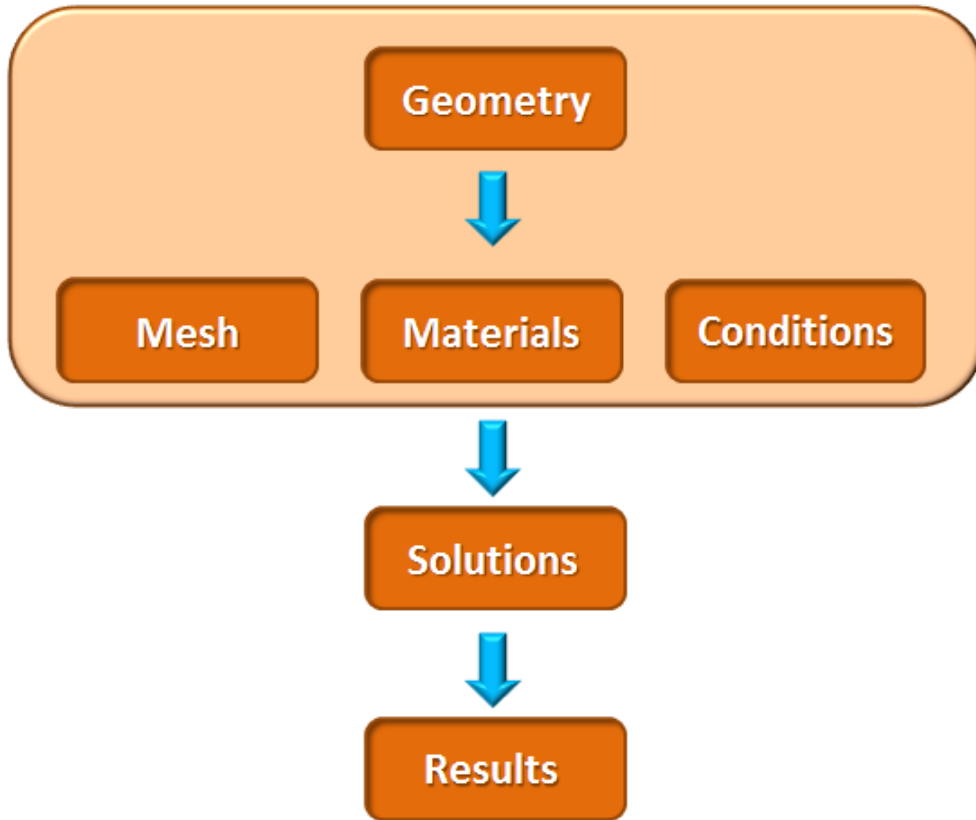


Figure 5.1: CFD approach for simulation.

Star CCM+ is adopted to conduct the simulation for heat transfer and flow friction characteristics of offset turbulator's fins. The conservation equations of mass, momentum, and energy are shown as follows:

$$\frac{\partial \rho}{\partial t} + \frac{\partial \rho u_x}{\partial x} + \frac{\partial \rho u_y}{\partial y} + \frac{\partial \rho u_z}{\partial z} = 0 \quad (5.3)$$

where $u_{x,y,z}$ are the velocity component along x, y and z direction.

Momentum equation that are three vectorial expression in the three directions, too:

$$\frac{\partial \rho u_x}{\partial t} + \nabla(\rho u_x \mathbf{u}) = -\frac{\partial p}{\partial x} + \nabla(\mu \mathbf{grad} u_x) + S_{u_x} \quad (5.4)$$

$$\frac{\partial \rho u_y}{\partial t} + \nabla(\rho u_y \mathbf{u}) = -\frac{\partial p}{\partial y} + \nabla(\mu \mathbf{grad} u_y) + S_{u_y} \quad (5.5)$$

$$\frac{\partial \rho u_z}{\partial t} + \nabla(\rho u_z \mathbf{u}) = -\frac{\partial p}{\partial z} + \nabla(\mu \mathbf{grad} u_z) + S_{u_z} \quad (5.6)$$

where p is the pressure measured in Pa and S_{u_i} is referred to source term, in most general formulation. Whereas the energy equation is:

$$\frac{\partial \rho E}{\partial t} + \nabla[\mathbf{u}(\rho E + p)] = \nabla \cdot [k_{eff} \mathbf{grad} T - \sum_j h_j J_j + (\tau_{eff} \cdot \mathbf{u})] + S_h \quad (5.7)$$

where E is the total energy of fluid, [J/kg]; h is entalpy, [J/kg]; k is the heat transfer coefficient, $W/(m^2K)$; J_j represents diffusion flux; τ is viscous stress, Pa. In the flow of circular pipe, Reynolds numbers Re less than 2300 is assumed as laminar flow, instead many compact surfaces, especially those with periodically interrupted passages such as corrugations or offset strip fins, like the actual heat exchanger, have effectively transitional flow at Reynolds numbers as low as about 300. In the following simulations, the Reynolds numeber is calculated considering D_h referred to the smallest passage for water side and oil side, respectively.

5.1.1 Geometry

Basic structure of the finned turbolator is shown in the picture below. A cad model is imported into StarCCM+ CAD scene. The operation take place in the following order:

- right click on geometry and oped a new cad scene;
- right click on the 3D-model node at the top of scene tree and select import cad model;
- once select cad file browsing into its folder, take a look to the cad repair tick, to resolve the component and avoid geometric issue.
- finally, import and visualize in the sketch plane.

At this point is sufficient to enclose the actual cad into a suitable volume extruded by a sketch. by the way, a new body is created as computation domain which not absorb the previous and inner piece, if body interaction option is set as "none". It is important to not "merge" the two bodies and the fluid body just created to not slice the first body: non-manifold geometry warning will appear like an error.

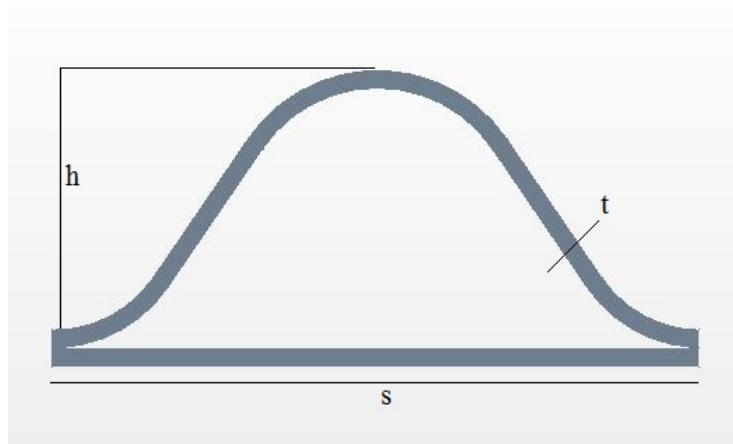


Figure 5.2: Solid part considered in the simulation, periodical repetition in x direction.

After creating two bodies, rename the last one as fluid domain: this will result more simple for setup of parts and regions into solver. The fluid domain has a block-like shape, the specifications are posted in the following table, all the measures are

referred to the lab reference:

Table 5.1: Fluid domain spec.

Parameter	x[mm]	y[mm]	z[mm]
fluid domain	7.5	100	4

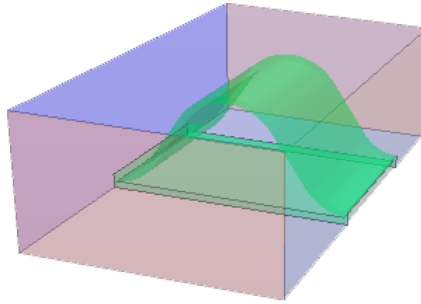


Figure 5.3: Computational domain.

In the table below, geometry parameters of the fins are presented. The main aim for simulation is to keep down the computational effort by reducing number of cells but not their quality at the same time. Moving on this track, it is necessary to reduce the computational domain considering the periodic repetition of the same geometry in the space 5.4 . In this case, turbulator presents the repetition of the same wave in the x direction, so it is sufficient to consider only one representative wave:

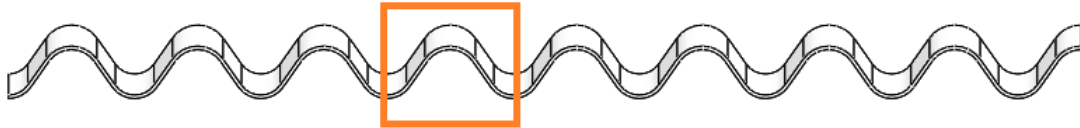


Figure 5.4: Inner turbulator section.

The geometric setup of 3D-CAD is over, the following step is the regions creations for simulation.

Table 5.2: Geometrical features of fin.

Parameter	h[mm]	s[mm]	t[mm]	length [mm]
fin	2.8	7	0.5	4.5

5.1.2 Mesh

In simulation environment, the bodies will be converted to regions. Firstly, parts is created :

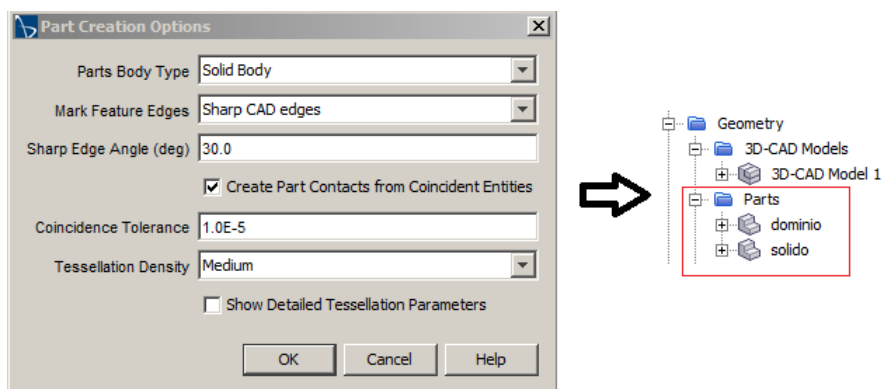


Figure 5.5: New geometry part.

Selecting "split by patch" option, inlet and outlet are assigned, renaming the entrance face of the fluid domain and the exit one, in streamwise directions. After this, two parts are inserted in the part tree node. Now, right clicking the same node, assign part to region is required to generate interactive entities from the two bodies. Attention must be paid to settings in this dialog window, because of interface options which define the new regions.

The table below, 5.6, presents all the boundaries type and characteristics assigned to the bodies.

Meshing process involves two different mesh definition, one for the fluid domain with specific setting, and another one for solid region. The generation of the grid is important for calculation: a fine grid mesh is strictly required in the boundary region near the wall, a coarse mesh is sufficient to discretize the rear space surrounding the solid body. As well as the previous table, the following one resume all the selected option to generate the mesh.

Regions	Type	Parts	Boundaries	Type
<i>Dominio</i>	Fluid Region	Dominio	Bottom	Simmetry plane
			Default_Dominio	Wall
			Def_Inteface	Contact Boundary
			Destro	Simmetry plane
			Inlet	Velocity Inlet
			Outlet	Pressure Outlet
			Sinistra	Simmetry plane
Top	Simmetry plane			
<i>Solido</i>	Solid Region	Solido	Default_solido	Wall
			Def_Inteface_solido	Conctat Interface
<i>Interfaces</i>	Contact Interface	Solido/Dominio		Contact Interface
			Topology	In place

Figure 5.6: Properties.

	Models	Reference Values	
<i>Mesh Fluid Domain</i>	Polyedral Mesh	Base Size	0.1 mm
	Prism Layer Mesher	Number of Prism Layers	10
	Surface Remesher	Prism Layer Thickness	2.33E-04
		Prism Layer Stretching	1.3
		Surface Curvature	40 pts/circle
		Surface Growth Rate	1.1
		Relative minimum size	0.005 mm
		Relative target size	0.05 mm
<i>Mesh Solid</i>	Surface Remesher	Base Size	0.01 mm
	Thin Mesher	Surface Growth Rate	1.1
		Thin mesh Layer	3
		Prism Layer	Disable

Figure 5.7: Mesh properties.

5.1.3 Mesh Outline

- **Surface Remesher:** it is often used to retriangulate the surface. The remeshing is primarily based on a target edge length that you supply and can also include feature refinement that is based on curvature and surface proximity [27].
- **Polyedral Mesh:** the polyhedral meshing model utilizes an arbitrary polyhedral cell shape in order to build the core mesh. The polyhedral core mesh density can be increased or decreased by using the volume mesh density factors. Volumetric controls that are chosen from a range of prescribed shapes can also be included to increase or decrease the mesh density locally. The maximum limit of polyhedral cells per process is 120 million cells [27].
- **Prism Layer Mesher:** the prism layer mesh model is used with a core volume mesh to generate orthogonal prismatic cells next to wall surfaces or boundaries. This layer of cells is necessary to improve the accuracy of the flow solution [27]. A prism layer is defined in terms of thickness, number of layers, size of layers, function to generate the distribution. Prism layers allow the solver to resolve near wall flow accurately, which is critical in determining not only the forces and heat transfer on walls, but also flow features such as separation. Separation in turn affects integral results such as drag or pressure drop. Using a prism layer mesh allows you to resolve the viscous sublayer directly if the turbulence model supports it (low $y^+ \sim 1$). Alternatively, for coarser meshes it allows the code to fit a wall function more accurately (high $y^+ < 30$).

Cell quality indicators are plotted thanks to macro. Playing the "meshquality-macro" [28], it is easy to ensure the mesh quality, considering the following parameters:

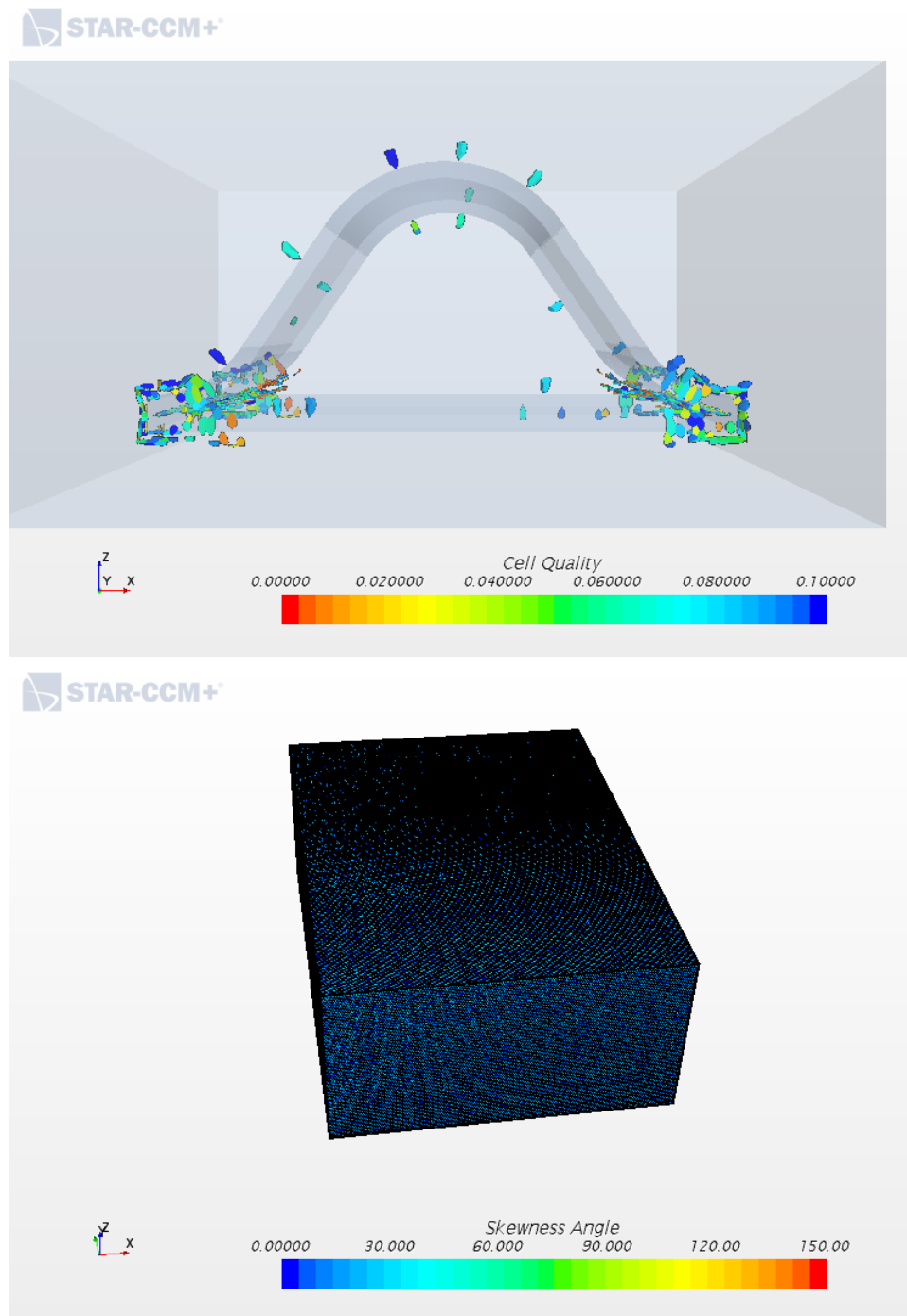


Figure 5.8: Mesh quality: output of the macro runned into StarCCM+.

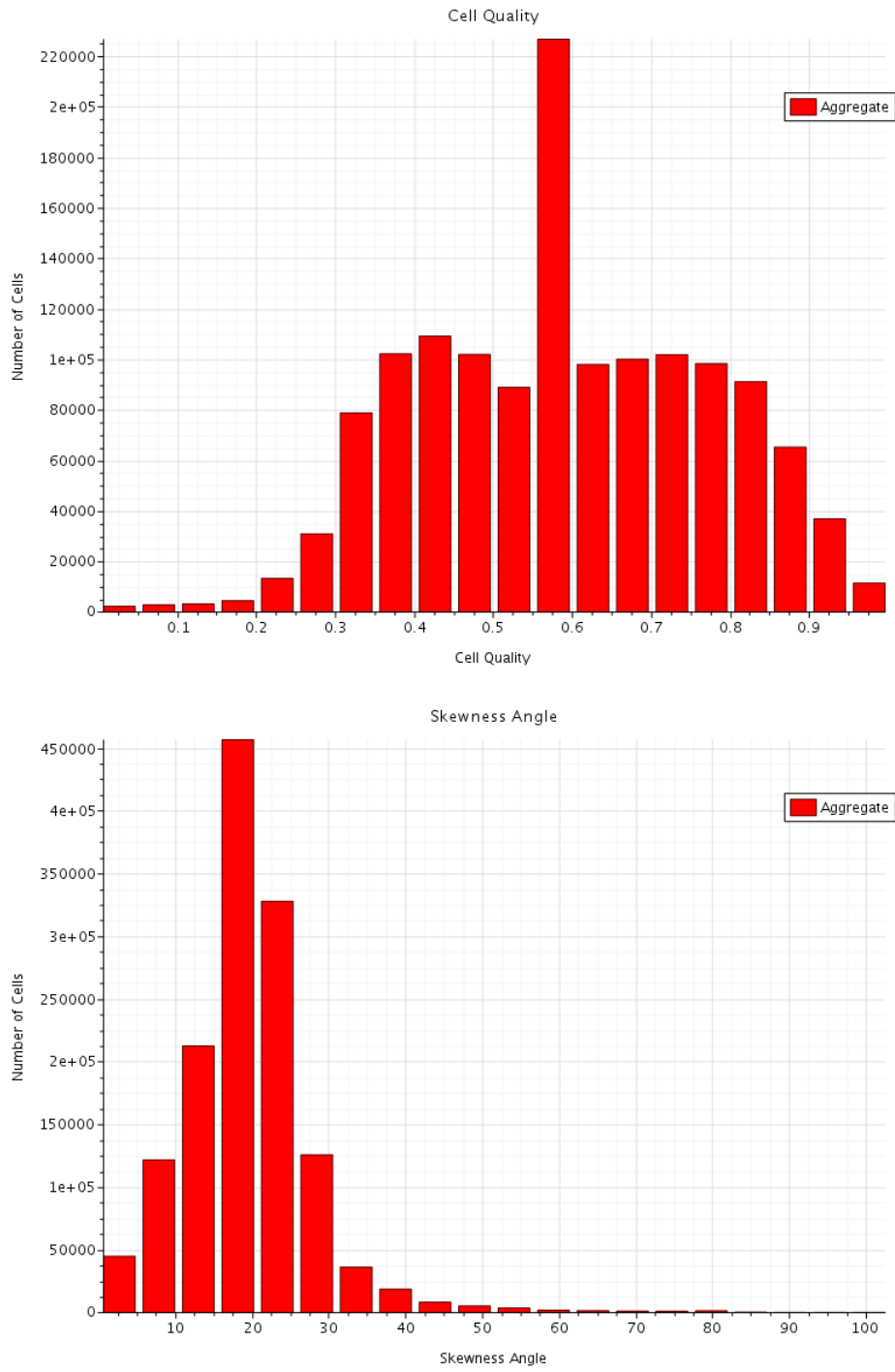


Figure 5.9: Bar chart about mesh properties.

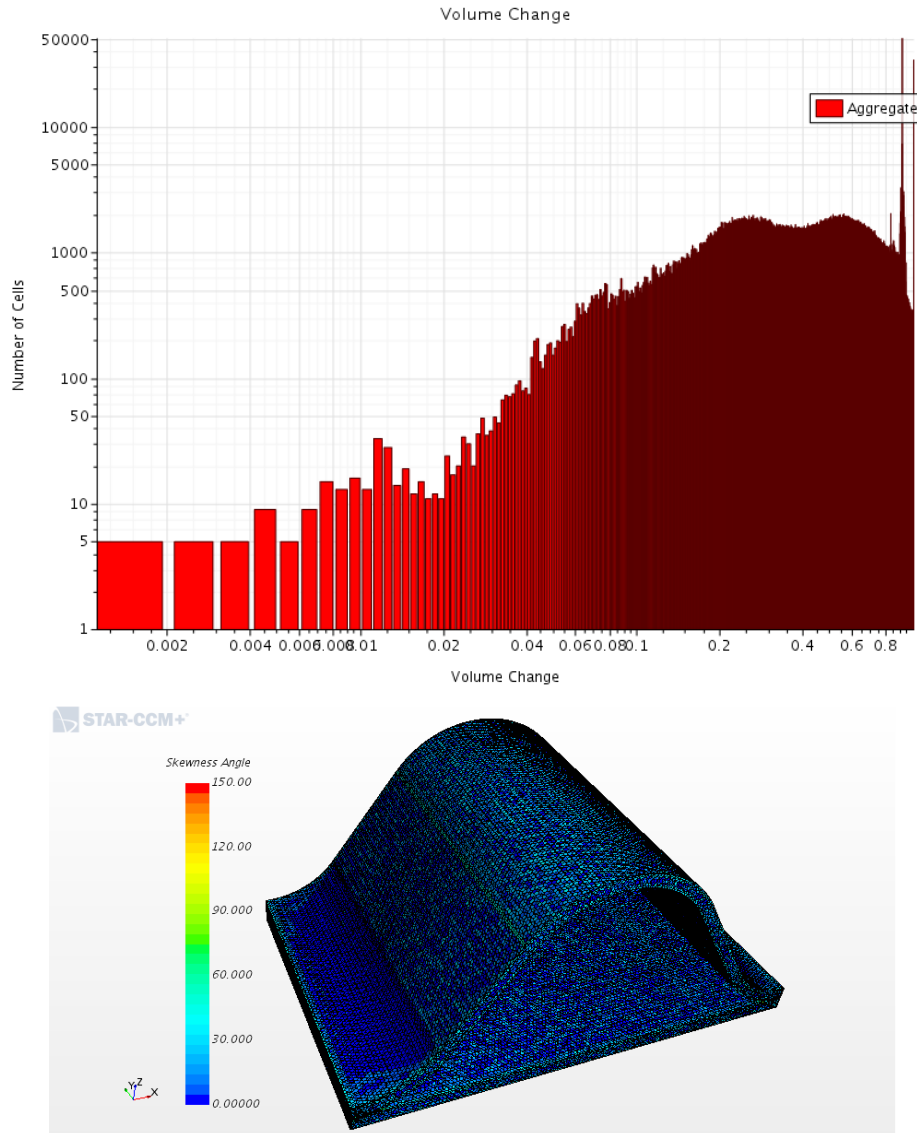


Figure 5.10: Volume mesh properties, macro's output.

After mesh generation, is useful to make sure about the quality and density of the volume mesh. In StarCC+ output window is easy to visualize a compact volume mesh report which exposes all the parameters involved in the grid generation. Several values is reported, but for critical analysis and estimation of the cells quality, particulare point are focused:

- Mesh validity;

- Face validity;
- Volume change;

In the following report related to "dominio" and "solido" meshes executed per-domains, is visible the output value of the upper parameter:

```

-----
--- Computing statistics in Region: dominio
-----
-> ENTITY COUNT:
# Cells: 1432511
# Faces: 7689205
# Verts: 6226343
-> EXTENTS:
x: [-3.5021e-02, -2.7579e-02] m
y: [ 0.0000e+00,  1.0000e-02] m
z: [-6.0057e-04,  3.2300e-03] m
-> MESH VALIDITY:
Mesh is topologically valid and has no negative volume cells.
-> FACE VALIDITY STATISTICS:
Minimum Face Validity: 9.644546e-01
Maximum Face Validity: 1.000000e+00
Face Validity < 0.50                0    0.000%
0.50 <= Face Validity < 0.60        0    0.000%
0.60 <= Face Validity < 0.70        0    0.000%
0.70 <= Face Validity < 0.80        0    0.000%
0.80 <= Face Validity < 0.90        0    0.000%
0.90 <= Face Validity < 0.95        0    0.000%
0.95 <= Face Validity < 1.00        3    0.000%
1.00 <= Face Validity                1032508 100.000%
-> VOLUME CHANGE STATISTICS:
Minimum Volume Change: 6.677691e-03
Maximum Volume Change: 1.000000e+00
Volume Change < 0.000000e+00        0    0.000%
0.000000e+00 <= Volume Change < 1.000000e-06  0    0.000%
1.000000e-06 <= Volume Change < 1.000000e-05  0    0.000%
1.000000e-05 <= Volume Change < 1.000000e-04  0    0.000%
1.000000e-04 <= Volume Change < 1.000000e-03  0    0.000%
1.000000e-03 <= Volume Change < 1.000000e-02  1    0.000%
1.000000e-02 <= Volume Change < 1.000000e-01  10950  1.061%
1.000000e-01 <= Volume Change <= 1.000000e+00 1021560 99.939%

```

Figure 5.11: Compact volume mash report.

- Cell quality histogram: the shape of the cell affects the cell quality. Cells with a quality less than $1.0e-5$ are considered bad, 5.9 .
- Skewness histogram: the skewness angle measures the angle between a face normal and the vector that connects two neighboring cell centroids. Skewness angles of deg 90 or greater typically result in convergence issues, while skewness angle of deg 0 results in perfectly orthogonal cell, 5.9 .
- The volume change metric describes the ratio of the volume of a cell to that of its largest neighbor. 0.01 volume change are considered bad cells, while a large jump in volume among neighboring cells causes accuracy issue and instability, 5.10.

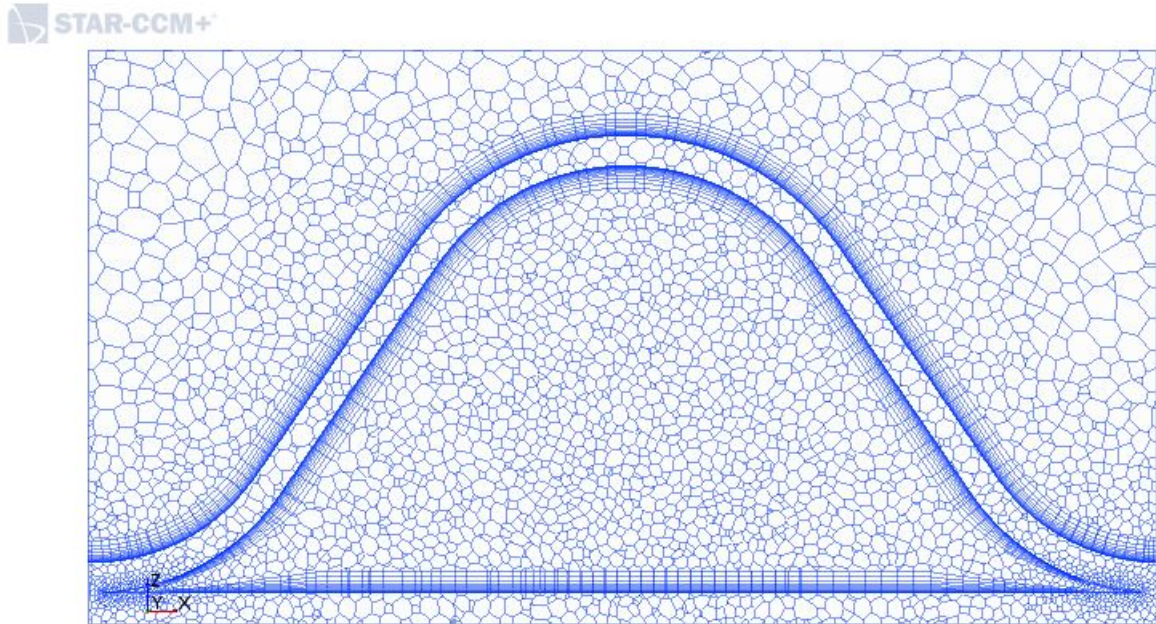


Figure 5.12: Section plane across domain for more comfortable mesh visualization.

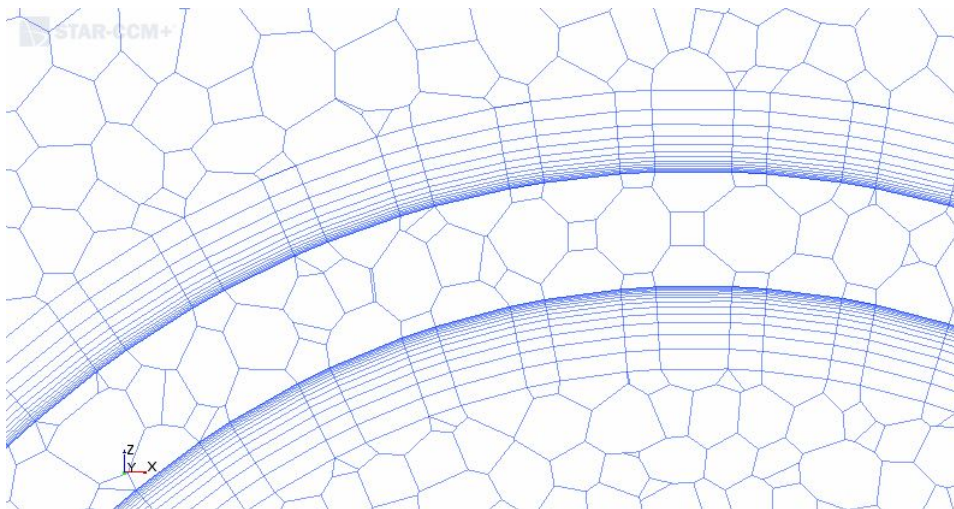


Figure 5.13: Conformity between prism layer and poly mesh.

5.1.4 Wall y^+

Wall treatment models are used in conjunction with RANS models. Three wall treatments options are available in StarCCM+:

- High- y^+ : is a traditional wall function where the centroid of the cell is placed in the log-law region and $30 \leq y^+ \leq 100$;
- Low- y^+ : suitable only for low-Re turbulence models in which the mesh is sufficient to resolve the viscous sublayer, and 10-20 cells are placed in the boundary layer region, $y^+ \approx 1$, 5.14;
- All- y^+ is an hybrid solution to give accurate results if the near wall cell centroid is in the viscous sublayer, the log-law region, or the buffer layer.

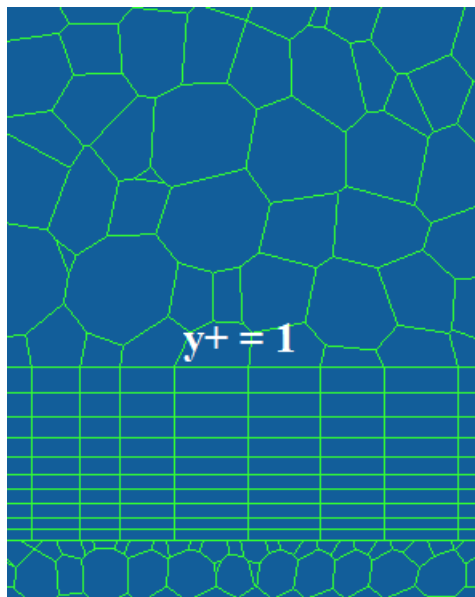


Figure 5.14: $y^+ \approx 1$

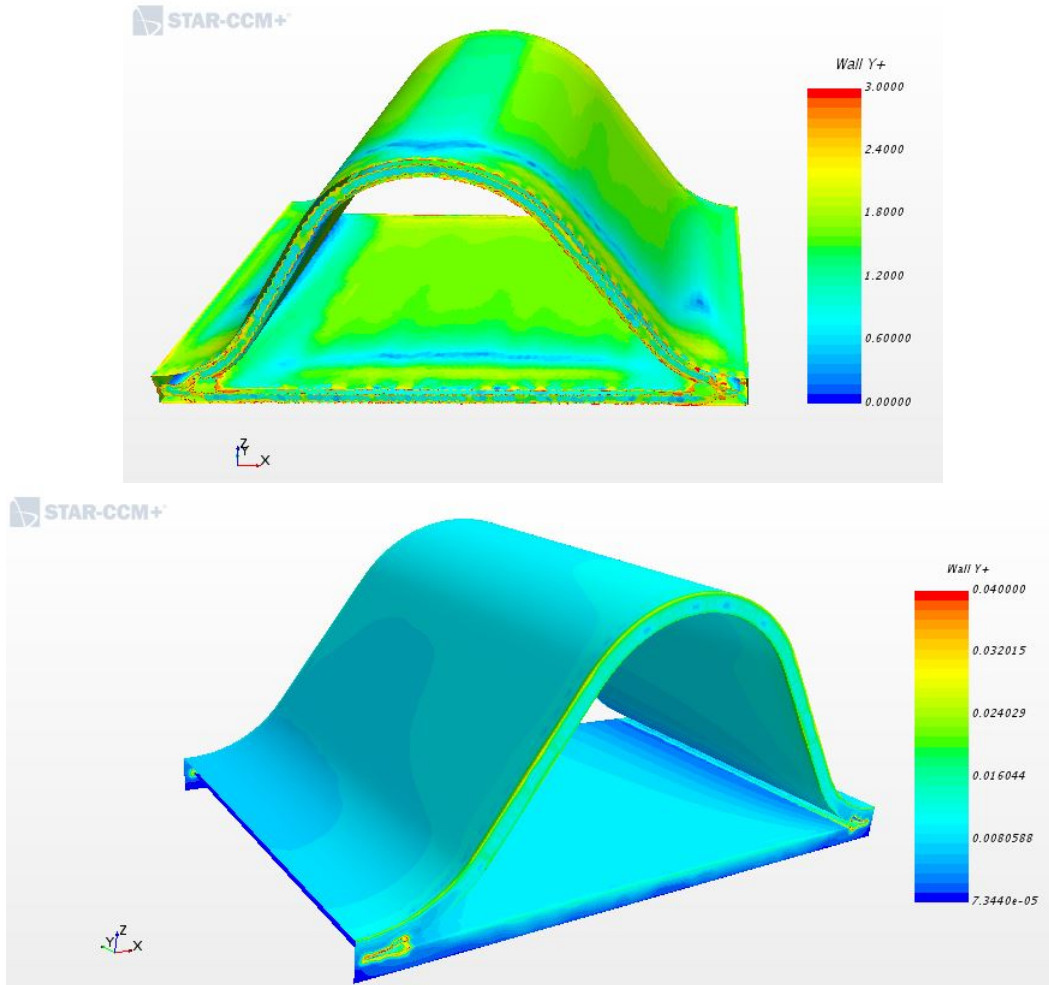


Figure 5.15: 10 layers are improved to capture the viscous sublayer near the wall, choosing a $y^+ \approx 1$. In the first image y^+ range is up to 3, instead in the second one, a refinement of the thin layer prism mesh bring to reduce the y^+ value to 0.05, involving a more accurate solution.

Figure 5.16: Wall y^+ : range 0-3.

Estimating wall y^+ start with desired y^+ : in the upper case, y^+ is set at 3. For example, the table below shows the step for estimating, for pipe flow:

$$\frac{\bar{C}_f}{2} = \frac{0.039}{Re^{1/5}} \quad (5.8)$$

$$\tau_w = \bar{C}_f \cdot \frac{\rho U^2}{2} \quad (5.9)$$

$$u^* \approx \sqrt{\frac{\tau_w}{\rho}} \tag{5.10}$$

We will target a y^+ of 3.

Table 5.3: Water medium, y^+ estimation.

Re	ν	U	ρ	$C_f/2$	τ_w	u^*	y^+
5870	2.82e-4	0.5981	958	0.006876	2.3564	0.04959	3

$$y = \frac{y^+\nu}{u^*} = 1.71\text{mm} \tag{5.11}$$

5.1.5 Models and conditions

After meshing, selecting models and boundary condition set are required. In the present case of study the mesh is polyedral one and conformal, to ensure geometric continuity from cell to cell as well as accuracy improving of the target value. Next step involves models physic for each domains. In particular a solid model and a fluid model to solved a conjugate heat transfer problem. In order to summarize the selections, two table are proposed, one for fluid and last for solid.

Table 5.4: Enabled models for oil side.

Continua	Regions	Models
Oil	Fluid	Three dimensional Steady Liquid Segregated flow Gradients Constant density Turbulent Re-averaged NS K-epsilon turbulence Standard k-epsilon Low-Re Exact wall distance Segregated Fluid Temperature Low y^+ wall treatment

Table 5.5: Enabled models for solid.

Continua	Regions	Models
Oil	Fluid	Three dimensional Steady Solid Segregated solid energy Gradients Constant density

Because of laminar flow, Re is 66 and a suitable turbulence models needed: low-Re and standard k-epsilon help to resolve issue. Moreover, a low y^+ allow us to captured the boundary effect near the wall. Oil is material not included in the library. Replace with a custom material introducing the fluid properties at a certain temperature. Then Aluminium solid medium is selected.

There are few initial conditions to be set, and these are:

Table 5.6: Initial conditions for oil side.

Continua	Initial Conditions	Value
Fluido	Pressure	1.5 bar
	Static Temperature	388K
	Velocity	[0,0.4814,0]m/s
Solido	Static temperature	300K

Instead in Regions, for each boundaries:

For the water side, the options selected are the same, but there are few differences like turbulence models, temperature and HTC.

Solid is the same.

Table 5.7: Regions initial conditions setup.

Fluido	Bound.	Type	Physic cond.	Ref. values
Inlet	Vel. inlet	Default Vel. magnitude	Static Temp.	388K 0.4814m/s
Lateral wall	Simmetry plane			
Outlet	Pressure outlet	1.5bar		
Top surface	Simmetry plane			
Bottom surface	Wall			
Bottom interf.	Shear stress spec. Thermal spec.	no-slip Adiabatic		
Inteface1	Conctact int. bound.			
Turbolator	Wall	Adiabatic		
Interface2	Contact int. bound.			
Interfaces	Fluido/solido	Contact In-place		

Table 5.8: Regions initial conditions setup.

Solido	Bound.	Type	Physic cond.	Ref. values
	Default	Wall	Convection	HTC 300 W/mK

Table 5.9: Enabled models for water side.

Continua	Regions	Models
Water	Fluid	Three dimensional Steady Liquid Segregated flow Gradients Constant density Turbulent Re-averaged NS K-epsilon turbulence Realizable k-epsilon Exact wall distance Segregated Fluid Temperature two-layer y+ wall treatment

Table 5.10: Regions initial conditions setup.

Fluido	Bound.	Type	Physic cond.	Ref. values
Inlet	Vel. inlet	Default Vel. magnitude	Static Temp.	366K 0.8791m/s

5.1.6 Oil side results and validation

Several simulations are played to provide data for validation of results. In particular, variation of the mass flow rate is useful. The following plots show the comparison of empirical trend by correlation and StarCCM+ results referred to different working conditions, as variation of rpm of the engine to which corresponds changing in temperature and pressure. Error trend is plotted in the same range.

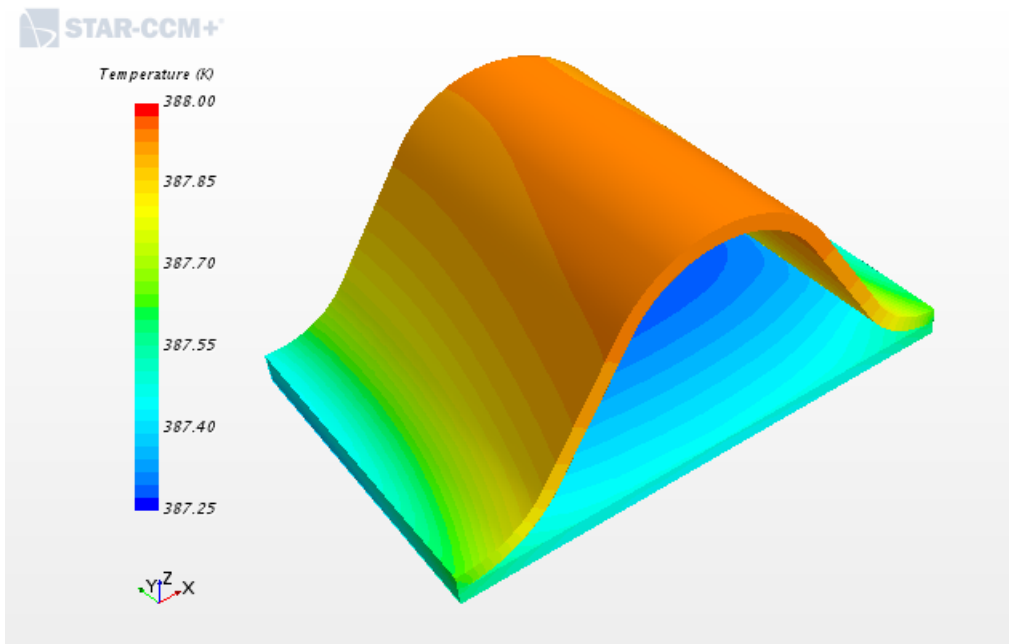


Figure 5.17: Oil temperature.

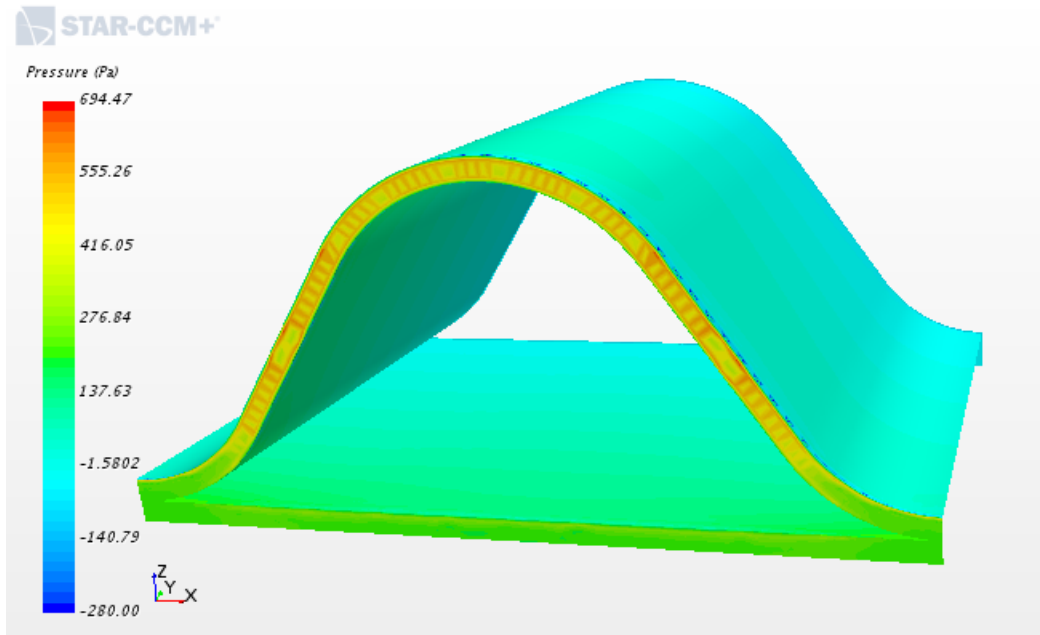


Figure 5.18: Oil Pressure.

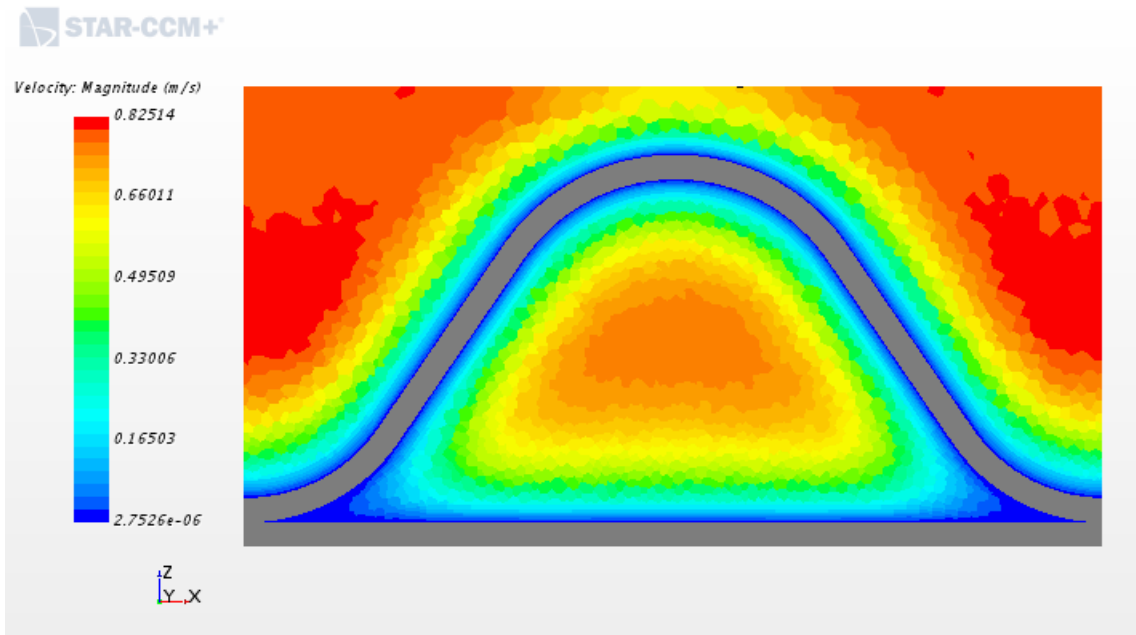


Figure 5.19: Oil velocity.

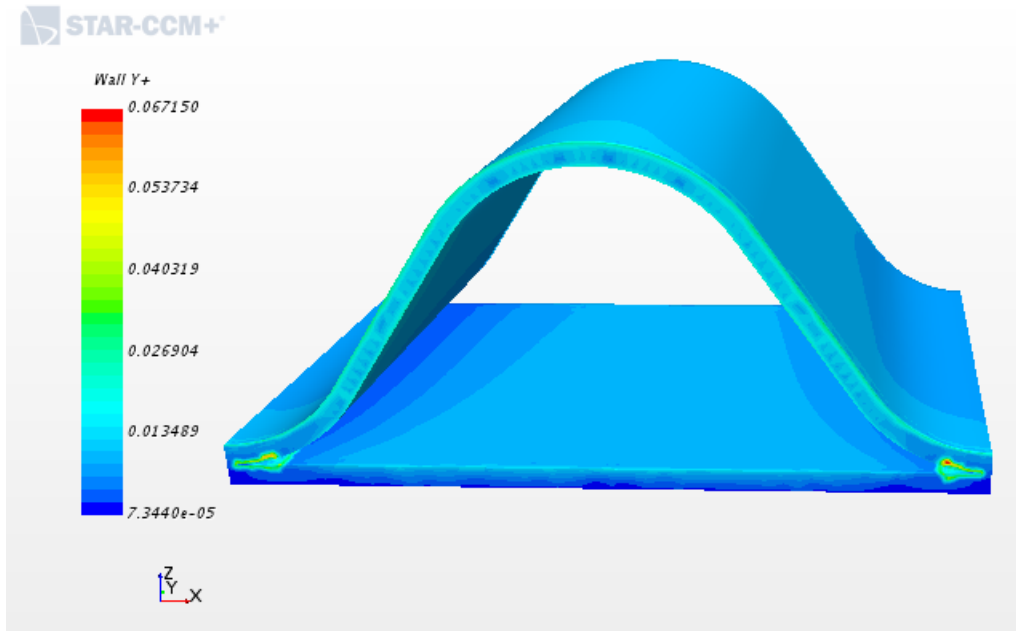


Figure 5.20: Wall y+ oil side.

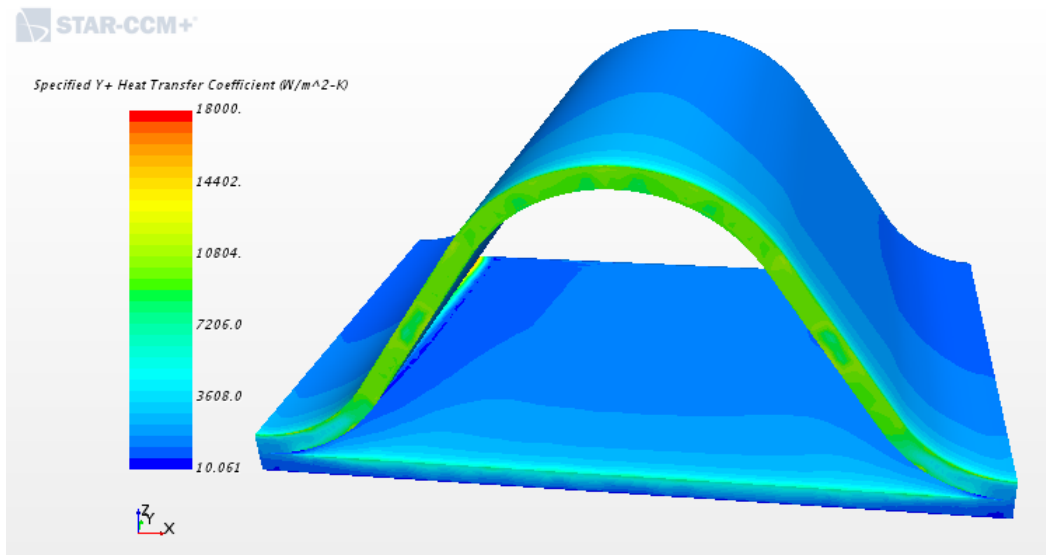


Figure 5.21: Specified Wall y+ heat transfer coefficient.

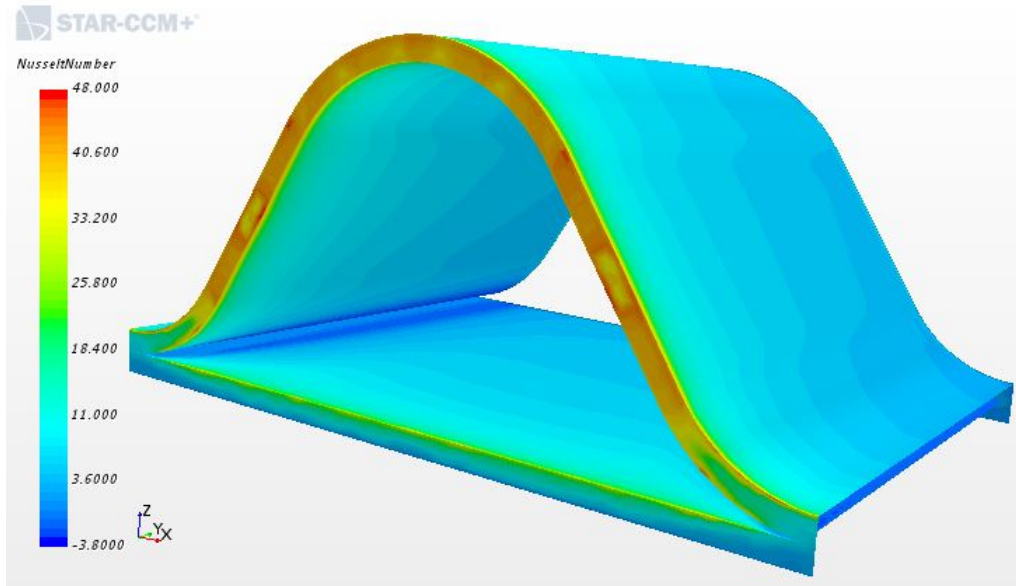


Figure 5.22: Nusselt number for oil.

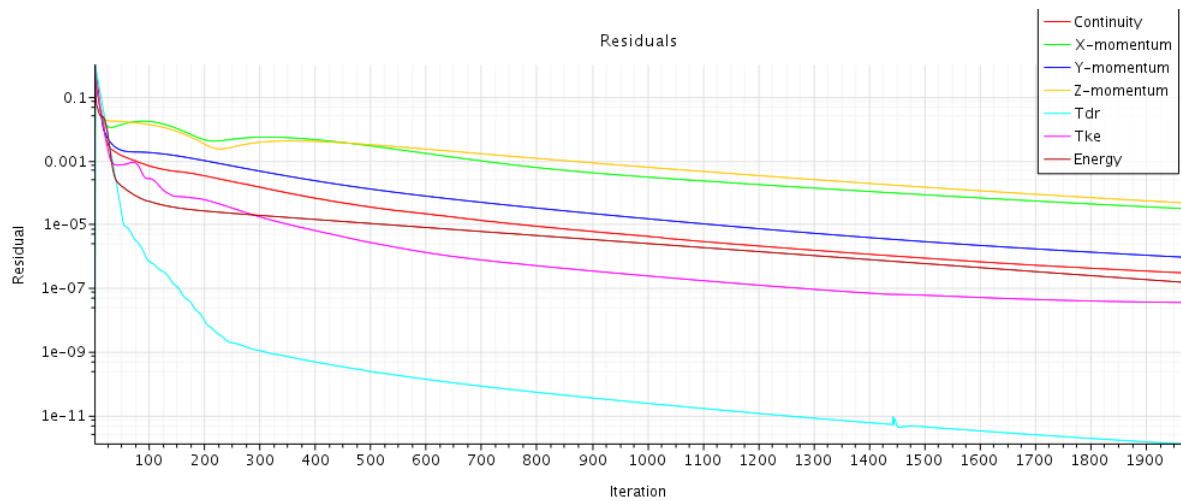


Figure 5.23: Simulation's residuals after simulation.

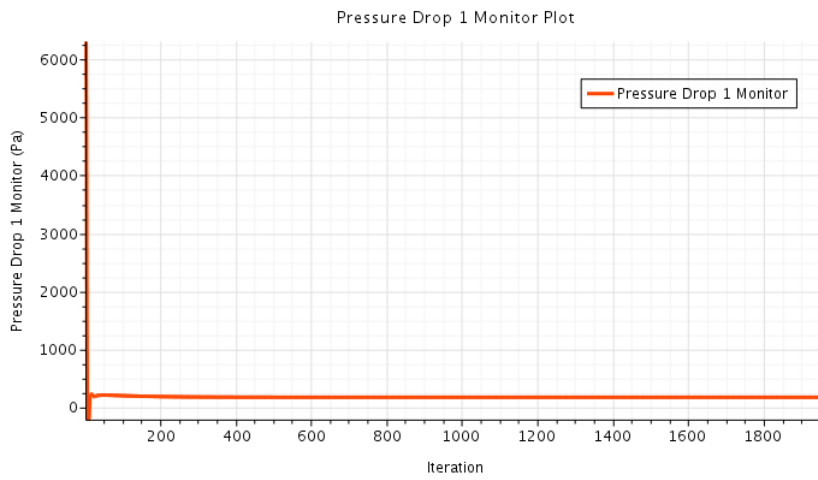


Figure 5.24: Pressure monitor: after convergence, pressure drop is steady at 174Pa.

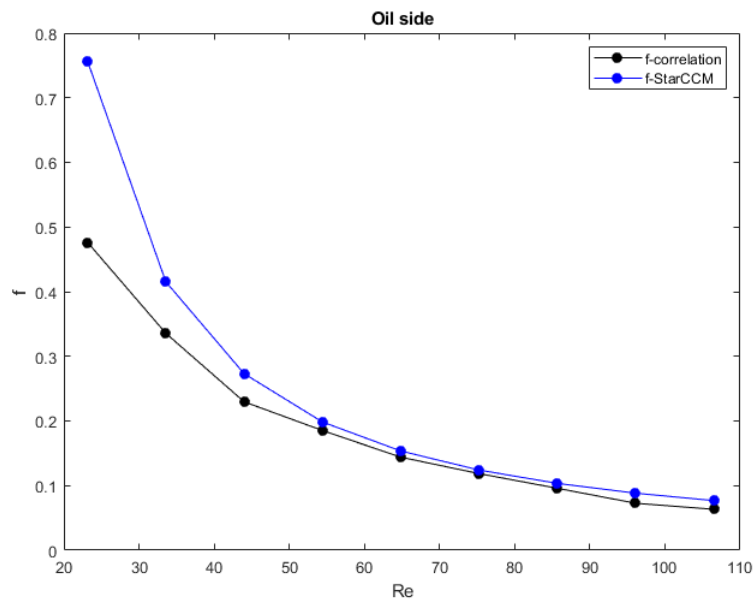


Figure 5.25: Fanning friction coefficient f vs Reunolds number.

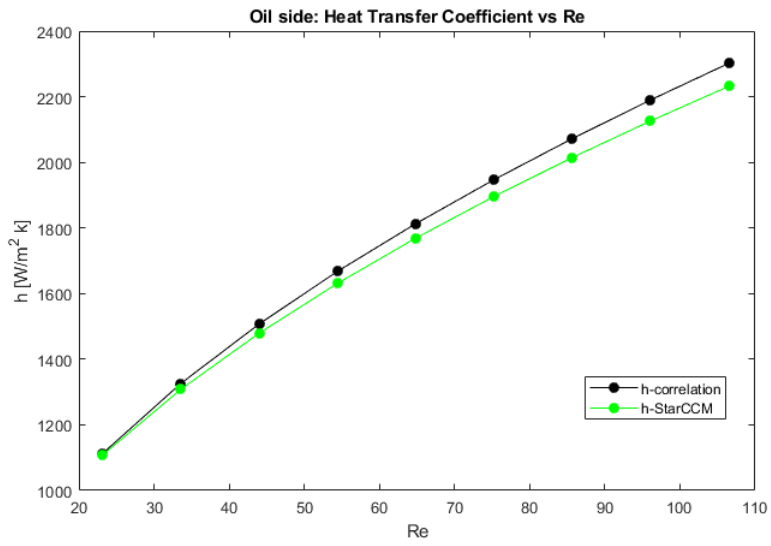


Figure 5.26: Heat transfer coefficient vs Reynolds number.

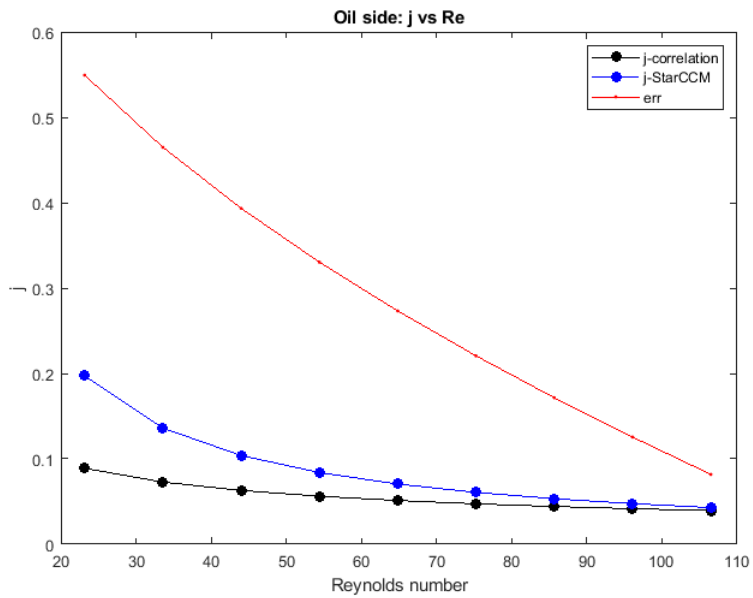


Figure 5.27: Colburn factor vs Reynold number.

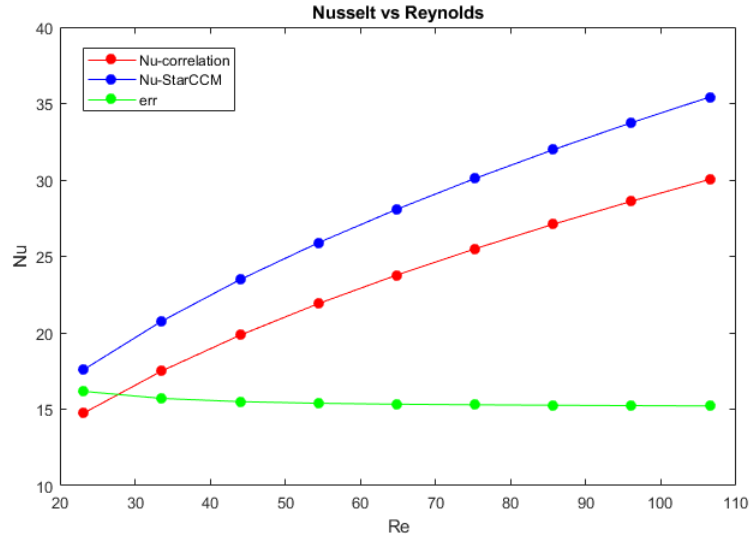


Figure 5.28: Nusselt number vs Reynold number.

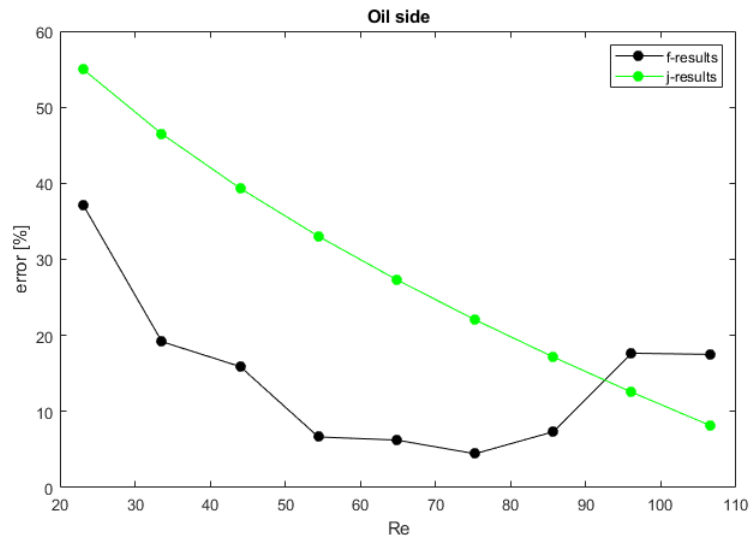


Figure 5.29: Error trend in f and j results.

5.1.7 Water side results and validation

Several simulations are played to provide data for validation of results. In particular, variation of the mass flow rate is useful. The following plots show the comparison of empirical trend by correlation and StarCCM+ results referred to different working conditions, as variation of rpm of the engine to which corresponds changing in temperature and pressure. Error is quite larger because of a series of mismatch introduced during test data record. It is also important to consider the fact that RANS model involved for simulation generates more variation respect to mean value. For this reason the validation is correct about trend, not exactly reliable about numbers.

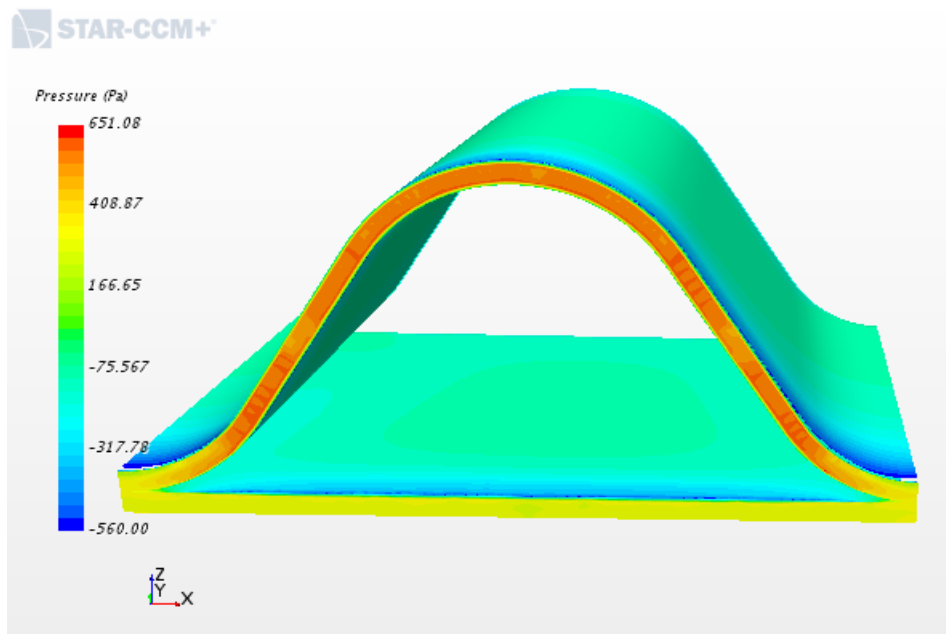


Figure 5.30: Water pressure.

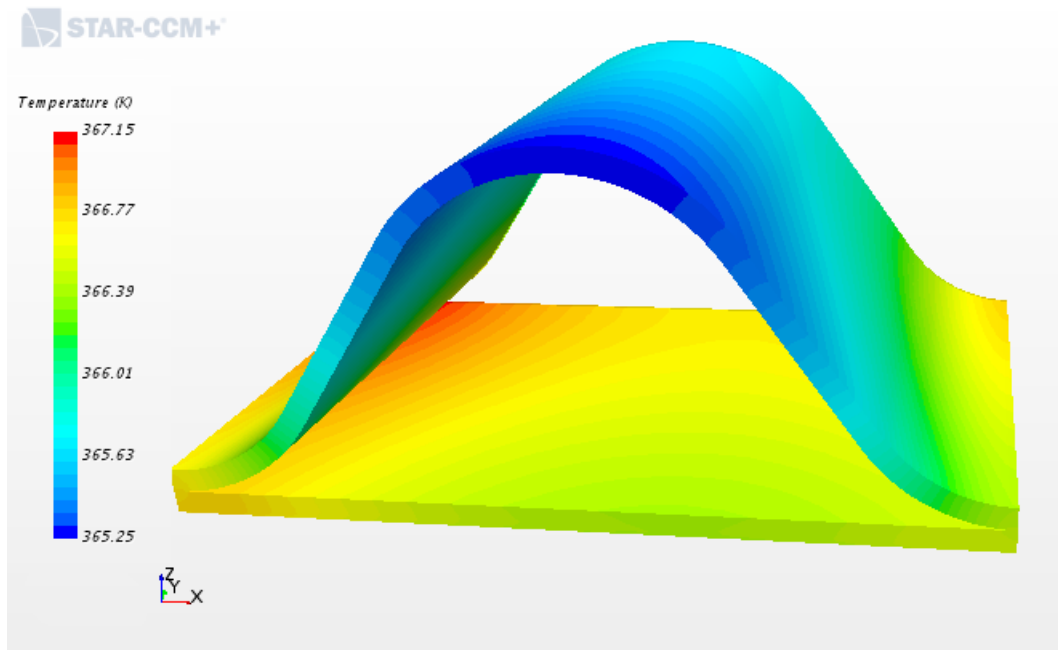


Figure 5.31: Water temperature.

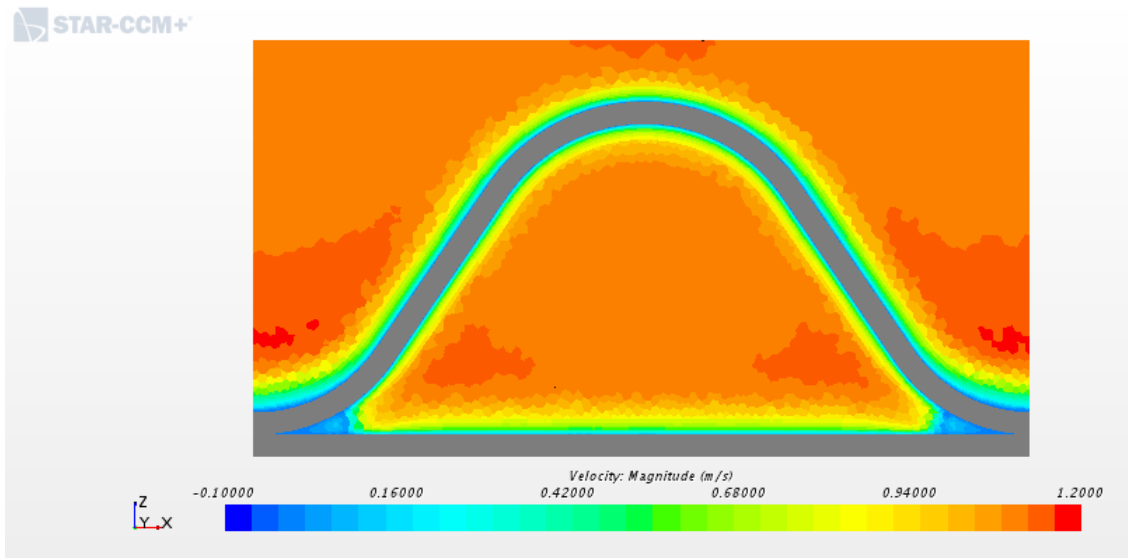


Figure 5.32: water velocity.

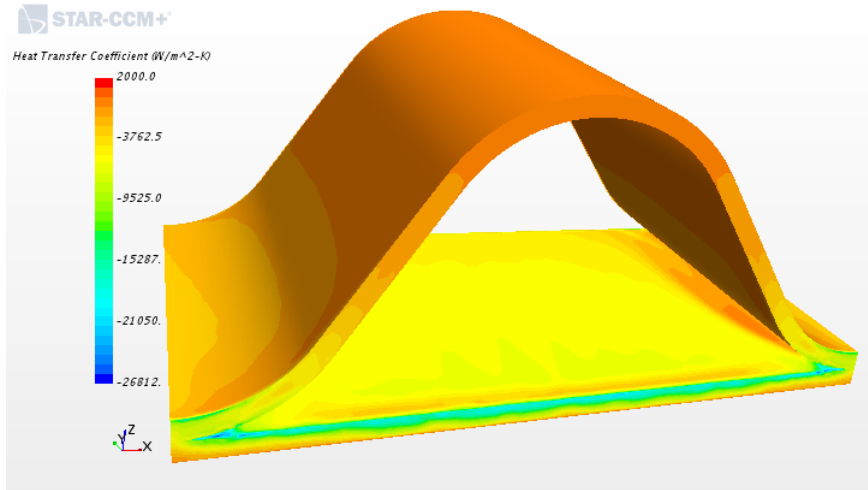


Figure 5.33: Heat transfer coefficient, water side.

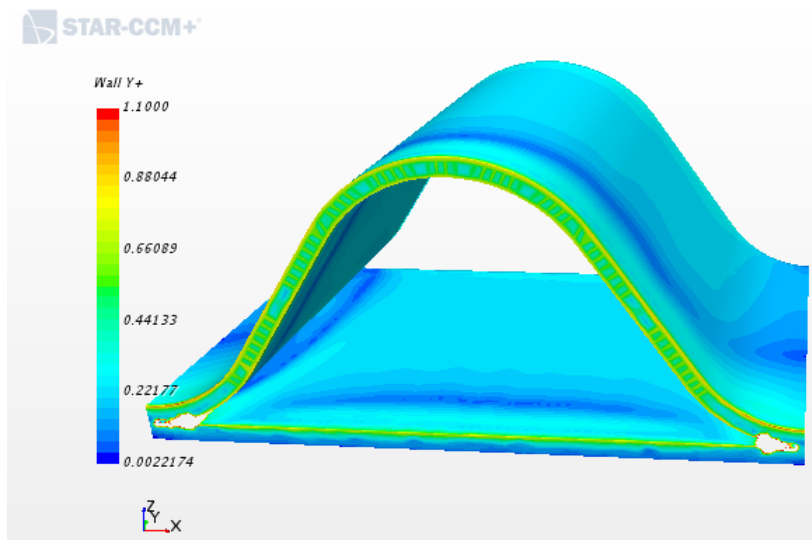


Figure 5.34: Wall y^+ water side.

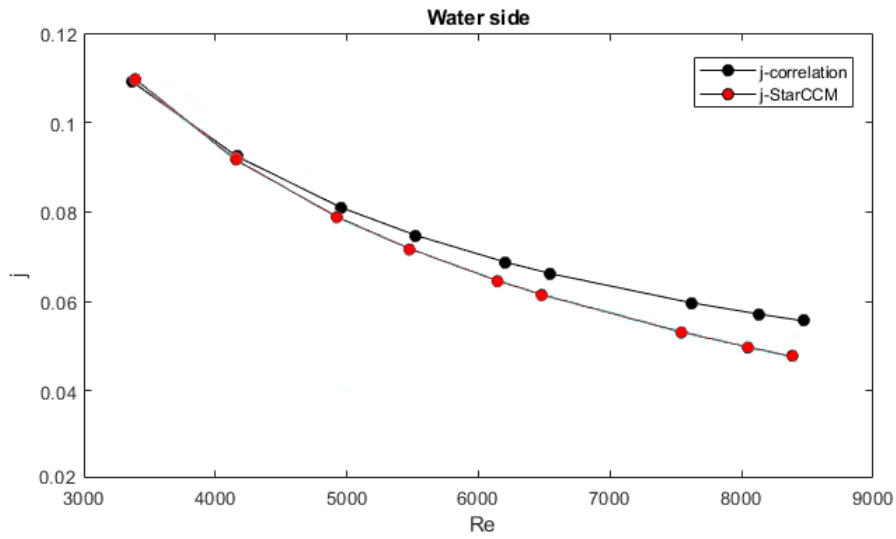


Figure 5.35: Colburn factor j vs Reynolds Number, water side.

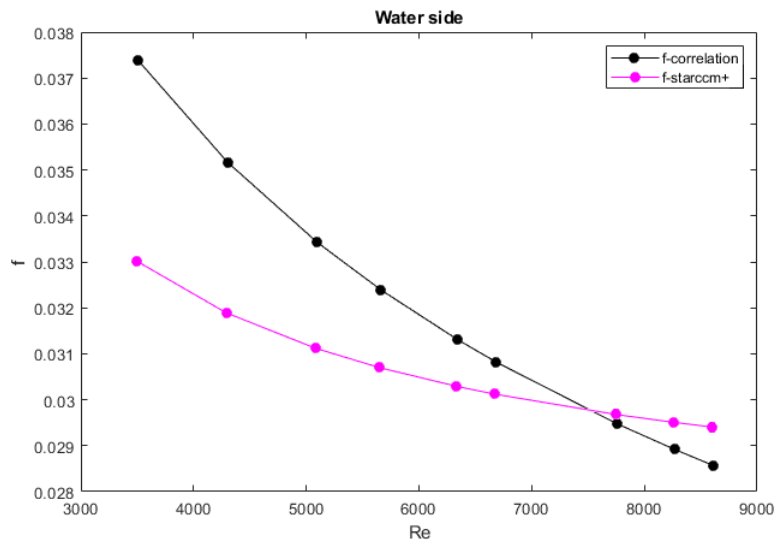


Figure 5.36: Fanning friction coefficient f vs Reynolds number, water side.

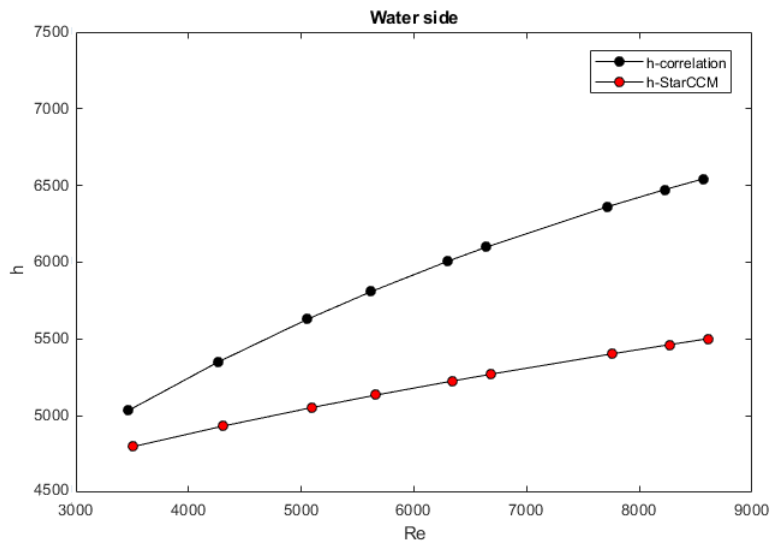


Figure 5.37: Heat transfer coefficient for water.

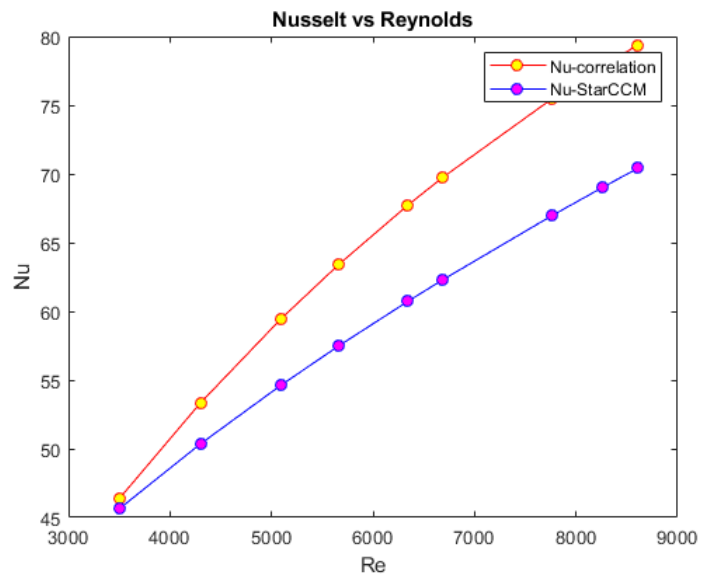


Figure 5.38: Nusselt number vs Reynolds number, water side.

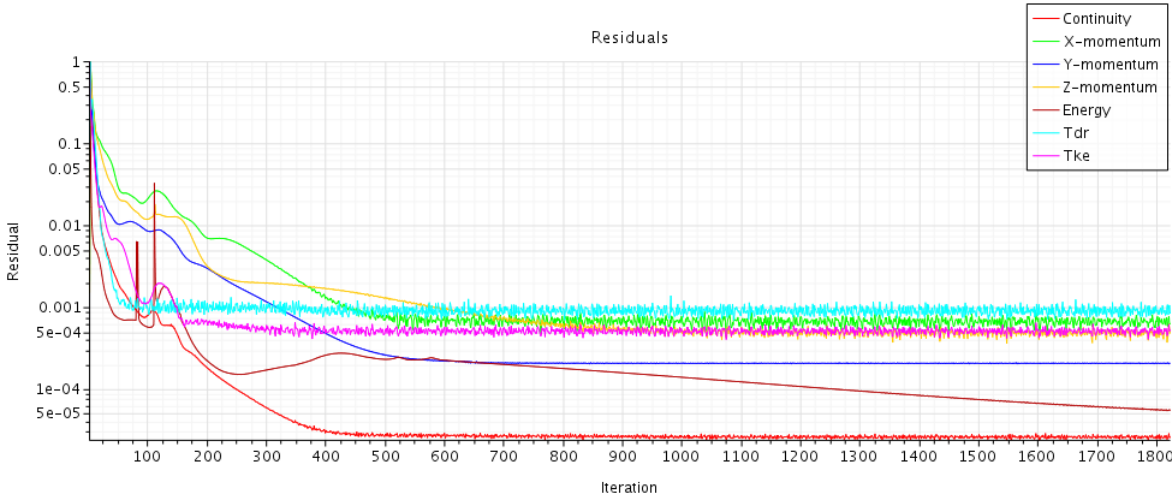


Figure 5.39: Residuals after simulation, water side.

Chapter 6

Conclusions

In the last chapter a brief but useful simulation has been performed to simulate and validate the actual heat exchanger performance. Starting by a 1D prediction of the heat transfer coefficient thanks to several empirical correlations, analytical exam is conducted. In particular, by choosing a split between water side and oil side, as cold working fluid and hot working fluid, respectively. Clearly, this setting resulted the best solution in view of a CFD analysis. However, some considerations are required to explain different solutions and discrepancy related to water side in particular. Let start by this last one aspect, by considering the StarCCM+ analysis:

- The Reynolds number of the water fluid is turbulent, about 6000 and the model to solve the simulations is based on the RANS equations and, specifically, involves the Realizable k-epsilon model provided by the software;
- The heat transfer coefficient read into the color map as output of the simulation is not ready to be utilized for validation. A little post-processing needed like a surface averaged value for the parameter considered.
- In the table provided by the company, is clear that a quite high discrepancy is introduced by not so reliable simplification in the test facility like the point of reading of test parameters. In particular, location of pressure is referred not on the heat exchanger's inlet and outlet, but at the outlet of cylinders and inlet of the hydraulic pump.
- All the considerations exposed below, are not valid for oil side. In spite of the fact that in simulation a certain errors are naturally involved, the fluid domain

is characterized by laminar evolution and the model results as accurate as reliable.

Table 6.1: Water side discrepancy about results, at $Re=6186$.

Parameter	Correlation	StarCCM+	Deviation
h	5186 W/m ² k	5862 W/m ² k	12.93%
j	0.0087	0.0072	17.24%
f	0.0464	0.0313	32%

As table show, an error of about 33% affects the result of the fanning friction coefficient. The pressure drop are not reliable because of the positioning of sensors. In particular:

- It is not quite accurate records pressur at engine’s head since several elements are placed between the exchanger inlet and the probe. These elements augments pressure losses, and are: radiator, valves, thermostat, lenght of channels, pump and filter.
- It is not quite accurate the pressure at the outlet of heat exchanger since the value reported in table is referred to pump’s impeller.

Nevertheless, the validation of CFD model is more accurate if oil side is taken into account. In fact, error’s trend is quite small and the results accurate. To sum up, a new test facility is recommended, it will be useful to disassemble the heat exchanger from engine and test it in a dedicated structure.

In the present dissertartion a novel core geometry is proposed to overcome the issue related to the actual heat exchanger. The cross corrugated synusoidal shape is appropriate to reduce pressure drop and enhance heat transfer coefficient of about 18%. The forecast of Nu for water is 80 and HTC for water side is about 6000W/m²K.

The additive manufacturing can realize the new heat exchanger, and actually, the printing process is playing. It is useful to remember that inner cavities are quite complex to modify after machining, in fact these are closed part impregnable to post-processing like CNC finishing or post-treatment.

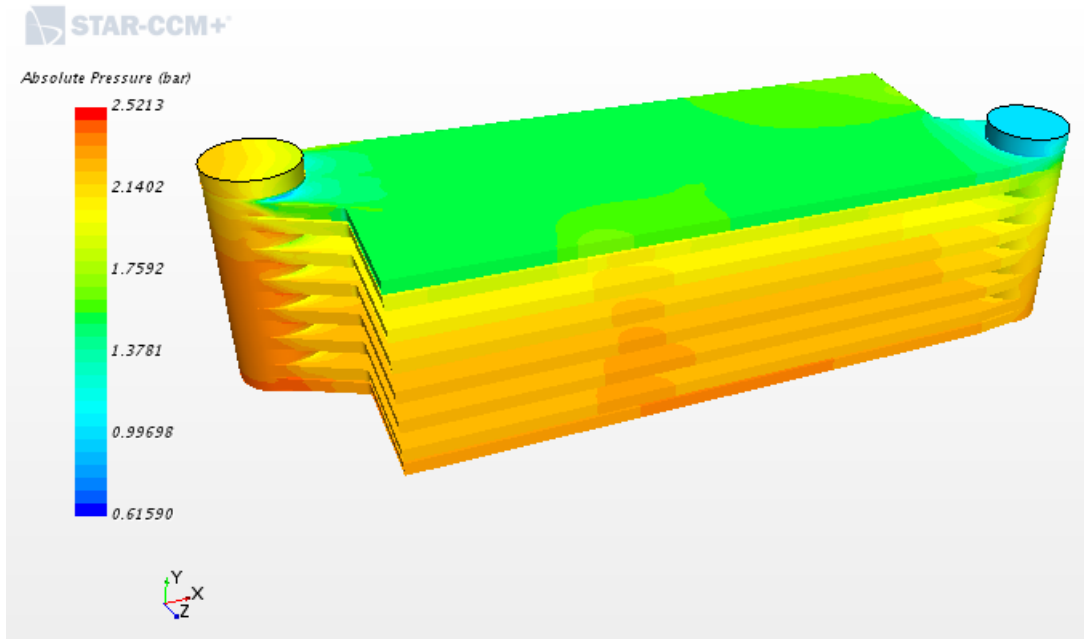


Figure 6.1: Water side absolute pressure: $\Delta P=1.03\text{bar}$.

A StarCCM+ simulation is performed taking into account the novel design and spacing. The channel is characterized by a sinusoidal development along x axis, which results in augmentation of heat transfer area. The initial conditions are the same of the previous simulation, but the inlet velocity is related to the mass flow rate through the novel passage spacing, 3.5 mm. The results show that:

- Large corrugation within plate results in zero-velocity bubbles near the wall, where kinetic energy is very small and the stagnation of fluid does not take part in enhancement of turbulent charge. These low speed zones are practically useless.
- If the pitch-height ratio rises, then a small and flatter corrugation shapes the surface. In one hand this means a reduction on the transfer area, but, on the other and this is useful for flow velocity: near the wall speed is greater than zero, no re-cycling bubbles occurred and interfere with developing of flow path and the pressure drop decreases.
- Obviously, a trade-off between all the requirements are necessary, moreover a special attention is paid to manufacturing process. To sum up, the second

solution is suggested by CFD analysis, directly, and avoiding specific issue is positive.

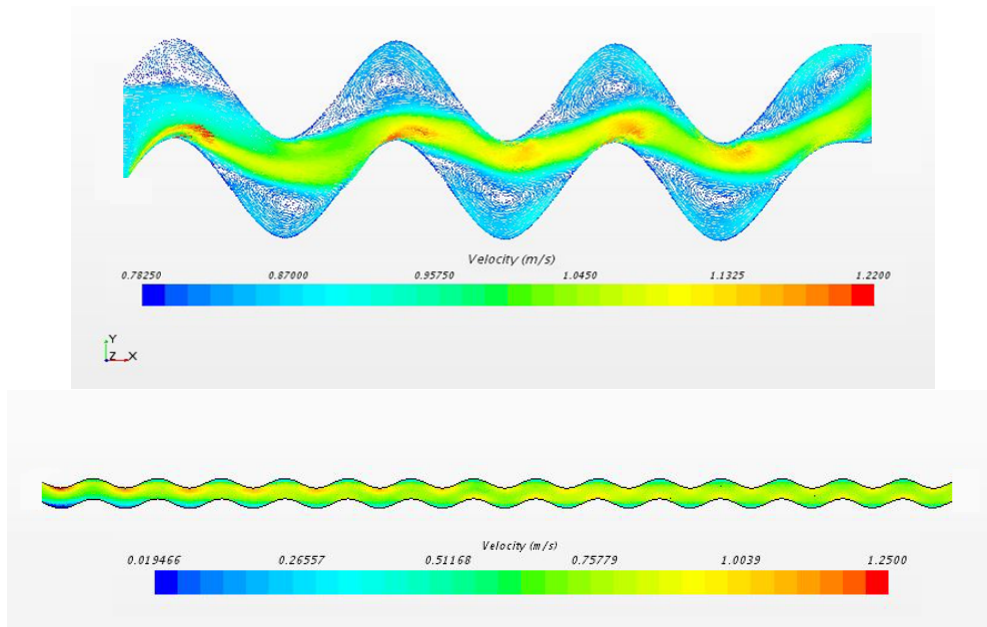


Figure 6.2: New channel layout and simulation.

Bibliography

- [1] https://en.wikipedia.org/wiki/V-twin_engine
- [2] Ferrari G., *Motori a combustione interna*, edizioni Il Capitello, Torino.
- [3] I.C.P. light aircraft brochure, M09 engine, www.icp.it
- [4] J.H. Doo, M.Y. Ha, J.K. Min, R. Stieger, A. Rolt, C. Son, *An investigation of cross-corrugated heat exchanger primary surfaces for advanced intercooled-cycle aero engines (Part-I: Novel geometry of primary surface)*, Rolls-Royce and Pusan National University Technology Centre in Thermal Management, Pusan National University, San, Jangjeon-dong, Geumjeong-gu, Busan, Republic of Korea, Strategic Research Centre, Rolls-Royce plc, P.O. Box 31, Derby DE24 8BJ, United Kingdom, 6 January 2012.
- [5] <https://en.wikipedia.org/wiki/Brazing>
- [6] Y.-Q. Wang, et al., Numerical study on plate-fin heat exchangers with plain fins and serrated fins at low Reynolds number, *Chem. Eng. Technol.* 32 (2009) 1219e1226.
- [7] Antonio Carozza, *Heat Exchangers in the Aviation Engineering*, from the book *Heat Exchangers – Advanced Features and Applications*.
- [8] Talal M. Abou Elmaatya, A.E. Kabeelb, M. Mahgoubc, *Corrugated plate heat exchanger review*.
- [9] www.Thewecgroup.com
- [10] Muley A. Heat transfer and pressure drop in plate heat exchangers [Ph.D. thesis]. Dept Mechanical Industrial and Nuclear Engineering, Div Graduate Studies and Research, University Of Cincinnati; 1997.
- [11] Martin H. A theoretical approach to predict the performance of chevron type plate heat exchangers. *Chem Eng Process* 1996.
- [12] Lee SH, Bai YI, Cho DJ. The effect of aspect ratio on turbulent flow heat

- transfer and pressure drop in a plate heat exchanger. *Int J Heat Exch* 2000.
- [13] Zhi-jian L, Guan-min Z, Mao-cheng T, Ming-xiu F. *Flow resistance and heat transfer characteristics of a new type plate heat exchanger*, *J Hydrodyn* 2008.
- [14] ZHAO Zhen-nan. *Effects of the corrugated inclination angle on heat transfer and resistance performance of plate heat exchangers*. Petro-Chemical Equipment, 2001.
- [15] Doo JH, Ha MY, Min, JK, Stieger R, Rolt A, Son C. *Theoretical prediction of longitudinal heat conduction effect in cross-corrugated heat exchanger*, *Int J Heat Mass Transf* 2012.
- [16] J.H. Doo, M.Y. Ha, J.K. Min, R. Stieger, A. Rolt, C. Son, *An investigation of cross-corrugated heat exchanger primary surfaces for advanced intercooled-cycle aero engines*.
- [17] Oraib Al-Ketana, Reza Rowshanc, Rashid K. Abu Al-Rub, *Topology-mechanical property relationship of 3D printed strut, skeletal, and sheet based periodic metallic cellular materials*.
- [18] Z. Chen, Q. Li, D. Meier, H.-J. Warnecke, *Convective heat transfer and pressure loss in rectangular ducts with drop-shaped pin fins*, Chemical Engineering, University of Paderborn, D-33098 Paderborn, Germany.
- [19] Zukauskas, A. A.: (1972) *Heat Transfer From Tubes in Cross flow. Advances in Heat Transfer*.
- [20] HiETA technologies, *Additive manufacturing of compact heat Exchangers*, 34th HEXAG meeting, 20 June 2017, The buttery and L101, Mertz Court, Newcastle University.
- [21] Yunus A. Cengel, *Termodinamica e trasmissione del calore*, 4th edition, McGraw Hill.
- [22] Adrian Bejan J. A. Jones Professor of Mechanical Engineering Department of Mechanical Engineering Duke University Durham, North Carolina, *HEAT TRANSFER HANDBOOK*.
- [23] J.H. Doo, M.Y. Ha, J.K. Min, R. Stieger, A. Rolt, C. Son, *An investigation of cross-corrugated heat exchanger primary surfaces for advanced intercooled-cycle aero engines*.
- [24] International Refrigeration and Air Conditioning Conference, *Evaluation of Fin Efficiency and Heat Transfer Coefficient for Fined Tube Heat Exchange*
- [25] D. Taler, P. Oclon, *Determination of heat transfer formulas for gas flow in*

- fin,Äi and-tube heat exchanger with oval tubes using CFD simulations*, Chem. Eng. Process.
- [26] S.W. Qian, *Heat Exchanger Design Handbook*, Chemical Industry Press, Beijing, 2002.
- [27] *C : /Program%20Files/CD – adapco/13.02.011 – R8/STAR – CCM + 13.02.011 – R8/doc/en/online/index.htmlpage/STARCCMP%2FGUID – 26938C38 – 3527 – 420B – 80FD – 48DB39AF6640%3Den3D.html%23*
- [28] *foundationTutorials/data,selectcheckMeshQuality.java*